

# SENSORS & TRANSDUCERS

ISSN 1726-5479

vol. 211

4/17



Physical, Chemical Sensors and Biosensors

# Sensors & Transducers

**International Official Open Access Journal of the  
International Frequency Sensor Association (IFSA)  
Devoted to Research and Development  
of Sensors and Transducers**

Volume 211, Issue 4, April 2017

---

**Editor-in-Chief**

Prof., Dr. Sergey Y. YURISH



IFSA Publishing: Barcelona • Toronto

*Sensors & Transducers* is an open access journal which means that all content (article by article) is freely available without charge to the user or his/her institution. Users are allowed to read, download, copy, distribute, print, search, or link to the full texts of the articles, or use them for any other lawful purpose, without asking prior permission from the publisher or the author. This is in accordance with the BOAI definition of open access. Authors who publish articles in *Sensors & Transducers* journal retain the copyrights of their articles. The *Sensors & Transducers* journal operates under the Creative Commons License CC-BY.

Notice: No responsibility is assumed by the Publisher for any injury and/or damage to persons or property as a matter of products liability, negligence or otherwise, or from any use or operation of any methods, products, instructions or ideas contained in the material herein.

Published by International Frequency Sensor Association (IFSA) Publishing. Printed in the USA.





**Editors-in-Chief:** Professor, Dr. Sergey Y. Yurish, tel.: +34 696067716, e-mail: editor@sensorsportal.com

**Editors for Western Europe**

Meijer, Gerard C.M., Delft Univ. of Technology, The Netherlands  
Ferrari, Vittorio, Università di Brescia, Italy  
Mescheder, Ulrich, Univ. of Applied Sciences, Furtwangen, Germany

**Editor for Eastern Europe**

Sachenko, Anatoly, Ternopil National Economic University, Ukraine

**Editors for North America**

Katz, Evgeny, Clarkson University, USA  
Datskos, Panos G., Oak Ridge National Laboratory, USA  
Fabien, J. Josse, Marquette University, USA

**Editor for Africa**

Maki K., Habib, American University in Cairo, Egypt

**Editors South America**

Costa-Felix, Rodrigo, Inmetro, Brazil  
Walsoe de Reça, Noemi Elisabeth, CINSO-CITEDEF  
UNIDEF (MINDEF-CONICET), Argentina

**Editors for Asia**

Ohyama, Shinji, Tokyo Institute of Technology, Japan  
Zhengbing, Hu, Huazhong Univ. of Science and Technol., China  
Li, Gongfa, Wuhan Univ. of Science and Technology, China

**Editor for Asia-Pacific**

Mukhopadhyay, Subhas, Massey University, New Zealand

**Editorial Board**

Abdul Rahim, Ruzairi, Universiti Teknologi, Malaysia  
Abramchuk, George, Measur. Tech. & Advanced Applications, Canada  
Aluri, Geetha S., Globalfoundries, USA  
Ascoli, Giorgio, George Mason University, USA  
Atalay, Selcuk, Inonu University, Turkey  
Atghiaee, Ahmad, University of Tehran, Iran  
Augutis, Vygantas, Kaunas University of Technology, Lithuania  
Ayeshe, Aladdin, De Montfort University, UK  
Baliga, Shankar, B., General Monitors, USA  
Barlingay, Ravindra, Larsen & Toubro - Technology Services, India  
Basu, Sukumar, Jadavpur University, India  
Booranawong, Apidet, Prince of Songkla University, Thailand  
Bousbia-Salah, Mounir, University of Annaba, Algeria  
Bouvet, Marcel, University of Burgundy, France  
Campanella, Luigi, University La Sapienza, Italy  
Carvalho, Vitor, Minho University, Portugal  
Changhai, Ru, Harbin Engineering University, China  
Chen, Wei, Hefei University of Technology, China  
Cheng-Ta, Chiang, National Chia-Yi University, Taiwan  
Cherstvy, Andrey, University of Potsdam, Germany  
Chung, Wen-Yaw, Chung Yuan Christian University, Taiwan  
Cortes, Camilo A., Universidad Nacional de Colombia, Colombia  
D'Amico, Arnaldo, Università di Tor Vergata, Italy  
De Stefano, Luca, Institute for Microelectronics and Microsystem, Italy  
Ding, Jianning, Changzhou University, China  
Djordjević, Alexander, City University of Hong Kong, Hong Kong  
Donato, Nicola, University of Messina, Italy  
Dong, Feng, Tianjin University, China  
Erkmen, Aydan M., Middle East Technical University, Turkey  
Fezari, Mohamed, Badji Mokhtar Annaba University, Algeria  
Gaura, Elena, Coventry University, UK  
Gole, James, Georgia Institute of Technology, USA  
Gong, Hao, National University of Singapore, Singapore  
Gonzalez de la Rosa, Juan Jose, University of Cadiz, Spain  
Goswami, Amarjyoti, Kaziranga University, India  
Guillet, Bruno, University of Caen, France  
Hadjiloucas, Sillas, The University of Reading, UK  
Hao, Shiyong, Michigan State University, USA  
Hui, David, University of New Orleans, USA  
Jaffrezic-Renault, Nicole, Claude Bernard University Lyon 1, France  
Jamil, Mohammad, Qatar University, Qatar  
Kaniusas, Eugenijus, Vienna University of Technology, Austria  
Kim, Min Young, Kyungpook National University, Korea  
Kumar, Arun, University of Delaware, USA  
Lay-Ekuakille, Aime, University of Lecce, Italy  
Li, Fengyuan, HARMAN International, USA  
Li, Jingsong, Anhui University, China  
Li, Si, GE Global Research Center, USA  
Lin, Paul, Cleveland State University, USA  
Liu, Aihua, Chinese Academy of Sciences, China  
Liu, Chenglian, Long Yan University, China  
Liu, Fei, City College of New York, USA  
Mahadi, Muhammad, University Tun Hussein Onn Malaysia, Malaysia

Mansor, Muhammad Naufal, University Malaysia Perlis, Malaysia  
Marquez, Alfredo, Centro de Investigacion en Materiales Avanzados, Mexico  
Mishra, Vivekanand, National Institute of Technology, India  
Moghavvemi, Mahmoud, University of Malaya, Malaysia  
Morello, Rosario, University "Mediterranea" of Reggio Calabria, Italy  
Mulla, Intiaz Sirajuddin, National Chemical Laboratory, Pune, India  
Nabok, Aleksey, Sheffield Hallam University, UK  
Neshkova, Milka, Bulgarian Academy of Sciences, Bulgaria  
Passaro, Vittorio M. N., Politecnico di Bari, Italy  
Patil, Devidas Ramrao, R. L. College, Parola, India  
Penza, Michele, ENEA, Italy  
Pereira, Jose Miguel, Instituto Politecnico de Seteabal, Portugal  
Pillarsetti, Anand, Sensata Technologies Inc, USA  
Pogacnik, Lea, University of Ljubljana, Slovenia  
Pullini, Daniele, Centro Ricerche FIAT, Italy  
Qiu, Liang, Avago Technologies, USA  
Reig, Candid, University of Valencia, Spain  
Restivo, Maria Teresa, University of Porto, Portugal  
Rodríguez Martínez, Angel, Universidad Politécnica de Cataluña, Spain  
Sadana, Ajit, University of Mississippi, USA  
Sadeghian Marnani, Hamed, TU Delft, The Netherlands  
Sapozhnikova, Ksenia, D. I. Mendeleev Institute for Metrology, Russia  
Singhal, Subodh Kumar, National Physical Laboratory, India  
Shah, Kriyang, La Trobe University, Australia  
Shi, Wendian, California Institute of Technology, USA  
Shmaliy, Yuriy, Guanajuato University, Mexico  
Song, Xu, An Yang Normal University, China  
Srivastava, Arvind K., Systron Donner Inertial, USA  
Stefanescu, Dan Mihai, Romanian Measurement Society, Romania  
Sumridetchkajorn, Sarun, Nat. Electr. & Comp. Tech. Center, Thailand  
Sun, Zhiqiang, Central South University, China  
Sysoev, Victor, Saratov State Technical University, Russia  
Thirunavukkarasu, I., Manipal University Karnataka, India  
Thomas, Sadiq, Heriot Watt University, Edinburgh, UK  
Tian, Lei, Xidian University, China  
Tianxing, Chu, Research Center for Surveying & Mapping, Beijing, China  
Vanga, Kumar L., ePack, Inc., USA  
Vazquez, Carmen, Universidad Carlos III Madrid, Spain  
Wang, Jiangping, Xian Shiyong University, China  
Wang, Peng, Qualcomm Technologies, USA  
Wang, Zongbo, University of Kansas, USA  
Xu, Han, Measurement Specialties, Inc., USA  
Xu, Weihe, Brookhaven National Lab, USA  
Xue, Ning, Agiltron, Inc., USA  
Yang, Dongfang, National Research Council, Canada  
Yang, Shuang-Hua, Loughborough University, UK  
Yaping Dan, Harvard University, USA  
Yue, Xiao-Guang, Shanxi University of Chinese Traditional Medicine, China  
Xiao-Guang, Yue, Wuhan University of Technology, China  
Zakaria, Zulkarnay, University Malaysia Perlis, Malaysia  
Zhang, Weiping, Shanghai Jiao Tong University, China  
Zhang, Wenming, Shanghai Jiao Tong University, China  
Zhang, Yudong, Nanjing Normal University China

# Contents

Volume 211  
Issue 4  
April 2017

[www.sensorsportal.com](http://www.sensorsportal.com)

ISSN 2306-8515  
e-ISSN 1726-5479

## Research Articles

- Modified Laccase-Gold Nanoparticles-Tetrathiafulvalene-SPCEs Based Biosensor to Determine W(VI) in Water**  
*Ana Lorena Alvarado-Gámez, M. Julia Arcos-Martínez*..... 1
- Optimum Combination and Effect Analysis of Piezoresistor Dimensions in Micro Piezoresistive Pressure Sensor Using Design of Experiments and ANOVA: a Taguchi Approach**  
*Kirankumar B. Balavalad and B. G. Sheeparamatti*..... 8
- Effect of Annealing and Operating Substrate Temperature on Methanol Gas Sensing Properties of SnO<sub>2</sub> Thin Films**  
*Priyanka Kakoty, Manabendra Bhuyan and Karen Das*..... 16
- Nanocrystalline CdSnO<sub>3</sub> Based Room Temperature Methanol Sensor**  
*Shanabhau Bagul, Dhanashri Patil, Priyanka Patil and Lalchand Patil*..... 23
- Synthesis of Nanocrystalline CdSnO<sub>3</sub> Powder on Large Scale by Simple Wet-chemical Route and CdSnO<sub>3</sub> Thick Film Based Sensors for NO<sub>2</sub> Sensing**  
*Shanabhau Bagul, Dhanashri Patil, Priyanka Patil and Lalchand Patil*..... 32
- Phase Method of Invariant Measurement of Active-Inductive Measuring Two-Pole Parameters**  
*Boris Mamikonyan*..... 38
- Chebyshev and Modified Wavelet Algorithm Based Sleep Arousals Detection Using EEG Sensor Database**  
*Mahalaxmi U. S. B. K. and Ramesh Patnaik M.* ..... 43
- Optimal Threshold Estimation Using Cultural Algorithm for EMD-DWT based ECG Denoising**  
*Rama Raju N. S. V. N. and V. Malleswara Rao*..... 51

Authors are encouraged to submit article in MS Word (doc) and Acrobat (pdf) formats  
by e-mail: [editor@sensorsportal.com](mailto:editor@sensorsportal.com). Please visit journal's webpage with preparation instructions:  
<http://www.sensorsportal.com/HTML/DIGEST/Submission.htm>

## Modified Laccase-Gold Nanoparticles-Tetrathiafulvalene-SPCEs Based Biosensor to Determine W(VI) in Water

<sup>1</sup> Ana Lorena Alvarado-Gómez, <sup>2</sup> M. Julia Arcos-Martínez

<sup>1</sup> School of Chemistry and Centro de Electroquímica y Energía Química, CELEQ, University of Costa Rica, San Pedro de Montes de Oca, 11501-2060, San José, Costa Rica

<sup>2</sup> Department of Chemistry, Faculty of Sciences, University of Burgos, Plaza Misael Bañuelos s/n, 09001 Burgos, Spain

<sup>1</sup> Tel.: 506-25112442, fax: 506-25112446

E-mail: ana.alvaradogomez@ucr.ac.cr

Received: 17 February 2017 / Accepted: 31 March 2017 / Published: 30 April 2017

**Abstract:** It was developed an amperometric biosensor to determine tungsten in water, based on the inhibition of laccase enzyme, by tungsten ions using pyrocatechol as a substrate. The enzyme was immobilized with a proper mixture containing, bovine serum albumin, and glutaraldehyde, for a cross-linking process over screen-printed carbon electrodes, previously modified with tetrathiafulvalen and gold nanoparticles. Optimized experimental conditions are: pyrocatechol in cell 0.040 mM in a phosphate buffer pH 6.5 and applied potential +350 mV. The repeatability and reproducibility, in terms of relative standard deviation values, of the developed biosensor were 3.3 % (n=3), and 2.2 % (n = 5) respectively, and detection limit was  $1.8 \times 10^{-7}$  mol L<sup>-1</sup>. Additionally it was determined the kinetics of the systems by means of Michaelis-Menten *K<sub>m</sub>* apparent constants, calculated using Lineweaver-Burk plots, with and without tungsten. Kinetic study resembles to be competitive inhibition. A recovery study was performed with spiked blanks with a tungsten certified reference standard, traceable to NIST, giving as a result  $102.3 \pm 6.7$  %; tap water samples analyzed presented a mean concentration of 1.75 μM, and recovery of the tungsten certified reference standard on the tap water samples gave  $98.8 \pm 3.1$  %.

**Keywords:** Biosensor, Cathecol, Gold nanoparticles, Laccase, Screen printed carbon electrodes, Tetrathiafulvalen, Tungsten, Water.

### 1. Introduction

Tungsten is a transition metal, found along with chromium, molybdenum and seaborgium, element 106 of the periodic table [1]. It is a valuable metal because of its great strength at high temperatures and its high electric and heat conductivity. Tungsten and its alloys have been used for many years in a wide range of applications from daily household necessities to highly specialized components of modern science and technology, such as heating elements for furnaces, filaments for electric lamps, spacecraft shielding, drill

tips, edging of cutting tools, medical equipment and small bore ammunition [1].

Tungsten in its metal form is not present in nature; rather, the tungstate anion persists and is thermodynamically stable under most environmental conditions. Polymerization of tungstate with itself and other common oxyanions (e.g. molybdate, phosphate, and silicate) can create a variety of polymer species [2-3].

Tungsten's release into environmental systems may occur as a result of natural or anthropogenic activities [4]. Natural deposits of tungsten ore can

release soluble and mobile tungstate into groundwater. Additionally, there is increasing interest in some anthropogenic sources of tungsten, which could become sources in the environment, including industrial, civilian, recreational and military applications [1-2, 4-6].

Although there have been several studies of the behavior and effects of tungsten in laboratory animals, little attention has been given to the problem of developing a biologically realistic model of the kinetics of tungsten in the human body [7]. Some tungsten compounds, which exert adverse biological effects on humans and animals, had been reported, nevertheless effects of tungsten on environmental systems have not been investigated extensively and published data are fragmentary [4, 8].

In Fallon, Nevada, childhood leukemia cluster affected this zone, supposed an investigation by the United States Centers for Disease Control and Prevention (CDC) that revealed through urine analysis, that residents were exposed to elevated levels of tungsten (VI) [9]. While it is inherently difficult to directly link these childhood leukemia clusters to environmental exposure to elevated tungsten concentrations, either via inhalation or through consumption of tungsten contaminated drinking waters, many studies have shown that this metal can be toxic and may indeed be carcinogenic [7, 10]. This investigation led to a study by the U.S. Geological Survey of tungsten in ground waters of the Carson Desert region of northwest Nevada, which showed concentrations of this metal ranging from 0.27–742  $\mu\text{g kg}^{-1}$  [5, 9-10].

Several methods to determine tungsten in water and other environmental samples have been published; among them are spectrophotometry [11], flame atomic absorption spectrometry (FAAS) [12], inductively coupled plasma atomic emission spectrometry (ICP-AES) [13], inductively coupled plasma mass spectrometry (ICP-MS) [14], X-ray fluorescence (XRF) [15], spectrofluorometry [16], polarography [17], voltammetry [8] and amperometry [18]. The sensitivity for tungsten by some of these techniques was lower than the necessary to analyze the low tungsten concentration present in water.

Among electroanalytical techniques, the chronoamperometry is getting more significance in the development of amperometric biosensors based on enzyme immobilization onto electrode surfaces that can retain their bioactivity and is one of the main issues in several fields ranging from environmental analysis to clinical diagnosis [19]. In the specific case of laccase-based biosensors, an extensive research effort has been addressed to incorporate laccase on electrode surfaces by different immobilization strategies in order to design biosensors with a wide range of applications. Many references show that its retained bioactivity mostly depends on the chosen immobilization method [20-24].

Chemically modified electrodes (CMEs) represent a modern approach to electroodic systems. Thus a proper alteration of electrode surfaces can achieve

characteristics to solve many electroanalytical problems, and may be the basis for a new device with better electrochemical distinctiveness.

The use of tetrathiafulvalen (TTF) as a mediator and the fact to be screen-printed is based in its non-solubility in water, so it may avoid risks of dissolution when working in aqueous solutions. Besides, TTF oxides losing one electron at +0.34 V, and a second electron at +0.78 V vs. Ag/AgCl in acetonitrile solution [24]. Thus, TTF based SPCEs have been built by screen-printed of a mixture of mediator and carbon ink. Then gold nanoparticles have been deposited and laccase enzyme have been cross-linked to TTF modified SPCEs (SPC<sub>TTF</sub>Es) with glutaraldehyde (GA) and bovine serum albumin (BSA) to obtain a biosensor for tungsten detection [25-27].

The purpose of this work was to obtain a sensitive biosensor for the quantitative determination of W(VI), based in the inhibitor effect of this metal over the enzymatic oxidation of catechol by laccase enzyme. So far it has not published anything like in the literature. To achieve this, laccase SPC<sub>TTF</sub>Es based biosensors are presented and the effects of gold nanoparticles (AuNPs), are also described.

## **2. Materials and Methods**

### **2.1. Reagents**

Laboratory-made screen-printed electrodes were made-up using different commercial inks: carbon ink (C10903P14, Gwent Electronic Materials, Torfaen, UK), dielectric ink (D2071120D1, Gwent Electronic Materials, Torfaen, UK), Ag/AgCl ink (SS Electrode 6037, Acheson Colloiden, Scheemda, Netherlands) and Ag ink (Electrode 418, Acheson Colloiden, Scheemda, Netherlands).

Tetrathiafulvalen (TTF) was acquired from Acros Organics (Geel, Belgium). Glutaraldehyde (GA), bovine serum albumin (BSA), Rhus vernicifera laccase enzyme (LAC), and pyrocatechol from Fluka Analytical, (St. Louis, MO, USA).

Phosphate salts for buffer preparation, Na<sub>2</sub>HPO<sub>4</sub> and KH<sub>2</sub>PO<sub>4</sub> used as supporting electrolyte were from Merck, (Darmstadt, Germany), NaOH and H<sub>3</sub>PO<sub>4</sub> to adjust pH from J.T. Baker, (Deventer, Netherlands).

Tungsten standard solutions 2 mg L<sup>-1</sup> were prepared daily from a 100 mg L<sup>-1</sup> ammonium tungstate CertiPUR traceable to NIST (Merck, Darmstadt, Germany) SRM stock solution, and store at 4 °C when not in use. Tungsten metal purity 99.99 % in 2 % v/v HNO<sub>3</sub>, certified value 1000 ± 4 mgL<sup>-1</sup> (High-Purity Standards, CRM traceable to NIST, SRM against 3163, lot 080331, USA) was used to spiked blanks samples and tap water samples for recovery studies.

All chemical reagents used were analytical grade, without any further purification. All solutions were prepared with ultrapure water from a TKA

System, 0.05  $\mu\text{S}/\text{cm}$  (18  $\text{M}\Omega$  (Gen-Pure TKA, Niederelbert, Germany).

## 2.2. Apparatus and Software

A DEK 248 screen-printing machine (DEK, Weymouth, UK) was used for the preparation of the screen printed transducers.

Cyclic voltammetric and chronoamperometric measurements were performed with an electrochemical potentiostat Autolab 128N with GPES software (Eco Chemie, Utrecht, The Netherlands). Buffer pH was adjusted with a Mettler-Toledo pHmeter S47-K (Columbus, Ohio, USA).

## 3. Methodology

### 3.1. Laboratory-made $\text{SPC}_{\text{TTF}}$ Es Preparation

Depending of the nature and characteristics of the electrodes, they can be easily built by using diverse kinds of inks. In this way, the screen-printed electrodic system based on three-electrode configuration (working, reference and counter electrode) has been manufactured by sequential layer deposition according to previously described procedures [28-30]. Carbon ink and, well-mixed and immediately printed, carbon ink with TTF (5 %w/w) were used to prepare the working electrodes, [25-26].

### 3.2. Functionalization of $\text{SPC}_{\text{TTF}}$ Es with Gold Nanoparticles (AuNPs)

$\text{SPC}_{\text{TTF}}$ Es were modified with gold nanoparticles (AuNPs/ $\text{SPC}_{\text{TTF}}$ Es) using a 0.1 mM  $\text{HAuCl}_4$  solution in 0.5 M  $\text{H}_2\text{SO}_4$ . The deposit was made by applying a potential of + 0.18 V (vs. Ag / AgCl SPE) for 15 s under mechanical agitation [31].

### 3.3. Immobilization of Laccase Enzyme on AuNPs/ $\text{SPC}_{\text{TTF}}$ Es

Mixing proper amounts of crosslinking agent, GA, BSA with LAC enzyme was performed in order to join it to working electrode surface, already prepared with TTF mediator and functionalized with gold nanoparticles. The optimum results were achieved by dropping over different functionalized electrodes, 10  $\mu\text{L}$  of a mixture prepared by 5  $\mu\text{L}$  of LAC (0.11 % w/v), 2.5  $\mu\text{L}$  BSA (1.75 % w/v) and 2.5  $\mu\text{L}$  GA (2.5 % w/v) onto modified electrodes and let them to dry 120 min at 4  $^\circ\text{C}$ .

### 3.4. Measuring Amperometric Procedure

Amperometric measurements were carried out at room temperature, placing the modified electrode in a

cell containing 5 mL of supporting electrolyte, pH=6.5 with constant stirring, at an applied potential of + 350 mV vs. Ag/AgCl SPE. Once a stable current was obtained after the addition of substrate or corresponding samples, sequential additions of tungsten standard solutions, were added.

For different prepared biosensors, their performances were evaluated by determining precision, limits of detection and quantification, accuracy, recovery of spiked samples and possible interferences. Also a kinetic study was carried out.

## 4. Results and Discussion

As it is well know from literature, LAC is a good oxide-reductase enzyme that oxidizes ortho and para phenol groups to ortho and para quinones, and reduces oxygen to water [32-34] (Fig. 1). Laccase has not being reported for tungsten determination, but to analyze polyphenols. Nevertheless, previous experiments had shown that tungsten inhibit the activity of this enzyme to catechol as a substrate; this fact is the base of the biosensor proposed in this work.

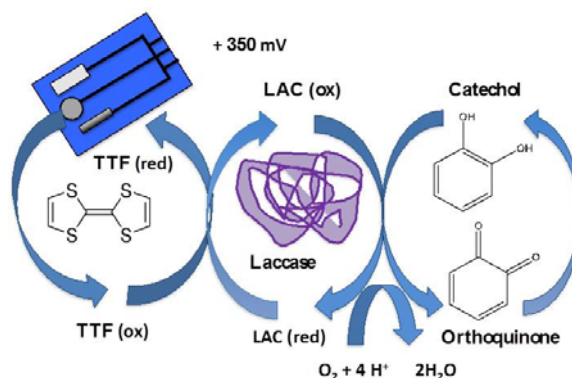


**Fig. 1.** Schematic representation of possible mechanism of catechol electrochemical reactions at laccase based biosensor-using TTF as a mediator, in the presence of oxygen according to references [32-34].

To obtain a sensitive analytical signal, a group of experiments were carried out considering the influence of three important experimental factors: applied potential ( $E_{\text{ap}}$ ), pH and catechol concentration, changing one at a time in a selected range, and keeping constant the rest. These experiments were done with LAC/AuNPs/ $\text{SPC}_{\text{TTF}}$ Es-based biosensors; so there were applied potentials between + 100 mV and + 500 mV at a fixed pH; once a potential of + 350 mV was set, then pH was changed from 5.0 to 9.0, being the best, between 6 and 7, so it was decided to work at pH 6.5. Different catechol solutions were tested ranging from 0.10 mM to 20 mM; the most stable signals were obtained with 0.040 mM catechol in cell. Fig. 2 presents a typical chronoamperogram under the selected conditions.



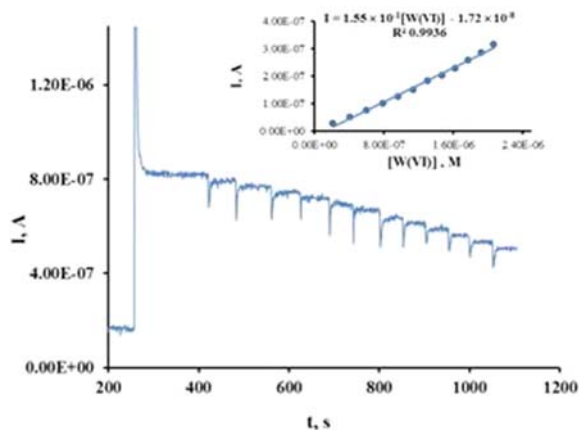


**Fig. 2.** Chronoamperogram registered using LAC/AuNPs/SPC<sub>TTFEs</sub> based-biosensor under the optimum conditions (applied potential, + 350 mV vs. Ag/AgCl SPE; Phosphate buffer pH 6.5; [catechol]: 0.04 mM). Inset: calibration curve corresponding to this chronoamperogram.

#### 4.1. Electrodes Characterization and Validation

Electrodes characterization was done by estimating precision, in terms of repeatability and reproducibility, limit of detection and quantification, accuracy and sensitivity.

The reproducibility of the modified electrodes was determined by means of relative standard deviations RSD (%), of the slopes of three independent calibration curves with three different LAC/AuNPs/SPC<sub>TTFEs</sub> and repeatability with the slopes of three independent calibration curves, using the same modified electrode; limit of detection (LOD) and limit of quantification (LOQ) were determined according to IUPAC definition [35], considering the LOD based on three times the standard deviation ( $3S_y/x$ ) of the calibration curve divided by the slope of the calibration curve. LOQ is ten times the standard deviation ( $10 S_y/x$ ) divided by the slope. Electrode performance in terms of repeatability as RSD was 3.2 %, reproducibility 2.2 %, sensitivity  $0.255 \text{ A} \cdot \text{M}^{-1}$ , LOD = 0.18  $\mu\text{M}$  and LOQ = 0.62  $\mu\text{M}$ .

Also recovery of spiked blanks with CRM W(VI) standard ( $1000 \pm 4$ )  $\text{mgL}^{-1}$  were evaluated obtaining  $102.3 \pm 6.7$  % Recovery in tap water was  $98.8 \pm 3.1$  %. Table 1 resume the results of this recoveries.

#### 4.2. Kinetics and Laccase Inhibition

To study kinetic behavior of laccase enzyme with catechol as a substrate, optimum conditions were used in the presence and absence of W(VI). To create Michaelis-Menten plots, successive aliquots of substrate were added in the cell with or without W(VI) until a constant rate was acquire, then with the linear part of it, there were obtained two reciprocal Lineweaver-Burk plots. Then their slopes and

intercepts were used to calculate Michaelis-Menten apparent constants. According to Table 2, slopes and  $K_m$  apparent increases with W(VI) concentration, which means that inhibitory effect of W(VI) on the laccase-catechol reaction was confirmed through the higher affinity of the enzyme for the substrate in the absence of this metal. Based on these results and accordingly to Fig. 3 and Table 2,  $V_{max}$  unchanged, and  $K_m \text{ app.}$  increases with inhibitor concentration, suggest competitive inhibition of the enzymatic process by the presence of the metal [36-37].

**Table 1.** Recovery of spiked blanks and tap water at pH 6.5, Eap. + 350 mV vs Ag/AgCl SPE, with W(VI) SRM standard traceable to NIST  $1000 \pm 4 \text{ mg L}^{-1}$ , with LAC/AuNPs/SPC<sub>TTFEs</sub>.

Spiked blanks			
[W(VI)] added	[W(VI)] found	% Recovery	[W(VI)] $\text{mg L}^{-1}$ Recovery
M	M		$1000 \pm 4 \text{ mg L}^{-1}$
	$4.44 \times 10^{-7}$	106.8	1067
	$4.41 \times 10^{-7}$	106.1	1060
$4.16 \times 10^{-7}$	$3.91 \times 10^{-7}$	94.0	940
	$4.52 \times 10^{-7}$	108.7	1087
	$3.99 \times 10^{-7}$	95.9	960
<b>Media</b>		102.3	1023
<b>Std. Dev.</b>		6.8	68
<b>RSD %</b>		6.6	6.6
D.F. dilution factors 50.00 mL/2.00 mL and 50.00 mL/5.00 mL			
Spiked tap water			
	$1.03 \times 10^{-6}$	99.0	1014
$1.04 \times 10^{-6}$	$9.97 \times 10^{-7}$	95.6	988
	$1.06 \times 10^{-6}$	101.6	953
<b>Media</b>		98.8	985
<b>Std. Dev.</b>		3.0	30
<b>RSD %</b>		3.1	3.1
D.F. dilution factors 5.20 mL/0.100 mL and 100.00 mL/1.00 mL			

**Table 2.**  $K_m \text{ app.}$  and Lineweaver-Burk calibration parameters for inhibition kinetics of laccase on catechol enzyme using LAC/AuNPs / SPC<sub>TTFEs</sub>.

[W(VI)] M	$K_m/V_m$ (Slope)	$K_m$ apparent, M
0	19.56	$3.1 \times 10^{-4}$
$4.95 \times 10^{-6}$ M	29.747	$5.5 \times 10^{-4}$
$3.06 \times 10^{-5}$ M	35.888	$4.2 \times 10^{-3}$

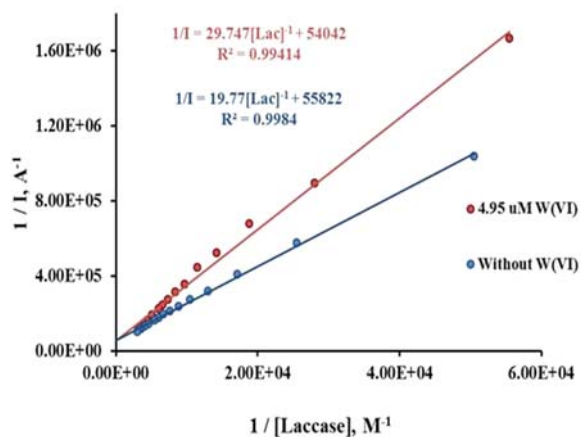


**Fig. 3.** Lineweaver-Burk graphics for laccase activity on catechol using Lac/AuNPs/SPC<sub>TTFEs</sub>, with and without W(VI) at pH 6.5 and E<sub>ap</sub> + 350 mV vs Ag/AgCl SPE.

### 4.3. Interferences Study

An analysis of possible effects caused by the presence of different metal ions was carried out by preparing standards of different cations to acquire concentrations in cell as 1.0 μM, 10 μM, 0.1 mM and 1.0 mM. Then it was calculated current from baseline to current signals obtained, determining inhibition percentage of the substrate with a number of metals added. Nevertheless, Fig. 4 represents the inhibition % of possible interferences, some of them could be usually present in natural waters, such as Al(III), Fe(III), Ca(II), As(V), Zn(II), Mo(VI), Cu(II), V(V), K(I), Na(I) and Mg(II).

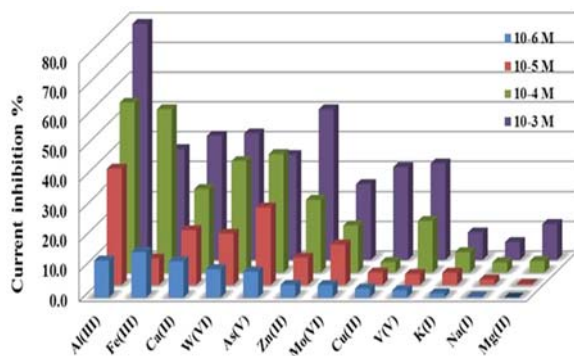


**Fig. 4.** Inhibition percentage of substrate current from several interferent cations for LAC/AuNPs/SPC<sub>TTFEs</sub> based biosensor at pH 6.5 and E<sub>ap</sub> + 350 mV vs Ag/AgCl SPE.

According to Fig. 4, Al(III), Fe(III), Ca(II) and As(V) can interfere with W(IV) measurements, at low and high concentrations and Zn(II) at 0.1 and 1 mM. Ions commonly present in water, such as Na(I), K(I) and Mg(II), cannot be considered as interferences. In agreement with several references, heavy metals in such concentrations can be removed from water samples before use the biosensors [38-39].

## 5. Conclusions

The use of laccase based biosensors using AuNPs/SPC<sub>TTFEs</sub> allows sensitive determination of W(VI). The proposed biosensor is based on the laccase enzyme inhibition by the presence of W(VI). This fact can be used to measure the decrease of a substrate current by successive additions of W(VI). According to Lineweaver-Burk plots laccase inhibition by W(VI) is competitive for these modified electrodes.

The biosensor showed excellent figures of merit such as repeatability and reproducibility, with a RSD of 3.3 % and 2.2 % respectively. LOD  $1.8 \times 10^{-7}$  M and LOQ  $6.2 \times 10^{-7}$ , accuracy in spiked blanks with a recovery of 102.3 % with a RSD of 6.6 %.

Some metals such as Al(III), Fe(III), Ca(II) and As(V) may represent significant interferences when W(VI) is present at low concentrations, if they are present in water samples, but there are many methods to remove them from water.

## Acknowledgements

The financial support made available by Vicerrectoría de Investigación and CELEQ, Universidad de Costa Rica to the project VI 804-B5-164 is gratefully acknowledged.

## References

- [1]. A. Koutsospyros W. Braida, C. Christodoulatos, D. Dermatas, N. Strigul, A review of tungsten: From environmental obscurity to scrutiny, *Journal of Hazardous Materials*, Vol. 136, Issue 1, 2006, pp. 1-19.  
<https://www.ncbi.nlm.nih.gov/pubmed/16343746>
- [2]. N. Strigul, A. Koutsospyros, C. Christodoulatos, Tungsten speciation and toxicity: Acute toxicity of mono- and poly-tungstates to fish, *Ecotoxicology and Environmental Safety*, Vol. 73, Issue 2, 2010, pp. 164-171.  
<https://www.ncbi.nlm.nih.gov/pubmed/19836837>
- [3]. J. Bednar, R. E. Boyd, W. T. Jones, C. J. McGrath, D. R. Johnson, M. Chappell, D. B. Ringelberg, Investigations of tungsten mobility in soil using column tests, *Chemosphere*, Vol. 75, Issue 8, 2009, pp. 1049-1056.  
[www.sciencedirect.com/science/journal/00456535/75/8](http://www.sciencedirect.com/science/journal/00456535/75/8)
- [4]. S. C. Hsu, H. L. Hsieh, C. P. Chen, C. M. Tseng, S. C. Huang, C. H. Huang, Y. T. Huang, V. Radashevsky, S. H. Lin, Tungsten and other heavy metal contamination in aquatic environments receiving wastewater from semiconductor manufacturing, *Journal of Hazardous Materials*, Vol. 189, Issue 1-2, 2011, pp. 193-202.  
<https://www.ncbi.nlm.nih.gov/pubmed/21377792>
- [5]. J. Feldmann, W. R. Cullen, Occurrence of volatile transition metal compounds in landfill gas: synthesis of molybdenum and tungsten carbonyls in the environment, *Environ Sci Technology*, Vol. 31, Issue 7, 1997, pp. 2125-2129.
- [6]. P. E. Leffler, G. Kazantzis, Tungsten, in Handbook on the Toxicology of Metals, Chapter 58, *Academic Press/Elsevier*, USA, 4<sup>th</sup> ed., 2007, pp. 1297-1306.

- [7]. S. Pawa, S. Ali, Liver necrosis and fulminant hepatic failure in rats: protection by oxyanionic form of tungsten, *Biochim. Biophys. Acta (BBA) - Molecular Basis of Disease*, Vol. 1688, Issue 3, 2004, pp. 210-222.  
www.sciencedirect.com/science/article/pii/S0925443903002011
- [8]. R. Piech, A. Bugajna, S. Baś, W. W. Kubiak, Ultrasensitive determination of tungsten (VI) on pikomolar level in voltammetric catalytic adsorptive catechol-chlorate (V) system, *Journal of Electroanalytical Chemistry*, Vol. 644, Issue 1, 2010, pp. 74-79.
- [9]. R. L. Seiler, K. G. Stollenwerk, J. R. Garbarino, Factors controlling tungsten concentrations in ground water, Carson Desert, Nevada, *Applied Geochemistry*, Vol. 20, Issue 2, 2005, pp. 423-441.
- [10]. K. H. Johannesson, H. B. Dave, T. J. Mohajerin, S. Datta, Controls on tungsten concentrations in groundwater flow systems: The role of adsorption, aquifer sediment Fe(III) oxide/oxyhydroxide content, and thiotungstate formation, *Chemical Geology*, Vol. 351, 2013, pp. 76-94.
- [11]. P. Lubal, H. Koprivova, O. Sedo, J. Havel, S. Lis, S. But, Simultaneous determination of molybdenum (VI) and tungsten (VI) and its application in elemental analysis of polyoxometalates, *Talanta*, Vol. 69, Issue 4, 2006, pp. 800-806.
- [12]. P. Fodor, I. Ipolyi, Atomic Absorption Spectrometry: Electrothermal, in *Encyclopedia of Analytical Chemistry*, 2<sup>nd</sup> ed., USA, Elsevier, 2004, pp. 170-180.
- [13]. N. Strigul, Does speciation matter for tungsten ecotoxicology ?, *Ecotoxicology and Environmental Safety*, Vol. 73, Issue 6, 2010, pp. 1099-1113.
- [14]. A. Bednar, J. Mirecki, L. Inouye, L. Winfield, S. Larson, D. Ringelberg, The determination of tungsten, molybdenum, and phosphorus oxyanions by high performance liquid chromatography inductively coupled plasma mass spectrometry, *Talanta*, Vol. 72, Issue 5, 2007, pp. 1828-1832.
- [15]. K. Tsuji, K. Nakano, Y. Takahashi, K. Hayashi, C. U. Ro, X-ray Spectrometry, *Analytical Chemistry*, Vol. 84, Issue 2, 2012, pp. 636-668.
- [16]. M. S. El-Shahawi, L. A. Al Khateeb, Spectrofluorometric determination and chemical speciation of trace concentrations of tungsten species in water using the ion pairing reagent procaine hydrochloride, *Talanta*, Vol. 88, 2012, pp. 587-592.
- [17]. S. K. Bhowal, M. Bhattacharyya, Determination of traces of molybdenum and tungsten by extraction and polarography of their salicylhydroxamates, *Talanta*, Vol. 36, Issue 10, 1989, pp. 989-992.
- [18]. A. L. Alvarado-Gómez, M. A. Alonso-Lomillo, O. Domínguez-Renedo, M. J. Arcos-Martínez, Chronoamperometric Screen Printed Carbon Biosensor Based on Alkaline Phosphatase Inhibition for W(IV) Determination in Water, Using 2-Phospho-L-Ascorbic Acid Trisodium Salt as a Substrate, *Sensors*, Vol. 15, Issue 2, 2015, pp. 2232-2243.
- [19]. N. Durán, M. A. Rosa, A. D'Annibale, L. Gianfreda, Applications of laccases and tyrosinases (phenoloxidases) immobilized on different supports: a review, *Enzyme and Microbial Technology*, Vol. 31, Issue 7, 2002, pp. 907-931.
- [20]. A. M. Mayer, R. C. Staples, Laccase: new functions for an old enzyme, *Phytochemistry*, Vol. 60, Issue 6, 2002, pp. 551-565.
- [21]. A. Sassolas, L. J. Blum, B. D. Leca-Bouvier, Immobilization strategies to develop enzymatic biosensors, *Biotechnology Advances*, Vol. 30, Issue 3, 2012 pp. 489-511.
- [22]. T. Kuwahara, T. Asano, M. Kondo, M. Shimomura, Bioelectrocatalytic O<sub>2</sub> reduction with a laccase-bearing poly (3-methylthiophene) film based on direct electron transfer from the polymer to laccase, *Bioelectrochemistry*, Vol. 91, 2013, pp. 28-31.
- [23]. M. Fernández-Fernández, M. A. Sanromán, D. Moldes, Recent developments and applications of immobilized laccase, *Biotechnology Advances*, Vol. 318, Issue 8, Dec. 2013, pp. 1808-1825.
- [24]. M. Bendikov, F. Wudl, D. F. Perepichka, Tetrathiafulvalenes, Oligoacenes, and Their Buckminsterfullerene Derivatives: The Brick and Mortar of Organic Electronics, *Chemical Reviews*, Vol. 104, Issue 11, 2004, pp. 4891-4945.
- [25]. L. Asturias-Arribas, M. A. Alonso-Lomillo, O. Domínguez-Renedo, M. J. Arcos-Martínez, Screen-printed biosensor based on the inhibition of the acetylcholinesterase activity for the determination of codeine, *Talanta*, Vol. 111, 2013, pp. 8-12.
- [26]. W. Henao-Escobar, O. Domínguez-Renedo, M. A. Alonso-Lomillo, M. J. Arcos-Martínez, Simultaneous determination of cadaverine and putresine using a disposal monoamine oxidase based biosensor, *Talanta*, Vol. 117, 2013, pp. 405-411.
- [27]. B. Molinero-Abad, M. A. Alonso-Lomillo, O. Domínguez-Renedo, M. J. Arcos-Martínez, Malate quinoneoxidoreductase biosensors based on tetrathiafulvalene and gold nanoparticles modified screen-printed carbon electrodes for malic acid determination in wine, *Sensors and Actuators B: Chemical*, Vol. 202, 2014, pp. 971-975.
- [28]. M. J. Giz, B. Duong, N. J. Tao, In situ STM study of self-assembled mercaptopropionic acid monolayers for electrochemical detection of dopamine, *Journal of Electroanalytical Chemistry*, Vol. 65, Issue 6, 1999, pp. 72-79.
- [29]. M. Albareda-Sirvent, A. Merkoci, S. Alegret, Configurations used in the design of screen-printed enzymatic biosensors. A review, *Sensors and Actuators B: Chemical*, Vol. 69, Issue 1-2, 2000, pp. 153-163.
- [30]. Alonso-Lomillo M. A., Yardimci C., Domínguez-Renedo O., Arcos-Martínez M. J., CYP450 2B4 covalently attached to carbon and gold screen printed electrodes by diazonium salt and thiols monolayers, *Analytica Chimica Acta*, Vol. 633, Issue 1, 2, 2009, pp. 51-56.
- [31]. O. Domínguez-Renedo, M. A. Alonso-Lomillo, L. Ferreira-Gonçalves, M. J. Arcos-Martínez, Development of urease based amperometric biosensors for the inhibitive determination of Hg (II), *Talanta*, Vol. 79, Issue 5, 2009, pp. 1306-1310.
- [32]. A. L. Yaropolov, O. V. Skorobogatko, S. S. Vartanov, S. D. Varfolomeyev, Laccase: Properties, catalytic mechanism, and applicability, *Applied Biochemistry and Biotechnology*, Vol. 49, Issue 3, 1994, pp. 257-280.
- [33]. C. Vaz-Domínguez, S. Campuzano, O. Rüdiger, M. Pita, M. Gorbacheva, S. Shleev, V. M. Fernández, A. L. De Lacey, Laccase electrode for direct electrocatalytic reduction of O<sub>2</sub> to H<sub>2</sub>O with high-operational stability and resistance to chloride inhibition, *Biosensors and Bioelectronics*, Vol. 24, Issue 4, 2008, pp. 531-537.

- [34]. V. Madhavi, S. S. Lele, Laccase: Properties and applications, *Bioresources*, Vol. 4, Issue 4, 2009, pp. 1694-1717, <http://ncsu.edu/bioresources>
- [35]. G. L. Long, G. D. Winefordner, Limit of detection. A closer look at the IUPAC definition, *Analytical Chemistry*, Vol. 55, Issue 7, 1983, pp. 712A-724A.
- [36]. D. L. Nelson, M. M. Cox, Leningher: Principios de Bioquímica, 5<sup>a</sup> Ed. Editorial, Omega, Barcelona, España, 2007.
- [37]. L. W. Aurand, A. E. Woods, M. R. Wells, Lipids, *Food Composition and Analysis, Van Nostrand Reinhold Company*, New York, 1987, pp. 283-348.
- [38]. Alvarado-Gómez, A., Alonso-Lomillo M., Domínguez-Renedo O., Arcos-Martínez M., A Chronoamperometric Screen Printed Carbon Biosensor Based on Alkaline Phosphatase Inhibition for W(IV) Determination in Water, Using 2-Phospho-l-Ascorbic Acid Trisodium Salt as a Substrate, *Sensors*, Vol. 15, Issue 2, 2015, pp. 2232-2243.
- [39]. M. Bálintová, A. Petriláková, Study of pH Influence on Selective Precipitation of Heavy Metals from Acid Mine Drainage, *Chemical Engineering Transactions*, 2011, pp. 345-350.



Published by International Frequency Sensor Association (IFSA) Publishing, S. L., 2017 (<http://www.sensorsportal.com>).

# SENSORS & TRANSDUCERS

The Global Impact Factor of the journal is **0.987**

Open access, peer reviewed, established, international journal devoted to research, development and applications of sensors, transducers and sensor systems.

Published monthly by International Frequency Sensor Association (IFSA Publishing, S.L.) in print and electronic versions (ISSN 2306-8515, e-ISSN 1726-5479)



Submit your article at:  
<http://www.sensorsportal.com/HTML/DIGEST/Submition.htm>

## NANOSENSORS: Materials and Technologies

Hardcover: ISBN 978-84-616-5378-2  
e-Book: ISBN 978-84-616-5422-2



Nada F. Atta, Ed.



*Nanosensors: Materials and Technologies* aims to provide the readers with some of the most recent development of new and advanced materials such as carbon nanotubes, graphene, sol-gel films, self-assembly layers in presence of surface active agents, nano-particles, and conducting polymers in the surface structuring for sensing applications. The emphasis of the presentations is devoted to the difference in properties and its relation to the mechanism of detection and specificity. Miniaturization on the other hand, is of unique importance for sensors applications. The chapters of this book present the usage of robust, small, sensitive and reliable sensors that take advantage of the growing interest in nano-structures. Different chemical species are taken as good example of the determination of different chemical substances industrially, medically and environmentally. A separate chapter in this book will be devoted to molecular recognition using surface templating.

The present book will find a large audience of specialists and scientists or engineers working in the area of sensors and its technological applications. The *Nanosensors: Materials and Technologies* will also be useful for researchers working in the field of electrochemical and biosensors since it presents a collection of achievements in different areas of sensors applications.

Order: [http://www.sensorsportal.com/HTML/BOOKSTORE/Nanosensors\\_IFSA.htm](http://www.sensorsportal.com/HTML/BOOKSTORE/Nanosensors_IFSA.htm)

## Optimum Combination and Effect Analysis of Piezoresistor Dimensions in Micro Piezoresistive Pressure Sensor Using Design of Experiments and ANOVA: a Taguchi Approach

**Kirankumar B. Balavalad and B. G. Sheeparamatti**

Department of Electronics and Communication Engineering, Basaveshwar Engineering College,  
Bagalkot-587103, Karnataka, India (Affiliated to VTU, Belagavi, Karnataka, India)  
E-mail: kiranb4004@gmail.com, sheepar@yahoo.com

*Received: 8 March 2017 /Accepted: 10 April 2017 /Published: 30 April 2017*

---

**Abstract:** Piezoresistive (PZR) pressure sensors have gained importance because of their robust construction, high sensitivity and good linearity. The conventional PZR pressure sensor consists of 4 piezoresistors placed on diaphragm and are connected in the form of Wheatstone bridge. These sensors convert stress applied on them into change in resistance, which is quantified into voltage using Wheatstone bridge mechanism. It is observed from the literature that, the dimensions of piezoresistors are very crucial in the performance of the piezoresistive pressure sensor. This paper presents, a novel mechanism of finding best combinations and effect of individual piezoresistors dimensions viz., Length, Width and Thickness, using DoE and ANOVA (Analysis of Variance) method, following Taguchi experimentation approach. The paper presents a unique method to find optimum combination of piezoresistors dimensions and also clearly illustrates the effect the dimensions on the output of the sensor. The optimum combinations and the output response of sensor is predicted using DoE and the validation simulation is done. The result of the validation simulation is compared with the predicted value of sensor response i.e.,  $V$ . Predicted value of  $V$  is 1.074 V and the validation simulation gave the response for  $V$  as 1.19 V. This actually validates that the model (DoE and ANOVA) is adequate in describing  $V$  in terms of the variables defined.

**Keywords:** MEMS, Pressure sensors, Piezoresistive pressure sensors, DoE, ANOVA.

---

### 1. Introduction

MEMS technology combines silicon based MEMS are one of the promising process technologies which are responsible for the fabrication of tiny-integrated devices [1]. Micro sensors are the miniaturized devices that sense the environmental factors like pressure, temperature and light in general. Micro-pressure sensors sense and detect the change in pressure. There are pressure sensors which work

on different transduction mechanisms like capacitive, piezoelectric, resonant and piezoresistive. Compared to all other pressure sensors, piezoresistive pressure sensor (PZRPS) achieves high sensitivity and better linearity [2]. MEMS pressure sensors have a wide horizon of applications including automobiles, industries, defense and domestic. Automotive sector remains the biggest area for MEMS pressure sensors [3-5]. Primitive pressure sensors were developed using strain gauge mechanism but now there has been

a rapid development both in fabrication capabilities and packaging, after finding piezoresistivity in silicon and germanium [6-7]. Typically PZRPS are designed, analyzed and validated using Wheatstone bridge configuration. The piezoresistors are placed or diffused using boron diffusion on selected regions of maximum stress onto silicon diaphragm. Then these resistors are connected in the form of Wheatstone bridge [8]. Paper [9] presented, several types of semiconductor stress gauges to measure the longitudinal, transverse, shear stress and torque, and employed a Wheatstone bridge type gauge in mechanical signal sensing. Kanda's [10] model is referred for proper designing of the model in order to improve the performance of the sensor. The work in [11] presents the simulation and sensitivity analysis of four different models such as, piezoresistive pressure sensor by Lynn Fuller, Silicon pressure transducer by M. Bao, Pressure sensor die by Tai-Ran Hsu and Motorola Xducer Piezoresistor. [12] describes about the better techniques to enhance the performance of the sensor, designing sensor with optimized geometry of the diaphragm. Also shape and location of the piezoresistors are considered for better sensitivity.

Authors in [13] have analyzed relationship between the different dimensions of a square and circular diaphragm with Piezoresistors for a pressure range of 0 to 1MPa. Results show that the square diaphragm has the highest induced stress for a given pressure. The paper suggests that the square diaphragm is preferred for high pressure generating high stress. Paper [14] presents the design and simulation of MEMS Piezoresistive pressure sensor for the pressure sensing range of 0 to 1.1 bar. Authors present different configuration of piezoresistor placement using meander shape with different number of turns to enhance sensitivity. Diaphragm is an important part of the sensor and scholars have worked on optimization of the diaphragm to improve the performance of the sensor. Paper [15] presents, optimization of a piezoresistive MEMS pressure sensor to find an optimal diaphragm shape by Finite Element Method using ABAQUS®. Three different shapes of diaphragms are considered in this study, they are circular, square and rectangular diaphragms. There are works in literature, worked on finding the optimum combination of piezoresistors dimensions to obtain better output voltage and sensitivity. Taguchi method has been utilized for optimization in literature, paper [16] presents the use of Taguchi and Two-Level Factorial approach to optimize the size of diaphragm thickness, slot width, and slot length for capacitive sensor.

Paper [17], has used Taguchi method to understand the effect of parameters in analyzing the silicon piezoresistive pressure sensor. There are works on studying the effect of piezoresistor dimensions, paper [8] presents design of silicon based piezoresistive micro pressure sensor. Finite Element Analysis is used find the effect of design parameters like the side length and the thickness of

the diaphragm in determining the sensitivity of the sensor. The paper makes an effort to determine the optimum length and positioning of piezoresistors. Our previous work [18] describes the design and simulation of micro piezoresistive pressure sensor for pressure range of 0 to 1 MPa. The work considers placement of piezoresistors at maximum stress area and piezoresistor dimensions were varied to find the better combination. All the works mentioned, considers the placement of resistors at maximum stress area. But there are very little works which explains the individual resistor dimensions viz., length, width and thickness effect on the output of the sensor. In this work DoE and ANOVA (Analysis of Means) using Taguchi method are in used to find the best combination of piezoresistors dimensions and to analyze the effect of individual piezoresistor dimensions on the output of the sensor. This paper is the first of its kind in find the optimized dimensions and illustrate the individual piezoresistor effect on sensor performance using DoE and ANOVA.

Organization of the paper: Section 2 illustrates the design of the piezoresistive pressure sensor, in Section 3 describes the use of DoE to find the optimum combinations of piezoresistors for high sensor response (output voltage). Section 4 describes the use of ANOVA to analyze the effect of piezoresistor dimensions on the sensor performance. Section 5 proposes conclusion.

## 2. Design of Piezoresistive Pressure Sensor

Piezoresistive pressure sensor is designed with placing four piezoresistors on a square diaphragm. The diaphragm dimension is  $400\ \mu\text{m} \times 400\ \mu\text{m}$  and  $10\ \mu\text{m}$  thickness (Fig. 1) [18].

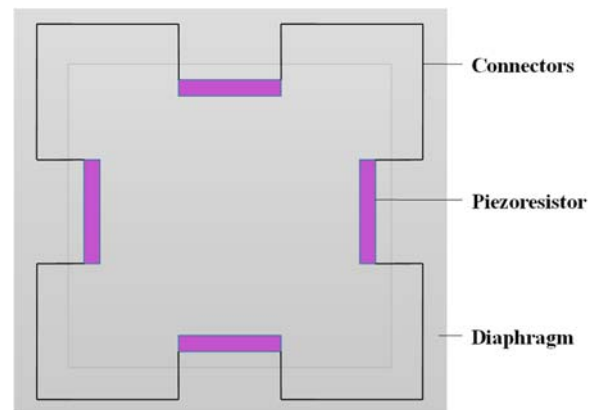


Fig. 1. Piezoresistor pressure sensor schematic view.

P-type silicon piezoresistors are used as they exhibit good gauge factor compared to n-type. Diaphragm is considered as n-type silicon. Cr and Al is used as connectors. Cr is usually considered to have a bonding between the semiconductor and the metal contact. The properties of the materials used

for simulation are mentioned in Table 1. Resistors and connectors are configured in the form of Wheatstone bridge with applied input voltage of 5 V. Initially the bridge is balanced with a small offset voltage. Pressure is applied to the back side of the diaphragm, as shown in Fig. 2.

**Table 1.** Material properties of the model.

Material Property	P-type Silicon (Piezoresistors)	N-type Silicon (Diaphragm)
Young's Modulus	129 GPa	170 GPa
Poisson's ratio	0.22	0.28
Density	2330 [kgm <sup>-3</sup> ]	2330 [kgm <sup>-3</sup> ]

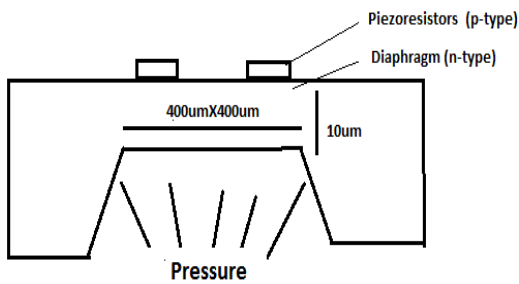


**Fig. 2.** Piezoresistive Pressure Sensor.

Pressure is varied from 0 to 1 MPa following the design aspects mentioned in our previous work [18] i.e., diaphragm thickness 10  $\mu\text{m}$  is considered, keeping fabrication aspects in mind. For diaphragm dimensions, the concept of thin plate theory has been included, according to which the length of the diaphragm must be at least  $10 \mu\text{m} \times 20 = 200 \mu\text{m}$  [19]. Small deflection theory of bending of thin plates says that, the maximum deflection must be within  $1/5^{\text{th}}$  of the thickness of the diaphragm. So the diaphragm with  $10 \mu\text{m}$  thickness should have deflection around  $2 \mu\text{m}$ . The diaphragm dimensions were finally fixed by carrying out simulation of maximum deflection v/s diaphragm dimensions. Simulation results show that the maximum diaphragm dimension should be  $400 \mu\text{m} \times 400 \mu\text{m}$  and the results are mentioned in Table 2.

**Table 2.** Diaphragm dimension and displacement.

Diaphragm Thickness ( $\mu\text{m}$ )	Diaphragm Size ( $\mu\text{m}^2$ )	Max. Displacement ( $\mu\text{m}$ )
10	$400 \times 400$	2.6254
10	$500 \times 500$	6.3379
10	$600 \times 600$	13.024

The designed models are simulated using COMSOL Multiphysics. The designed models are simulated for the pressure range of 0 to 1 MPa. The potential distribution plot is shown in Fig. 3 for input voltage of 5 V.

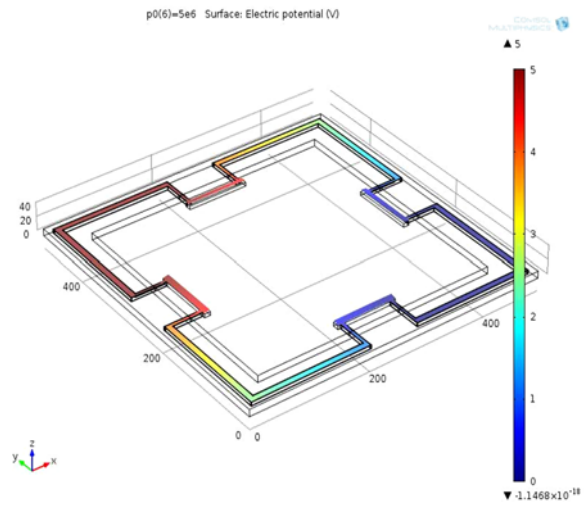


**Fig. 3.** Electric potential of the PZR pressure sensor.

### 3. DoE: A Taguchi Approach to Find Optimum Combination of Piezoresistor Dimensions

Basically the paper follows Design of Experiments using Taguchi methods. Taguchi method is also known as robust design method. This method considers first the number of parameters influencing the quality characteristics/responses of the devices [20]. Typically, a process optimization will have several control factors which directly decide the desired value of the output. The optimization process then involves determining the best control factor levels so that the output is at the desired level [21]. In this case the design set up and performance parameters are described in Fig. 4.

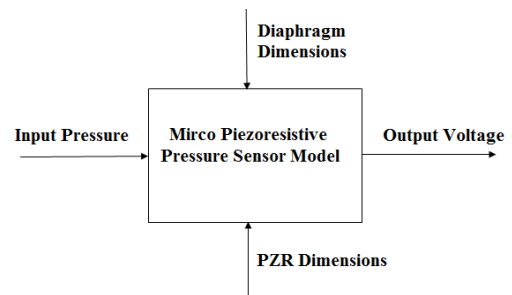


**Fig. 4.** Signal Factor diagram for DoE.

Pressure is input to the sensor, the performance of the sensor in normal operating conditions mainly depend upon, diaphragm dimensions and piezoresistor dimensions. In this work the focus in on finding the effect of individual resistor dimensions on the performance of the sensor, keeping all other conditions ideal. Although temperature is one of the noise factors which affect the performance of the sensor, it is not considered here as the focus is on PZR dimensions optimization. DoE was performed with varying dimensions of piezoresistors with predefined combinations following L9 orthogonal

array. Although DoE gives insight about the effect and optimum piezoresistor combinations, there is one more method called ANOVA (Analysis of Means), which gives a better insight of effect analysis of individual dimension effect analysis. In this work both DoE and ANOVA are used to serve the cause.

The factors affecting the sensor performance are piezoresistor dimensions viz., 1. Length (A). 2. Width (B). 3. Thickness (C).

The above mentioned factors are taken here for effect analysis and to find the optimum combinations. Each of these factors (A, B, C) are assigned with the three distinct levels. The level assignment is based on the literature studies and the papers (works on piezoresistor pressure sensors) that we have published. The literature reveals that the lower bound on the piezoresistor length is 50  $\mu\text{m}$ , for width it is 5  $\mu\text{m}$  and for thickness it is 4  $\mu\text{m}$  (and below). The upper bound happens to be 100 $\mu\text{m}$  for length, 15  $\mu\text{m}$  for width and 6 $\mu\text{m}$  for thickness. Table 3, presents the factors and their levels assigned.

**Table 3.** Factors and their levels.

Factors	Level 1	Level 2	Level 3
Length (A)	50 $\mu\text{m}$	75 $\mu\text{m}$	100 $\mu\text{m}$
Width (B)	5 $\mu\text{m}$	10 $\mu\text{m}$	15 $\mu\text{m}$
Thickness (C)	4 $\mu\text{m}$	5 $\mu\text{m}$	6 $\mu\text{m}$

For the levels assigned, the simulation was conducted as per the L9 orthogonal array, which is a standard array. In this array 1, 2, 3 represent the levels of respective factors. In the array, for any pair of columns, all combinations of factor levels occur and they occur equal number of times, hence the array is orthogonal. The last column of the Table 3, represents the responses, i.e., output voltage of the sensor. Simulation was conducted for six repeated times and an average value is taken for say experiment  $i$ , where  $i = 1, 2, 3, \dots, 9$  different experiments/simulation combinations. The factors, their combination and the simulation results are tabulated in Table 4.

**Table 4.** Experiment as per L9 orthogonal array.

Expt. No	Column Number and Factor Assigned			Output Voltage 'V' (mV) at 1MPa of input pressure
	1. Length (A)	2. Width (B)	3. Thickness (C)	
1	1	1	1	$V_1=348.02$
2	1	2	2	$V_2=203.73$
3	1	3	3	$V_3=183.69$
4	2	1	2	$V_4=769.93$
5	2	2	3	$V_5=424.22$
6	2	3	1	$V_6=351.35$
7	3	1	3	$V_7=1169$
8	3	2	1	$V_8=715.37$
9	3	3	2	$V_9=483.67$

From the response data in the Table 3, the overall mean is computed, as

$$m = \frac{1}{9} \sum_{i=1}^9 V_i = \frac{1}{9} [V_1 + V_2 + \dots + V_9] = 516.54 \text{ mV}$$

### 3.1. Effect of Factors at Different Levels

This section presents the effect of the Length, Width and Thickness factors at different levels. All the mean values and effect values are in mV.

#### 3.1.1. Effect of Length (A) at Different Levels

The effect of Length (A) at level 3 is given by the result of experiment number 7, 8, 9.

$$m_{A3} = \frac{1}{3} [V_7 + V_8 + V_9] = 789.34$$

The effect of Length (A) at level 2 is given by the result of experiment number 4, 5, 6.

$$m_{A2} = \frac{1}{3} [V_4 + V_5 + V_6] = 515.16$$

The effect of Length (A) at level 1 is given by the result of experiment number 1, 2, 3.

$$m_{A1} = \frac{1}{3} [V_1 + V_2 + V_3] = 245.14$$

The effect of length (A) at level A3 is given by,  $(m_{A3-m}) = 272.8$ .

The effect of length (A) at level A2 is given by,  $(m_{A2-m}) = -1.38$ .

The effect of length (A) at level A1 is given by,  $(m_{A1-m}) = -271.40$ .

#### 3.1.2. Effect of Width (B) at Different Levels

The effect of Width (B) at level 3 is given by the result of experiment number 3, 6, 9.

$$m_{B3} = \frac{1}{3} [V_3 + V_6 + V_9] = 339.57$$

The effect of Width (B) at level 2 is given by the result of experiment number 2, 5, 8.

$$m_{B2} = \frac{1}{3} [V_2 + V_5 + V_8] = 447.77$$

The effect of Width (B) at level 1 is given by the result of experiment number 1, 4, 7.

$$m_{B1} = \frac{1}{3} [V_1 + V_4 + V_7] = 762.31$$



The effect of Width (B) at level B3 is given by,  $(m_{B3}-m) = -176.97$ .

The effect of Width (B) at level B2 is given by,  $(m_{B2}-m) = -68.77$ .

The effect of Width (B) at level B1 is given by,  $(m_{B1}-m) = 245.77$ .

### 3.1.3. Effect of Thickness (C) at Different Levels

The effect of Thickness (C) at level 3 is given by the result of experiment number 3, 5, 7.

$$m_{C3} = \frac{1}{3} [V_3 + V_5 + V_7] = 592.30$$

The effect of Thickness (C) at level 2 is given by the result of experiment number 2, 4, 9.

$$m_{C2} = \frac{1}{3} [V_2 + V_4 + V_9] = 485.77$$

The effect of Thickness (C) at level 1 is given by the result of experiment number 1, 6, 8.

$$m_{C1} = \frac{1}{3} [V_1 + V_6 + V_8] = 471.58$$

The effect of Thickness (C) at level C3 is given by,  $(m_{C3}-m) = 75.76$ .

The effect of Thickness (C) at level C2 is given by,  $(m_{C2}-m) = -30.77$ .

The effect of Thickness (C) at level C1 is given by,  $(m_{C1}-m) = -44.96$ .

All the above calculations are theoretical. The same was implemented using Minitab 17 software the results show exact similarities to the theoretical. The individual analysis of means for Length, width and thickness are plotted in Figs. 5, 6, 7. All the factors effects can be plotted in the form of means plots as shown in Fig. 8.

Above figure shows the analysis of means for length factor of piezoresistor. This mean is around the overall mean. Where  $\alpha$  is the maximum acceptable level of risk for rejecting a true null hypothesis. It is expressed as a probability ranging between 0 and 1. A is frequently referred to as the level of significance, it should be set before beginning the analysis. The most commonly used  $\alpha$ -level is 0.05. At this level, the chance of finding an effect that does not really exist is only 5%. Fig. 7, describes the means plot for piezoresistor thickness factor. All level factor effects can be observed that they are near to overall mean.

The combined plot of analysis of means for all three factors is shown in Fig. 8.

The interaction plot of the 3 factors is plotted in Fig. 9. The plot considers the interaction of all factors, keeping one factor constant and varying other two. This plot gives better insight on optimum levels and combinations desired.

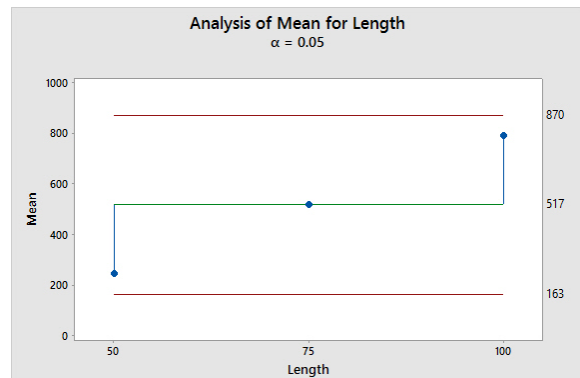


Fig. 5. Analysis of Mean for Length.

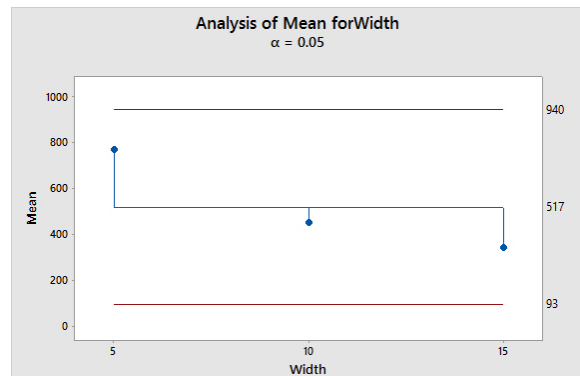


Fig. 6. Analysis of Mean for Width.

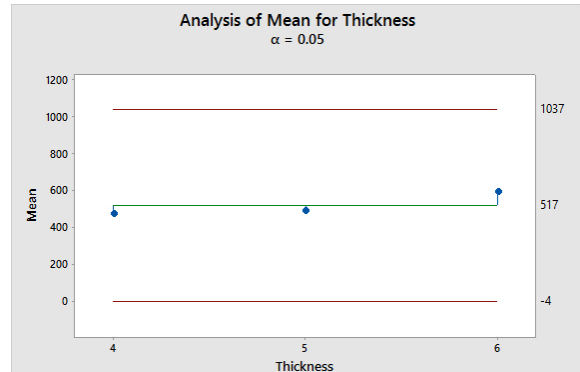


Fig. 7. Analysis of Mean for Thickness.

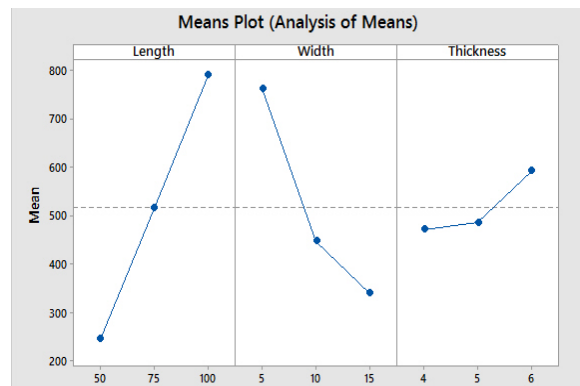


Fig. 8. Analysis of Means for the factors.

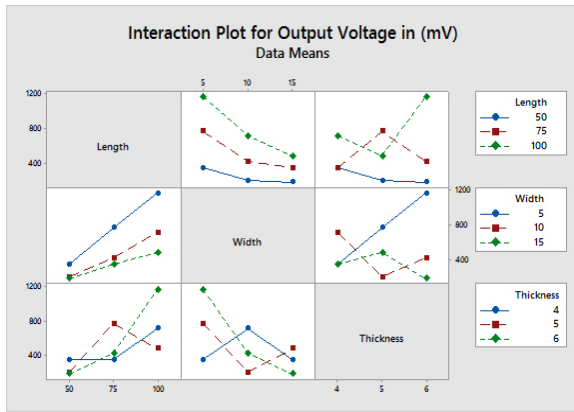


Fig. 9. Interaction plot for 3 factors.

Based on the theoretical calculation, observations and plots using Minitab 17, now we can find the optimum combinations of factors. The optimum combinations are indicated where the contribution of the level to deviate away from the mean. Table 5, presents the optimum levels indicated with \* mark.

Table 5. Optimum Combinations.

Factors	Levels		
	1	2	3
A Length	245.14	515.16	789.34*
B Width	762.31*	447.77	339.57
C Thickness	471.58	485.77	592.30*

The means plot describes thickness has got least effect, so it can be neglected while considering the combinations. But considering all factor effects the optimum combinations to have enhancement in output voltage the combinations need to be preferred are  $A_3B_1C_3$  or  $A_3B_1C_2$ . Minitab 17 was trained for optimum combinations, and the following plot shows the required combinations with levels, which are in accordance with the calculated optimum combinations. The optimum combinations with levels are plotted in Fig. 10.

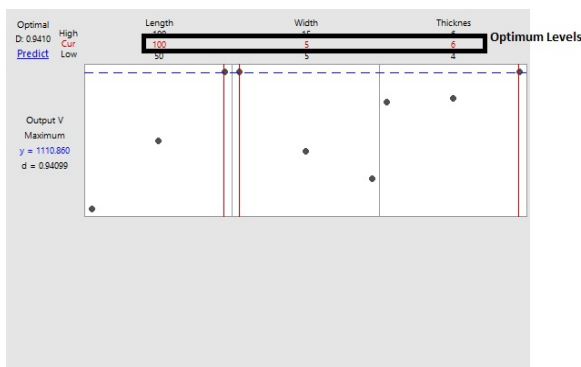


Fig. 10. Optimization Plot.

The objective of the Taguchi methods is to predict optimum condition/combinations. The optimum predicted conditions as mentioned in the Table 5  $A_3B_1C_3$ . Using the additive model, the value of V under optimum combinations as,

$$V = m + (m_{A3} - m) + (m_{B1} - m) + (m_{C3} - m) = 1.074V$$

A verification simulation is conducted after determining the optimum conditions and predicting the response with these combinations. The result of the verification simulation is compared with the predicted value of V. Predicted value of V is 1.074 V and the verification simulation gave the response for V as 1.19 V. So this actually concludes that this model is adequate in describing V in terms of the variables defined.

#### 4. ANOVA: Analysis of Means Approach to Find the Effect of Piezoresistor Dimension of Sensor Response

The effect of different factors of piezoresistor and an optimized levels and combinations were defined using means plot in the previous section. But the better insight of relative effect of different factors can be obtained by decomposition of variance, known as Analysis of Variance (ANOVA). ANOVA also provides the variance for the factor effects and variance of the prediction error. It involves three decompositions viz., grand sum of squares, sum of squares due to mean and total sum of squares.

Where **Total sum of squares = (Grand sum of squares – sum of squares due to mean)**

The model of experimentation is same as defined in Section 3 following Fig. 4. All factor and their levels defined in above section i.e., in DoE are followed in this section too. Same responses i.e., the output voltage for input pressure of 1 MPa is considered for ANOVA.

#### ANOVA:

1. Grand Sum of Squares (GSS) is given by  $GSS = \sum_{i=1}^9 V_i^2 = 3204819.33 \text{ (mV)}^2$
2. Sum of Squares due to Mean (GSM) is given by  $GSM = (\text{number of experiments})Xm^2 = 9(516.54)^2 = 2401322.14 \text{ (mV)}^2$
3. The Total Sum of Squares (TSS) is given by  $TSS = \sum_{i=1}^9 (V_i - m)^2 = 803373.24 \text{ (mV)}^2$
4.  $TSS = GSS - GSM = 3204819.33 - 2401322.14 \approx 803497.19 \text{ (mV)}^2$
5. Sum of Squares due to individual factors
  - 1) Sum of squares due to Factor A. Length  $= [3(m_{A1}-m)^2 + 3(m_{A2}-m)^2 + 3(m_{A3}-m)^2] = 444239.11 \text{ (mV)}^2$

- 2) Sum of Squares due to Factor B. Width  
 $= [3(m_{B1}-m)^2 + 3(m_{B2}-m)^2 + 3(m_{B3}-m)^2]$   
 $= 289351.74 \text{ (mV)}^2$
- 3) Sum of Squares due to Factor C. Thickness  
 $= [3(m_{C1}-m)^2 + 3(m_{C2}-m)^2 + 3(m_{C3}-m)^2]$   
 $= 26123.30 \text{ (mV)}^2$

Based on the above findings, ANOVA table is prepared, and is shown in Table 6.

**Table 6.** ANOVA table.

Factors	DoF	Sum of Squares	Mean Squares	F Ratio
A. Length	2	444239.11	222119.55	1.211
B. Width	2	289351.74	144675.87	0.78
C. Thickness	2	26123.30	13061.65	0.007
Error	0	0	----	
Total	6	759714.15	----	
(Error)	4	733590.85	183397.71	

The above table is prepared by neglecting the effect of factor C-Thickness, as it has minimum effect.

DoF - Degree of Freedom. F ratio is calculated by  $F = \text{Mean square value/error}$ .

From ANOVA Table 6, factor A is responsible for  $(444239.11/759714.15) = 58.47\%$  percent of variation of V (output voltage). Similarly All factor effects are tabulated in Table 7.

**Table 7.** Effect of individual factors on the output of sensor.

Factors	Percentage effect of factors for variation in output voltage in ‘%’
Length of piezoresistor	58.47
Width of piezoresistor	38.08
Thickness of piezoresistor	3.43

## 5. Conclusions

The paper presents a very unique and novel technique of finding the individual effect of piezoresistor dimensions on the output of the sensor and the optimum combinations of levels required to enhance the output voltage. Design of Experiment and ANOVA methods are used to achieve the purpose. The results and observations suggest the best combination of levels to optimize the response of the sensor is  $A_3B_1C_3$  i.e.,  $100 \mu\text{m} \times 5 \mu\text{m} \times 6 \mu\text{m}$ . The predicted response after optimization (using DoE) was 1.074 V and the validation simulation using the optimum combinations shows the response value of 1.19 V. And ANOVA method describes that the effect of Length of the piezoresistor has highest effect on the output variations of the sensor. Length

has 58.74 % effect next is width with 38.08 % effect and least is the effect of thickness 3.43 %. Therefore to enhance the output response of the sensor, length of piezoresistor has to be carefully addressed.

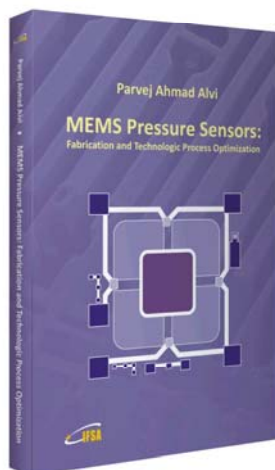
## References

- [1]. Madhab G. B., Intelligent Microsystems: an Overview, in *Proceedings of the Student Conference on Engineering, Sciences and Technology*, 30-31 Dec. 2004, pp. 54-59.
- [2]. K. N. Bhat, M. M. Nayak, MEMS Pressure Sensor- An overview of challenges in ‘Technology and Packaging’, *Journal of ISSS*, Vol. 2, No. 1, March 2013, pp. 39-71.
- [3]. Mohan A., Malshe A. P., Aravamudhan S., Bhansali S., Piezoresistive MEMS pressure sensor and packaging for harsh oceanic environment, in *Proceedings of the 54<sup>th</sup> Conference on Electronic Components and Technology*, Vol. 1, 1-4 June 2004, pp. 948-950.
- [4]. Lung-Tai Chen, Jin-Sheng Chang, Chung-Yi Hsu, Wood-Hi Cheng, Fabrication and Performance of MEMS-Based Pressure Sensor Packages Using Patterned Ultra-Thick Photoresists, *Sensors*, Vol. 9, 2009, pp. 6200-6218.
- [5]. MEMS Market Overview: Steady Growth for MEMS in 2013 and beyond, in *Proceedings of the MEMS Tech Seminar*, Castelletto, September 2013.
- [6]. Tufte O. N., Chapman P. W., Long D., Silicon diffused-element Piezoresistive diaphragms, *Journal of Applied Physics*, Vol. 33, No. 11, 1962, pp. 3322-3327.
- [7]. Jeff Melzak, Nelsimar Vandelli, SiC MEMS Pressure Sensors: Technology, Applications and Markets, *PLXMicro, Inc.*
- [8]. K. Y. Madhavi, M. Kirshna, C. S. Chandrasekhara, Design of a Piezoresistive Micropressure Sensor Using Finite Element Analysis, *International Journal of Computer Applications*, Vol. 70, No. 3, May 2013, pp. 20-26.
- [9]. P.J. French and A.G.R. Evans, Piezoresistance in Polysilicon and Its Applications to Strain Gauges, *Solid-State Electronics*, Vol.32, No.1, pp.1-10, 1989.
- [10]. Y. Kanda, Optimum Design Considerations for Silicon Piezoresistive Pressure Sensor, *Sensor and Actuators A: Physical*, Vol. 62, No. 1-3, 1997, pp. 539-542.
- [11]. S Meenatchisundaram, S. M. Kulkarni, Sensitivity Analysis of Different Models of Piezoresistive Micro Pressure Sensors, in *Proceedings of the Comsol Conference Bangalore*, 2013.
- [12]. U. Sampath Kumar, N. Jagadesh Babu, Design and Simulation of MEMS Piezoresistive Pressure Sensor to Improve the Sensitivity, *International Journal of Innovative Research in Electrical, Electronics, Instrumentation and Control Engineering*, Vol. 3, Issue 3, March 2015.
- [13]. Avishek Ghosh, Sunipa Roy and C. K. Sarkar, Design and Simulation of MEMS Based Piezoresistive pressure Sensor for Enhanced Sensitivity, *IEEE*, 978-1-4673-6150-7/13, 2013.
- [14]. S. Snatosh Kumar, Anuj Kumar Ojha, Ramprasad Nambisan, Anil Kumar Sharma, B. D. Pant, Design & Simulation of MEMS Silicon Piezoresistive Pressure Sensor for Barometric Applications, *Elsevier*, 2013, pp. 339-345.

- [15]. Nabiollah Abol Fathi, Zohreh Allah Moradi, Design and Optimization of Piezoresistive MEMS Pressure Sensors Using ABAQUS, *Middle-East Journal of Scientific Research*, Vol. 21, Issue 12, 2014, pp. 2299-2305.
- [16]. M. Ali, A. C. W. Noorakma, N. Yusof, W. N. F. Mohamad, N. Soin, S. F. W. M. Hatta, Optimization of MEMS intraocular capacitive pressure sensor, in *Proceedings of the IEEE International Conference on Semiconductor Electronics (ICSE)*, Kuala Lumpur, 2016, pp. 173-176.
- [17]. Tai-Kang Shing, Robust design of Silicon Piezoresistive Pressure Sensor, in *Proceedings of the International Conference on Modeling and Simulation of Microsystems*, Taiwan, 1998, pp. 597-601. <http://www.nsti.org/publications/MSM/98/pdf/T3707.pdf>
- [18]. Kirankumar B. Balavalad, B. G. Sheeparamatti, Design, Simulation and Analyses of Piezoresistive Micro Pressure Sensor for Pressure Range of 0 to 1MPa, in *Proceedings of the IEEE International Conference on Electrical, Electronics, Communication, Computer Technologies and Optimization Techniques (ICEECCOT)*, 2017.
- [19]. L. Herrera-May, *et al.*, Electromechanical analysis of a piezoresistive pressure micro-sensor for low-pressure biomedical applications, *Revista Mexicana de Fisica*, Vol. 55, No. 1, 2009, pp. 14-24.
- [20]. Madhav Padke, Quality Engineering Using Robust Design, *Prentice Hall*, 1989.
- [21]. [https://www.ee.iitb.ac.in/~apte/CV\\_PRA\\_TAGUCHIINTRO.htm](https://www.ee.iitb.ac.in/~apte/CV_PRA_TAGUCHIINTRO.htm)



Published by International Frequency Sensor Association (IFSA) Publishing, S. L., 2017 (<http://www.sensorsportal.com>).



Hardcover: ISBN 978-84-616-2207-8  
e-Book: ISBN 978-84-616-2438-6

So far, no book has described the step by step fabrication process sequence along with flow chart for fabrication of micro pressure sensors, and therefore, the book has been written taking into account various aspects of fabrication and designing of the pressure sensors as well as fabrication process optimization. A complete experimental detail before and after each step of fabrication of the sensor has also been discussed. This leads to the uniqueness of the book.

Features include:

A complete detail of designing and fabrication of MEMS based pressure sensor.

- Step by step fabrication and process optimization sequence along with flow chart, which is not discussed in other books.
- Description of novel technique (lateral front side etching technique) in terms of chip size reduction and fabrication cost reduction, and comparative study on both the techniques (i.e. Front Side Normal Etching Technology and Front Side Lateral Etching Technology) for the fabrication of thin membrane.
- Discussion on issues of sealing of conical tiny cavity; because the range of pressure applied (i.e. greater or less than atmospheric pressure) can be decided by methodology of sealing of tiny cavity.
- A complete theoretical detail regarding aspects of designing and fabrication, and experimental results before and after each step of fabrication.

**MEMS Pressure Sensors: Fabrication and Process Optimization** will greatly benefit undergraduate and postgraduate students of MEMS and NEMS courses. Process engineers and technologists in the microelectronics industry including MEMS-based sensors manufacturers.

Order: [http://www.sensorsportal.com/HTML/BOOKSTORE/MEMS\\_Pressure\\_Sensors.htm](http://www.sensorsportal.com/HTML/BOOKSTORE/MEMS_Pressure_Sensors.htm)

## Effect of Annealing and Operating Substrate Temperature on Methanol Gas Sensing Properties of SnO<sub>2</sub> Thin Films

<sup>1,\*</sup> Priyanka Kakoty, <sup>1</sup> Manabendra Bhuyan and <sup>2</sup> Karen Das

<sup>1</sup> Tezpur University, Tezpur, Assam, India

<sup>2</sup> Assam Don Bosco University, Guwahati, Assam, India

\* E-mail: priyankak@tezu.ernet.in

Received: 2 February 2017 / Accepted: 31 March 2017 / Published: 30 April 2017

**Abstract:** SnO<sub>2</sub> based sensing nano-material have been synthesized by simple chemical route using Stannic (IV) chloride-pentahydrate (SnCl<sub>4</sub>.5H<sub>2</sub>O) as precursor. The structural properties of the prepared SnO<sub>2</sub> nano-particles annealed at different temperatures have been characterized by X-ray diffraction (XRD) analysis. The XRD patterns showed pure bulk SnO<sub>2</sub> with a tetragonal rutile structure in the nano-powders. By increasing the annealing temperatures, the size of crystals were seen to increase, the diffraction peaks were found narrower and the intensity was higher. SnO<sub>2</sub> films prepared by spin coating the prepared nano-material solution was tested at different temperatures for methanol vapour and it showed that the film prepared from SnO<sub>2</sub> powder annealed at 500 °C shows the higher sensitivity to methanol vapour at 150 °C substrate temperature with significantly low response and recovery time.

**Keywords:** SnO<sub>2</sub> sensing material, Annealing, Methanol, Gas sensor.

### 1. Introduction

Methanol is an extremely lethal organic solvent and is often fatal to living beings. It is highly carcinogenic and may cause serious adverse effect on health and environment. Significant exposure of methanol can cause bronchial constriction, narrowing of airways, increased pulmonary resistance, changes in metabolism and even irritation to mucus membrane in eyes [1]. But in the field of manufacturing of drugs, perfumes, dyes, power sources, etc., methanol has extensive applications [2]. So although methanol is harmful, use of this solvent is almost unavoidable. Therefore, a methanol sensor is in huge demand which has reliability in detection. Detection of methanol at low concentration levels would be even more important as small amount of leakage to the environment could be detected and necessary measures could be taken to save the living beings as

well as the environment from any danger from methanol.

Researchers have reported the use of many metal oxides for methanol sensing in many different forms like nanorods, nanosheets, nanoribbons, nanobelts, thick film, thin film, etc., among which SnO<sub>2</sub> is established as a popular choice owing to its various physical characteristics [3]. It is an n-type wide bandgap (3.6 eV) semiconductor that shows high sensitivity to volatile gases, stability, non-toxicity an abundancy. SnO<sub>2</sub> shows sensitivity to various oxidizing and reducing gases and has superior reproducibility. SnO<sub>2</sub> is a low cost material and has been developed as different structures for sensing various oxidizing and reducing gases. SnO<sub>2</sub> have been studied for alcohol gas sensors [4], H<sub>2</sub>S gas sensor [5], ammonia sensor [6], CO<sub>2</sub> gas sensor [7], NO<sub>2</sub> sensors [8]. Gases which are a subject of risk to the environment like combustible gases, organic vapours,

toxic gases needs to be controlled and SnO<sub>2</sub> have been extensively exploited for the purpose.

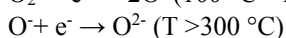
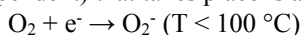
While preparing SnO<sub>2</sub> material for gas sensing applications, annealing is an important process that activates the material for the purpose of gas sensing. Annealing process confiscates the surface oxygen anions and leads to surface made of tin cations in various bonding arrangements and oxidation states with delocalized electronic structure [13]. Adsorption of various gases onto the surface of the treated SnO<sub>2</sub> by annealing process alters the surface electronic properties and allows detection of gas through conductance measurements.

Herein, preparation of SnO<sub>2</sub> based gas sensor is presented which is developed using a simple wet chemical process for methanol sensing. In this paper, analysis of variations seen in the characteristics of the prepared SnO<sub>2</sub> material at different annealing temperatures is presented. This work brings forward the importance of selection of a proper annealing temperature for preparing SnO<sub>2</sub> for methanol sensing. This paper includes the description of chemisorption sensing reaction scheme of the gas sensor on exposure to methanol, the preparation of the sensing material, its structural as well as electrical characterization.

## 2. The Chemisorption Mechanism of the Sensor Towards Methanol

An adsorption/desorption process of oxygen and the gas molecules at the sensor surface governs the SnO<sub>2</sub> sensing mechanism. The chemical reaction mechanism is therefore very essential for portraying a clear view of the sensing operation.

During chemisorption reaction, when the SnO<sub>2</sub> film is heated in air, the atmospheric oxygen is converted to different ionic form such as O<sub>2</sub><sup>-</sup>, O<sup>-</sup>, O<sup>2-</sup> by acquiring the trapped electrons from the conduction band. The oxidation reaction (which is temperature dependent) that takes place is as follows [9]

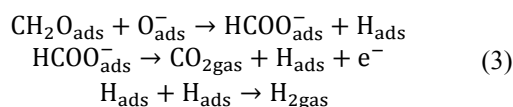
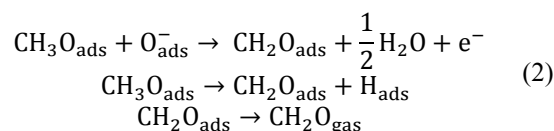


This oxidation reaction results in an energy band bending as the trapped oxygen gets reduced in number from the surface and oxygen in ionic form gets adsorbed on the SnO<sub>2</sub> surface which leads to an increase in resistance of the sensor film.

It was proposed in [10-13] that at an operating temperature between 100 °C - 300 °C, the sensitivity of pure SnO<sub>2</sub> film is maximized to reducing gases. For methanol, the absorbed alcohol molecules are very reactive and easily oxidize to form CO<sub>2</sub>. At this temperature range, the O<sup>-</sup> is highly active and acts as the dominating ionic species of oxygen present in the surface of the sensing layer. This ionic species thus turn as major adsorbed species that influence sensitivity of sensor element. On the other hand, O<sub>2</sub><sup>-</sup> is categorized as 'electrophilic' agent and O<sup>2-</sup> as 'nucleophilic' agent connected with the lattice at the

surface and are highly unstable and do not take significant role in inducing sensitivity. While O<sup>-</sup> dominates the decomposition reaction of methanol when exposed to the sensing surface layer. Methanol is initially adsorbed on the surface of SnO<sub>2</sub> as a form of methoxide (OCH<sub>3</sub>) and then reacts with adsorbed oxygen ions at the surface of SnO<sub>2</sub>.

Methanol mainly decomposes following the dehydrogenation path into formaldehyde and consequently into formic acid following the reaction steps releasing electrons into the conduction band as given below [1]:

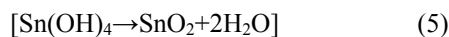
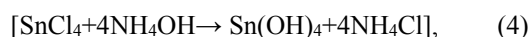


As shown in Equation (1), (2) and (3), methanol first decomposes into methoxy group (CH<sub>3</sub>O (ads)) which again decomposes into formaldehyde groups (CH<sub>2</sub>O (ads)). A part of this group also desorbs as CH<sub>2</sub>O (gas). The remaining CH<sub>2</sub>O reacts with adsorbed oxygen O<sub>ads</sub><sup>-</sup> resulting in species like HCOO<sup>-</sup> (ads) which is very unstable and so further decompose to CO<sub>2</sub>. Subsequently, the electrons are returned back to the metal oxide, which results in an increase of conductance. The hydrogen atoms combine to form molecular hydrogen gas. The increase in conductivity due to liberation of electrons back into the conduction band represents the response of the sensor.

## 3. Experimental

### 3.1. Sensing Material Preparation

The sample preparation procedure involves a low cost wet chemical method. Stannic (IV) chloride-pentahydrate (SnCl<sub>4</sub>.5H<sub>2</sub>O) (from Sigma Aldrich) is dissolved in distilled water to prepare 0.1 M solution to which NH<sub>4</sub>OH aqueous solution (1 mol/L) was added dropwise under constant stirring for 1hr to get white precipitate of pure SnO<sub>2</sub>. The pH of the solution was maintained at 10. The precipitate was further washed with ethanol and DI water to remove NH<sub>4</sub><sup>+</sup> and Cl<sup>-</sup> ions. AgNO<sub>3</sub> test was done to ensure removal of chloride ions from the precipitate. The samples were then preheated at 100 °C for 10 minute to remove organic residuals. Equations (4) and (5) shows the formation of SnO<sub>2</sub> through the chemical process steps.



### 3.2. Deposition of the Prepared Sensing Material on Si/SiO<sub>2</sub> Substrate:

A 3" Si wafer of <100> orientation was cleaned and then oxidized to form SiO<sub>2</sub> layer by PECVD deposition technique at pressure 0.8 torque at 250 °C for 150 sec. The prepared SnO<sub>2</sub> solution was then spin coated onto the substrate at 3000 r.p.m. for 60 sec after which the substrate was cut into five samples of 1.5 cm×1.5 cm and dried in an oven for 50-60 minutes maintaining the temperature within 90 °C to 100 °C. Then all the samples were annealed in a muffle furnace for 1hr to improve crystallinity of the sensing layer at five different temperatures of 200 °C, 300 °C, 400 °C, 500 °C and 600 °C.

The sensors were designed to operate in resistive mode for which wire bonding for electrical characterization was required. Thereby, metallization process was carried out in a vacuum coater at a pressure of 10<sup>-9</sup> mbar and 80A current. The active sensing layer was protected by an aluminium foil and the space for metallization was exposed to Pd vapours in the metallization chamber which resulted in formation of Pd film of 266 nm thickness over the exposed region. The model used for vacuum coating is "HINDHIVAC" Vacuum coating Unit Model (HHV BC-300). The contact pad dimension was 3 mm × 3 mm and the average distance between two lateral pads was 5 mm. Thin copper wires were used for wire connections using silver paste. The sample was then mounted on a glass slide and was kept in oven at 150 °C for 1hr so that the paste dries up and a proper

contact is made and then it was allowed to cool. The schematic diagram of the prepared sensor with its dimensions is shown in Fig. 1.

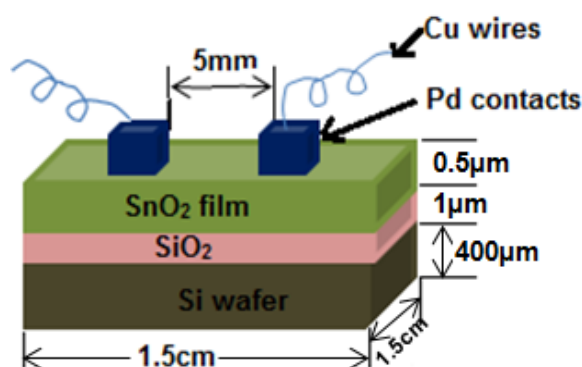


Fig. 1. The prepared sensor structure.

### 4. XRD Analysis

The crystalline structure analysis of the samples annealed at five different temperatures was carried out using X-ray Diffractometer (Bruker AXS, D8 focus) with CuK $\alpha$  radiation as an X-ray source at 40 kV and 30 mA in the scanning angle (2 $\theta$ ) from 10<sup>0</sup> to 70<sup>0</sup> with a scan speed of 0.02<sup>0</sup>/s. The samples shows major reflections at (110), (101), (200), (211), (220), (002), (310), (112) and (301) crystal planes. Fig. 2 shows the XRD of the five samples and their variations in crystalline structure.

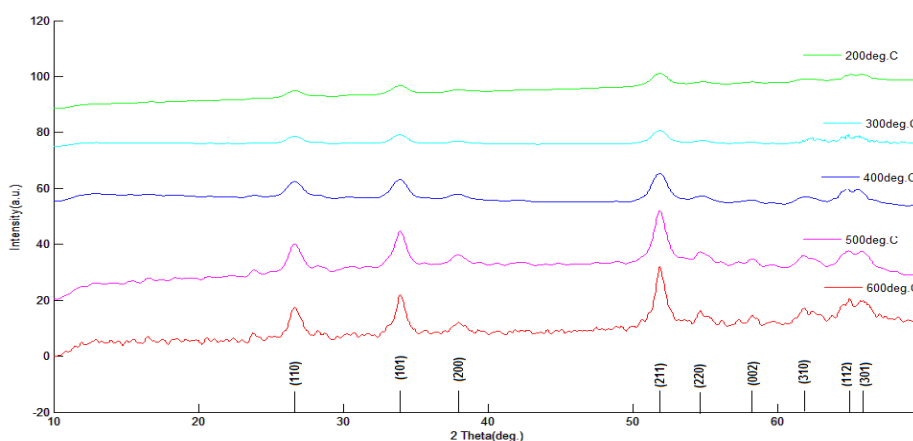


Fig. 2. XRD pattern of the prepared materials at different annealing temperatures.

These reflections shown in Fig. 2 correspond to the standard card (JCPDS card No. 041-1445) that can be indexed to standard pure bulk SnO<sub>2</sub> with a tetragonal rutile structure [14-15]. No impurities were observed. It is seen that as the temperature increases, the prepared SnO<sub>2</sub> nanomaterial becomes more crystalline. It is also observed that with the increase in temperature the diffraction peaks become narrower and exhibits a higher intensity. This can be ascribed to the change in crystal size.

The first major peaks were then used to estimate the SnO<sub>2</sub> crystallite size according to Debye-Sherrer formula [16]:

$$D = \frac{0.9\lambda}{\beta \cos\theta}$$

where  $\lambda$  is the wavelength of the incident X-ray (1.54Å),  $\beta$  is the full width at half maximum intensity of the distinctive peak, and  $\theta$  is the Bragg's angle.

The crystallite sizes were found to be increasing with increasing temperature shown in Table 1. So we can tune the material crystal size by varying the annealing temperature.

**Table 1.** Variation of crystallite size with annealing temperature.

Annealing temperature	Crystallite size(nm)
200	7.08
300	7.55
400	7.57
500	8.2
600	8.98

## 5. Electrical Characterization

A custom made sensor characterization set up as shown in Fig. 3 was used for measurement of the gas sensing properties based on two probe measurement technique. The prepared sensor was placed inside an air tight enclosed test chamber where an arrangement of heating the substrate to an optimum operating temperature was provided. All the five samples were tested to analyze the resistance variation with change in substrate temperature.

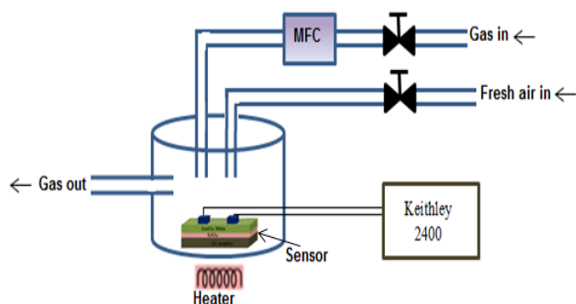


**Fig. 3.** The sensing set up.

Fig. 4 shows the resistances offered by the samples with change in substrate temperature starting from room temperature (27 °C) to 200 °C. An electrometer (Keithley 2400) was used to monitor the sensor resistances. It is observed that the samples annealed at 200 °C and 300 °C showed very little change in resistances even when substrate temperature was increased up to 200 °C from room temperature. Although a change in resistance is seen for the sample annealed at 400 °C, but it become prominent with the sample annealed at 500 °C. For the sample annealed at 600 °C, it is seen that the change in resistance with substrate temperature becomes insignificant. So, from this experiment it can be stated that among the prepared sensors, the one annealed at 500 °C exhibits a good amount of change in resistance with increase in substrate temperature and this characteristics is desirable for a sensing material to work efficiently as a gas sensor.

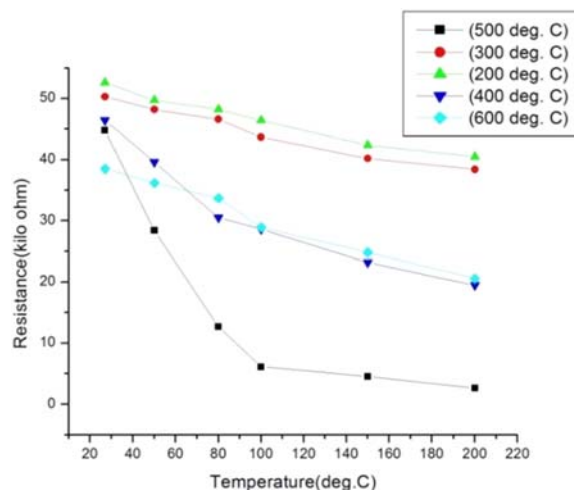


**Fig. 4.** Resistance vs temperature of SnO<sub>2</sub> samples synthesized at different annealing temperatures.

With all the five prepared sensors, I-V characterization was performed (Fig. 5) to see the variation of current in the sensors with application of voltage from 1 V to 10 V.

It is seen that for all the samples, the current increases as the substrate temperature rises on application of a certain voltage. Nevertheless, amongst all the samples, the current vs voltage variation was highest with the sample annealed at 500 °C, which indicates formation of better crystalline structures and grain boundaries on its surface, making it the most suitable sample for gas sensing operation.

## 6. Response on Exposure to Methanol

### 6.1. I-V Characterization

Since the sample annealed at 500 °C exhibited a good amount of change in resistance with temperature variation, 500 °C can be inferred to be the optimum annealing temperature for SnO<sub>2</sub> based sensing material to work as a gas sensor. This sample was then further characterized with gas exposure.

The sensor was experimented with methanol vapour at different operating temperatures and change in current through the sensor with varied applied voltages across the sensor was analyzed (Fig. 6). The operating temperature to the sensor was provided through a heater via a hot-plate as shown in Fig. 3. The flow of methanol vapour to the gas sensor chamber was controlled using a mass flow controller at 0.8slpm (model: Alicat MC-05slpm-D). By keeping the voltage fixed at a certain value, the gas was allowed to enter to the chamber and current readings were recorded. In all the samples, it is seen that after a certain period of time, the current became almost constant on a certain value. Nevertheless, it is found that rise in current level is highest when the operating temperature was maintained at 150 °C.



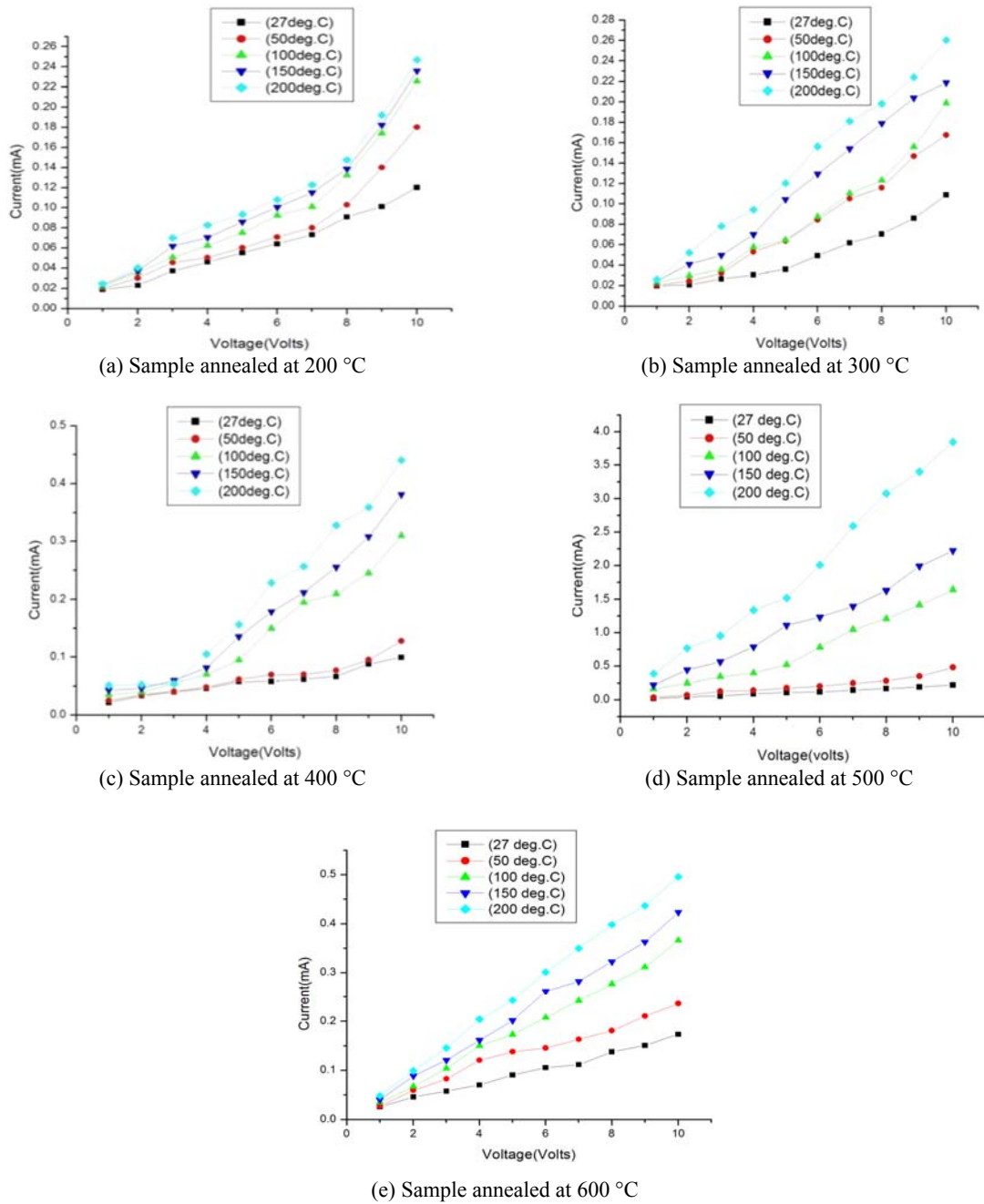


Fig. 5. I-V characterization of the prepared sensors at different operating temperatures without gas exposure.

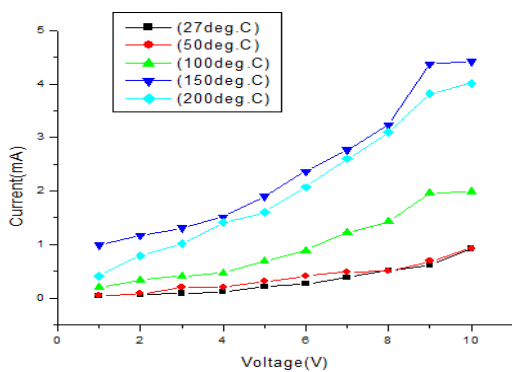
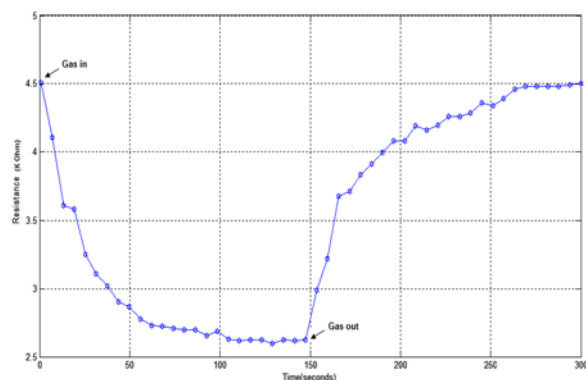


Fig. 6. I-V characteristics of the gas sensor (annealed at 500 °C) at different operating temperatures on exposure to methanol.

## 6.2. Response and Recovery Time

It is seen that the resistance exhibited by the samples decreases with time when exposed to methanol vapour and it increases during the recovery time. It is observed that at operating temperature of 150 °C, the response and recovery time is lower than that of the other operating temperatures. At operating temperature of 150 °C the sensor's response reached a stable value after 105 s upon exposure to methanol. After the sensor was refreshed with fresh air by opening the fresh air inlet and the gas outlet, it was seen that after 122 s, the sensor resistance returned to its baseline value as shown in Fig. 7. Response and recovery time at 150 °C operating temperature was

relatively lower amongst all other operating temperatures. The response and recovery times of the sensor at different operating temperatures is shown in the histogram in Fig. 8.



**Fig. 7.** Gas sensor response at 150 °C operating temperature (Variation of resistance with time).

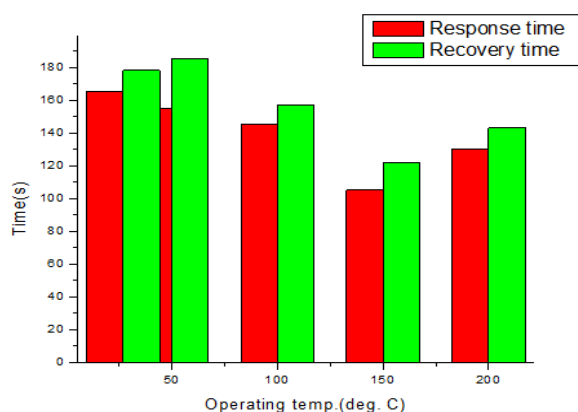


**Fig. 8.** Response and recovery time of the sensor (annealed at 500 °C) at different operating temperatures.

## 7. Conclusions

Fabrication and characterization of SnO<sub>2</sub> based methanol sensor is presented in this paper. SnO<sub>2</sub> was prepared using a low cost wet chemical process and deposited on Si/SiO<sub>2</sub> substrate by spin coating process. The deposited films was then annealed at five different temperatures of 200 °C, 300 °C, 400 °C, 500 °C, 600 °C. XRD based characterization was carried out and it is found that with increase in temperature the crystallite size were increasing. Change in resistance of the sensing film was studied by varying the substrate temperature and it is found that the sample annealed at 500 °C showed prominent change in resistance with increase in substrate temperature as compared to the other samples which makes the sample annealed at 500 °C better choice for gas sensing. So, the sensors annealed at 500 °C was further characterized with exposure to methanol with various operating temperature and it is found that the prepared

sensor works better at an operating temperature of 150 °C. The response and recovery time was also studied. It is seen that the sensor's response reached a stable value after 105 s upon exposure to methanol and it takes 122 s to reach the stable value while flashing the methanol from gas chamber. The response and recovery time of the fabricated sensor was studied for different operating temperature and it is found that at 150 °C response and recovery time is lower as compared to other operating temperatures. In this work it is found that SnO<sub>2</sub> as gas sensor for methanol sensing, 500 °C is optimum temperature for annealing and at 150 °C operating temperature better response is obtained.

## References

- [1]. Amit Gupta, J. K. Srivastava, Anand A. Bhaskar, Pd-doped SnO<sub>2</sub> based Thick Film gas sensor for detection of Methanol, *International Journal of Innovative Research in Engineering & Science*, Vol. 5, Issue 3, May 2014, pp. 49-55.
- [2]. P. Siciliano, Preparation, characterization and applications of thin films for gas sensors prepared by cheap chemical method, *Sensors and Actuators B: Chemical*, Vol. 70, No.1-3, 2000, pp. 153-164.
- [3]. P. Kakoty, M. Bhuyan, SnO<sub>2</sub> based Gas Sensors: Why it is so popular?, in *Proceedings of the IEEE International Conference on Electrical, Computer and Communication Technologies (ICECCT)*, 2015, pp. 1-5.
- [4]. Chen Y. J., *et al.*, Synthesis and ethanol sensing characteristics of single crystalline SnO<sub>2</sub> nanorods, *Applied Physics Letters*, Vol. 87, 2005, pp. 233503-1–233503-3.
- [5]. Maekawa Tomoki, *et al.*, Sensing behavior of CuO-loaded SnO<sub>2</sub> element for H<sub>2</sub>S detection, *Chemistry Letters*, Vol. 25, No. 4, 1991, pp. 575-578.
- [6]. Zhang Jun, *et al.*, Polypyrrole-coated SnO<sub>2</sub> hollow spheres and their application for ammonia sensor, *The Journal of Physical Chemistry C*, Vol. 113, No. 5, 2009, pp. 1662-1665.
- [7]. Mizuno Noritaka, *et al.*, CO<sub>2</sub>-sensing characteristics of SnO<sub>2</sub> element modified by La<sub>2</sub>O<sub>3</sub>, *Sensors and Actuators B: Chemical*, Vol. 13, No. 1-3, 1993, pp. 473-475.
- [8]. Maiti Amitesh, *et al.*, SnO<sub>2</sub> nanoribbons as NO<sub>2</sub> sensors: insights from first principles calculations, *Nano Letters*, Vol. 3, No. 8, 2003, pp. 1025-1028.
- [9]. J. Gonzalez-Chavarri, C. Hurtado, G. G. Mandayo, E. Castano, Design and fabrication of sensor structures for the measurement of toxic gases, in *Proceedings of the Spanish Conference on Electron Devices (CDE)*, 2013, pp. 107-110.
- [10]. Jayaraman V., *et al.*, A low temperature H<sub>2</sub> sensor based on intermediate hydroxy tin oxide, *Sensors and Actuators B: Chemical*, Vol. 55, No. 2, 1999, pp. 147-153.
- [11]. Zhang Gong, Meilin Liu, Effect of particle size and dopant on properties of SnO<sub>2</sub>-based gas sensors, *Sensors and Actuators B: Chemical*, Vol. 69, 2000, pp. 144-152.
- [12]. Cabot A., Arbiol J., Morante J. R., Weimar U., Barsan N., Göpel W., Analysis of the noble metal catalytic additives introduced by impregnation of as

- obtained SnO<sub>2</sub> sol-gel nanocrystals for gas sensors, *Sensors and Actuators B: Chemical*, Vol. 70, No. 1, 2000, pp. 87-100.
- [13]. Park Sung-Soon, J. D. Mackenzie, Thickness and microstructure effects on alcohol sensing of tin oxide thin films, *Thin Solid Films*, Vol. 274, No. 1-2, 1996, pp. 154-159.
- [14]. M. Aziz, S. Abbas, W. Baharom, Size-controlled synthesis of SnO<sub>2</sub> nanoparticles by sol-gel method, *Materials Letters*, Vol. 91, 2013, pp. 31-34.
- [15]. Y. Li, W. Yin, R. Deng, R. Chen, J. Chen, *et al.*, Realizing a SnO<sub>2</sub>-based ultraviolet light-emitting diode via breaking the dipole-forbidden rule, *NPG Asia Materials*, Vol. 4, Issue 11, 2012, p. e30.
- [16]. I. H. Kadhim, H. A. Hassan, Effects of glycerin volume ratios and annealing temperature on the characteristics of nanocrystalline tin dioxide thin films, *Journal of Materials Science: Materials in Electronics*, Vol. 26, Issue 6, 2015, pp. 1-10.



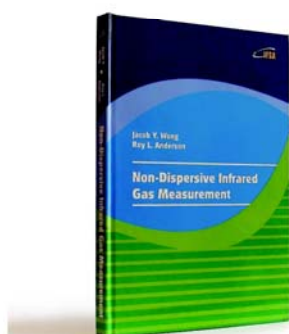
Published by International Frequency Sensor Association (IFSA) Publishing, S. L., 2017 (<http://www.sensorsportal.com>).



International Frequency Sensor Association (IFSA) Publishing

**Jacob Y. Wong, Roy L. Anderson**

## **Non-Dispersive Infrared Gas Measurement**



Formats: printable pdf (Acrobat) and print (hardcover), 120 pages

ISBN: 978-84-615-9732-1,  
e-ISBN: 978-84-615-9512-9

Written by experts in the field, the *Non-Dispersive Infrared Gas Measurement* begins with a brief survey of various gas measurement techniques and continues with fundamental aspects and cutting-edge progress in NDIR gas sensors in their historical development.

- It addresses various fields, including:
- Interactive and non-interactive gas sensors
- Non-dispersive infrared gas sensors' components
- Single- and Double beam designs
- Historical background and today's of NDIR gas measurements

Providing sufficient background information and details, the book *Non-Dispersive Infrared Gas Measurement* is an excellent resource for advanced level undergraduate and graduate students as well as researchers, instrumentation engineers, applied physicists, chemists, material scientists in gas, chemical, biological, and medical sensors to have a comprehensive understanding of the development of non-dispersive infrared gas sensors and the trends for the future investigation.

[http://sensorsportal.com/HTML/BOOKSTORE/NDIR\\_Gas\\_Measurement.htm](http://sensorsportal.com/HTML/BOOKSTORE/NDIR_Gas_Measurement.htm)

**Universal Frequency-to-Digital Converter (UFDC-1 and UFDC-1M-16) in MLF (5 x 5 x 1 mm) package**

**SMALL WORLD - BIG FEATURES**

SWP, Inc., Toronto, Ontario, Canada,  
Tel. +34 696067716, fax: +34 93 4011989, e-mail: [sales@sensorsportal.com](mailto:sales@sensorsportal.com)  
[http://www.sensorsportal.com/HTML/E-SHOP/PRODUCTS\\_4/UFDC\\_1.htm](http://www.sensorsportal.com/HTML/E-SHOP/PRODUCTS_4/UFDC_1.htm)

## Nanocrystalline CdSnO<sub>3</sub> Based Room Temperature Methanol Sensor

**Shanabhau BAGUL, Dhanashri PATIL, Priyanka PATIL  
and \* Lalchand PATIL**

Nanomaterials Research Laboratory, Department of Physics, Pratap College Amalner, Jalgaon, India  
E-mail: [plalchand\\_phy\\_aml@yahoo.co.in](mailto:plalchand_phy_aml@yahoo.co.in)

*Received: 16 March 2017 /Accepted: 17 April 2017 /Published: 30 April 2017*

---

**Abstract:** Synthesis of nanocrystalline CdSnO<sub>3</sub> powder by ultrasonic atomizer assisted wet chemical method is reported in this paper. Synthesized CdSnO<sub>3</sub> powder was characterized by X-Ray Diffraction (XRD), Field Emission Scanning Electron Microscopy (FESEM) and Transmission Electron Microscopy (TEM) to examine phase and microstructure. FESEM and TEM analysis reveals that the CdSnO<sub>3</sub> powder prepared here is porous monodisperse nanocrystalline in nature, with average particle size of approximately 17 nm or smaller. The material is also characterized by UV-Visible and Photoluminescence (PL) spectroscopy. Thick films of synthesized CdSnO<sub>3</sub> powder fired at 850 °C are made by using screen printing method. The films surface is modified by using dipping method. CuCl<sub>2</sub> (0.005M) dipped (for 2 min) thick film shows high response (R= 477) to 100 ppm methanol at room temperature (35 °C). The sensor shows good selectivity and fast response recovery time to methanol. The excellent methanol sensing performance, particularly high response values is observed to be mainly due to porous CdSnO<sub>3</sub> surface.

**Keywords:** Cadmium stannate, Nanocrystalline powder, Thick films, Methanol sensors.

---

### 1. Introduction

In the last 2-3 decades the development of industrial zone uses methanol in many industrial processes, home appliances, as a fuel, and in the production of biodiesel. Volatile organic compounds (VOCs) are easily evaporated at room temperature, which can cause both short-and long-term adverse health effects, such as breathing discomfort, cancers of nervous system, endocrine system and the brain [1-2]. However methanol has strong toxicity and affects on nervous system. Researchers have comparatively more focused on methanol as compare to other volatile organic compounds. Thus it is necessary to develop high response and selectivity methanol gas sensor. Metal oxide semiconductor gas sensors play an important role in environmental monitoring [3].

Metal oxide semiconductor (MOS) gas sensor, as one of the most important conductometric sensors, has attracted dramatic attentions due to their numerous positive features [4-7]. Phase control of perovskite oxides (ABO<sub>3</sub>) with a desired composition is still a challenge owing to their various stoichiometries (e.g. typical formulas of ABO<sub>3</sub>, A<sub>2</sub>BO<sub>4</sub> and AB<sub>2</sub>O<sub>4</sub>) and the associated complex structures [8-9]. In recent years, considerable efforts have been devoted to the synthesis of these complex metal oxides [10]. More effort is needed to reveal their phase evolution and formation mechanism, which is much important for addressing their properties and technological potentials with a specific phase. It is well-known that the gas sensing characteristics are greatly dependent on its morphology and structure, such as porosity, grain size, surface-to-volume ratio, and morphology. The

CdSnO<sub>3</sub> is a perovskite material, which has good thermal and chemical stability due to this it is good candidate for gas sensor. The perovskite and ilmenite cadmium stannate (CdSnO<sub>3</sub>), have been used as alcohol vapor sensing materials [10-13]. In recent years, cadmium stannate (CdSnO<sub>3</sub>) used as electrochemical material [14-15]. CdSnO<sub>3</sub> have shown quite attractive gas sensitivity properties to various gases such as C<sub>2</sub>H<sub>5</sub>OH gas [16], chemical warfare agents Chloro Ethyl Sulphonate (CEES) [17-18].

Modification of pure semiconductor metal oxide is another effective and simple way to improve the gas sensing performance by increasing response, selectivity, stability and decreasing the response-recovery time [19-24]. In recent years, some metal oxides and complex metal oxides have been reported to be used as methanol gas sensors [25-34]. But many of those sensors work at high temperature [26-34].

## 2. Experimental

### 2.1. Synthesis and Characterization of CdSnO<sub>3</sub>

Ultrasonic atomization assisted chemical method was used to synthesize CdSnO<sub>3</sub> nanoparticles. All the chemicals were of analytical grade and used as-received without further purification. In a typical procedure we took 1.1417 g CdCl<sub>2</sub>.H<sub>2</sub>O and 1.7528 g SnCl<sub>4</sub>.5H<sub>2</sub>O were respectively dissolved in 100 ml ethanol (99.9 % purity) to make 0.05 M solution. 0.5 ml hydrochloric acid (HCl) was added drop by drop into the solution of cadmium chloride (0.05 M, 100 ml) called as solution A. SnCl<sub>4</sub> solution (0.05 M, 100 ml) was called as solution B. Solution A was mixed into solution B at room temperature with rigorous stirring for 10 min, forming a mixture of solutions called solution C. 5 ml double distil water was added into the mixture solution C. The mixture solution C was ultrasonicated for 60 minute by using ultrasonic atomizer (2.1 MHz Gapsol 9001 RBI Meylan, France). The solution C got transferred from the transparent form to viscous milky. The viscous solution was dried in hot air oven at 80 °C to get white precipitate powder. The powder was collected and fired at 850 °C for 1 hour in muffle furnace.

### 2.2. Paste Formulation and Preparation of CdSnO<sub>3</sub> Thick Films

The thixotropic paste was formulated by mixing the nanocrystalline CdSnO<sub>3</sub> powder fired at 850 °C with solvent of ethyl cellulose (a temporary binder) in mixture of organic solvents, such as butyl cellulose, butyl carbitol acetate and turpinol, etc. The ratio of inorganic and organic part was kept at 75:25 in formulating the paste. The paste was screen printed on glass substrates in the desired pattern to

obtain the sensors. These sensors were fired at 500 °C for 30 minute to remove the organic binder permanently [35-36]. The films fabricated from as prepared nanocrystalline CdSnO<sub>3</sub> powder were termed as 'unmodified CdSnO<sub>3</sub> films and referred to as S0 sensor.

### 2.3. Preparation of Cu-modified CdSnO<sub>3</sub> Thick Films

The Cu-modified CdSnO<sub>3</sub> thick films were prepared by dipping them into a 0.005 M aqueous solution of Copper chloride CuCl<sub>2</sub>.2H<sub>2</sub>O for different dipping time intervals of 1, 2, 3, 4 and 5 min and referred respectively as S1, S2, S3, S4 and S5 sensors. The films were dried at 80 °C under IR lamp, followed by firing at 500 °C for 30 min in muffle furnace. These surface modified films were called as 'Cu-modified CdSnO<sub>3</sub>' films.

### 2.4. Characterization and Gas Sensor Measurements

The phase and structural study of the powder were determined by powder X-ray diffraction (Bruker D8 Advance) with Cu-Kα1 radiation ( $\lambda = 1.5406 \text{ \AA}$ ) operating at 40 kV, 30 mA at a scanning rate of 2° of 2 $\theta$  per minute over the range 20-80°. The powder was confirmed to be of CdSnO<sub>3</sub>. The morphology and nanostructure of the prepared thick films were investigated by using field emission scanning electron microscopy (FE-SEM: JSM 670 F, JEOL Tokyo Japan) and transmission electron microscope (TEM) (Philips-CM200) with an acceleration voltage of 200 kV. TEM samples were prepared from depositing a drop of diluted suspension of the as-prepared powders in ethanol on a carbon film-coated copper grid. The chemical composition was investigated by using energy dispersive spectrum (EDAX). The thermal properties of the synthesized powder were analyzed by using thermogravimetric-differential scanning calorimetry (TG-DSC) spectrum (STA-6000, Perkin Elmer). The optical properties (band gap) were measured by using ultraviolet-visible spectrophotometer (Shimadzu, Japan) and photoluminescence spectrophotometer (PL, Perkin Elmer). The Fourier transform infrared (FTIR) spectroscopy was used to see the composition of CuO on CdSnO<sub>3</sub> thick films.

The gas sensing performance of the CdSnO<sub>3</sub> thick films were tested in gas sensing system shown in Fig. 1. The prepared CdSnO<sub>3</sub> thick films were cut and made electrical contacts by using purchased silver paste and copper wires. The sensor so fabricated was exposed to various gases mixed with air in chamber. After each exposure to gas, current  $I_a$  and  $I_g$  was measured by using picoammeter, where  $I_a$  and  $I_g$  are current flow through the sensor in air and in the test gas respectively. The sensor was exposed to the atmospheric air by opening the chamber.

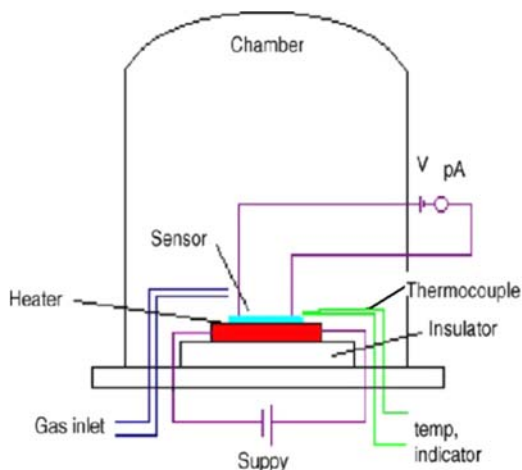


Fig. 1. Block diagram of the gas sensing system.

## 2.5. Sensing Performance of the Sensors

Gas response (S) of sensor is defined as the ratio of the change in conductance of the sensor on exposure to the target gas to the original conductance in air. It is given as:

$$S = \frac{I_g - I_a}{I_a}, \quad (1)$$

where  $I_a$  and  $I_g$  are the current flowing through the sensor resistor in air and in a test gas medium respectively. The response time is a time required by the sensor to reach 90 % of its maximum increase in conductance on exposure of the gas. Recovery time is a time required to get back 90 % of the maximum conductance when the flow of gas is switched off.

## 3. Results and Discussion

### 3.1. Crystalline Structure and Morphology

The crystalline structure of the as-prepared sample was characterized using XRD. As shown in Fig. 2, the XRD spectra of thick films prepared by powder fired at 850 °C for 1 hour. Fig. 2 shows XRD spectrum of (A) pure  $\text{CdSnO}_3$  thick film and (B) 2 min dipped ( $\text{CuCl}_2$ )  $\text{CdSnO}_3$  thick film. All the diffraction peaks of precursor are indexed to the perovskite  $\text{CdSnO}_3$  (JCPDS card No. 01-080-3323) without impurity peak. The crystallite size is estimated using the Scherrer formula,

$$D = \frac{0.89\lambda}{\beta \cos\theta}, \quad (2)$$

where  $\lambda$  is the wavelength of the X-ray radiation ( $\lambda=0.154$  nm for  $\text{CuK}\alpha 1$ ) and  $\beta$  is the peak width at half maximum at  $2\theta$ ,  $\theta$  is the Bragg diffraction angle, D is the mean crystallite size. Average crystallite size of the prepared sample was approximately 15.23 nm. The TEM images, Fig. 3 also reveals that the particles are

of uniform nanospheres with an average diameter of less than 20 nm.

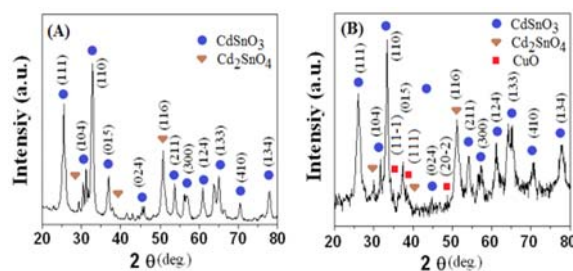


Fig. 2. XRD of thick films of synthesized powder fired at 850 °C (A) Pure, (B) 2 min dipped  $\text{CuCl}_2$ .

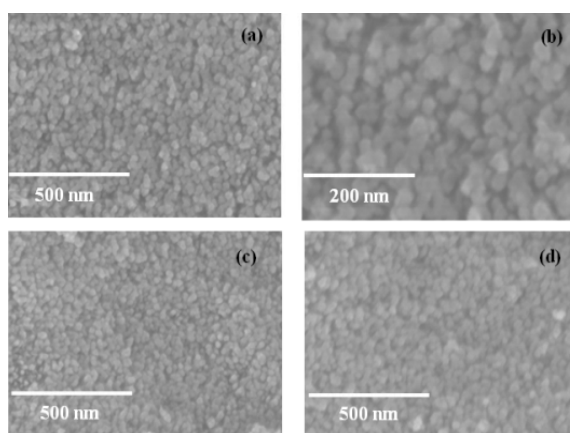
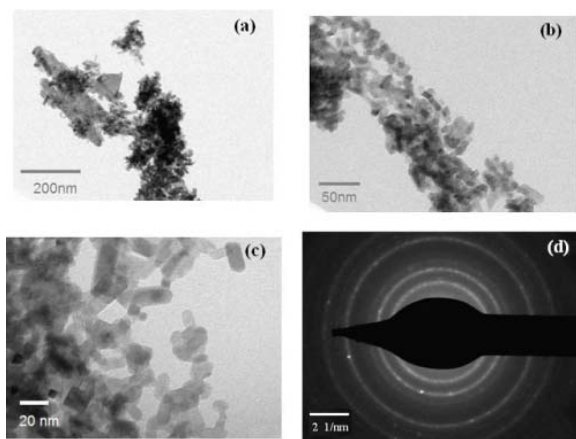


Fig. 3. FESEM images of (a) and (b) pure  $\text{CdSnO}_3$ , (c) 2 min dipped (S2), and (d) 5 min dipped (S5)  $\text{CdSnO}_3$  thick films.

The morphology and microstructure of the as-prepared samples were characterized using FESEM and TEM. The FESEM image of pure  $\text{CdSnO}_3$  sample obtained after calcinations is shown in Fig. 3(a), from which a number of uniform nanospheres with an average diameter of 20 nm could be clearly seen. No other morphologies were detected, indicating a high of these nanospheres. Fig. 3(c) and 3(d) shows the FESEM images of 2 and 5 minute  $\text{CuCl}_2 \cdot 2\text{H}_2\text{O}$  (0.005 M) dipped  $\text{CdSnO}_3$  films respectively. From figures it is seen that the surface get modified with respect to dipping time. The chemical composition of the thick films of pure and surface modified  $\text{CdSnO}_3$  was measured by EDAX and it is observed that the amount of copper increases with respect to dipping time.

To further investigate the morphology of the as prepared particles, the sample was characterized by TEM. Fig. 4(a)-(c) are TEM images of as obtained nanoparticles. Images possessed elongated nanoparticles having average dimensions less than 20 nm. Fig. 4(d) shows the corresponding selected area electron diffraction (SAED) pattern of prepared powder. Electron diffraction rings reveals the polycrystalline structure of the prepared nanoparticles.



**Fig. 4.** (a)-(c) TEM and (d) SAED images of the powder fired at 850 °C.

The band gap of as prepared powder fired at 850°C was measured by using UV-Visible spectrophotometer. Fig. 5 shows the UV-Visible absorption spectrum of synthesized CdSnO<sub>3</sub> powder. From the absorption spectrum, the band gap was found to be 3.1 eV. The measured band gap value is larger than the standard reported value of 2.9 eV. This blue shift may be occurred due to smaller particle size of CdSnO<sub>3</sub>.

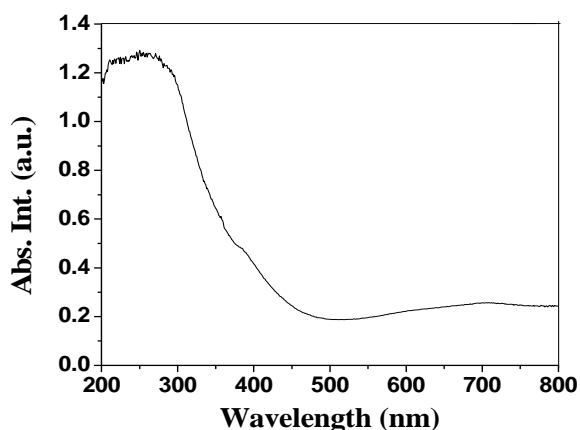


**Fig. 5.** UV-Visible spectrum of synthesized CdSnO<sub>3</sub> powder fired at 850 °C.

The thermogravimetric and differential scanning calorimetry (TG-DSC) analysis were carried out in nitrogen atmosphere, heating from 50 °C to 900 °C at the rate of 10 °C/min (Fig. 6). There is first weight loss observed at 100 °C due to the removal of water. At 550 °C the decomposition of chloroethane is take place. The weight loss from 550 °C to 810 °C is due to removal of chloroethane. There is one exothermic peak occur at 840 °C is due to the crystallization of CdSnO<sub>3</sub>. The balance reaction of as synthesized powder is given in Equation (3).

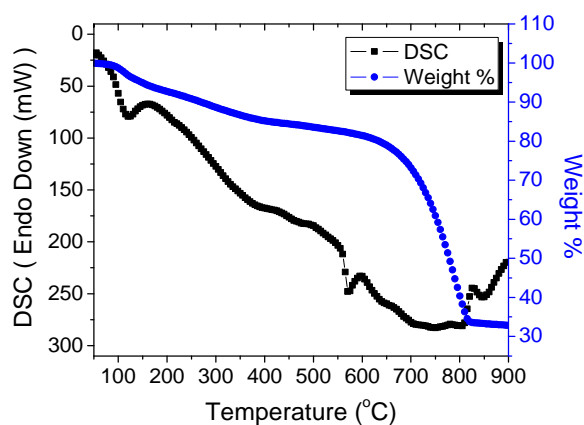
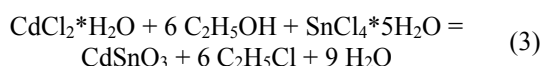


**Fig. 6.** TG-DSC of synthesized powder.

The defect states in CdSnO<sub>3</sub> can be determined by photoluminescence (PL) spectroscopy. The PL spectra of CdSnO<sub>3</sub> nanopowder was measured from 350 to 550 nm at room temperature without any filters used in this study (Fig. 7).

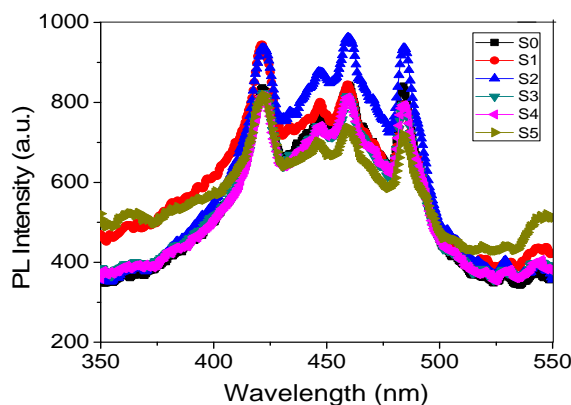


**Fig. 7.** PL emission spectrum of pure and surface modified CdSnO<sub>3</sub> thick films with Exc.300 nm.

Different extrinsic and intrinsic defect centers may be responsible for visible emissions [37-38]. The nanoparticles with large surface to volume ratios have a lot of defects on the surface, which can absorb the O<sub>2</sub><sup>-</sup> and O<sup>-</sup> ions to form the O<sub>2</sub><sup>-</sup>/O<sup>-</sup> surface system. Schoenmakers et al [39] have demonstrated that this O<sub>2</sub><sup>-</sup>/O<sup>-</sup> surface system is the predominant of the electrons in conduction band, which play a key role in the formation of the visible emission centers. Fig. 7 shows emission spectrum of pure and surface modified CdSnO<sub>3</sub> thick films with excitation at 300 nm. It is seen from spectrum that the emission intensity of 2 min dipped film is more than that of pure and other dipped films. It may be due to the more heterocontacts form on the surface of film S2 as compare to the others. The photoluminescence energy associated with localized defect levels can be used to identify specific defects and the amount of photoluminescence can be used to determine their concentration.

The amount of copper oxide on surface of dipped  $\text{CdSnO}_3$  ( $\text{CuCl}_2 \cdot 2\text{H}_2\text{O}$ , 0.005 M) thick films were observed by FTIR spectrum (Fig. 8). From FTIR spectrum it is seen that pure  $\text{CdSnO}_3$  film (S0) do not show CuO peak and other films from S1 to S4 shows CuO peak with increasing absorbance. Peak intensity in infrared spectra shows the concentration of molecules in the sample. From IR spectrum (Fig. 8) it is observed that the amount of CuO increases with dipping time of films in  $\text{CuCl}_2 \cdot 2\text{H}_2\text{O}$  (0.005 M) solution. The surface coverage of  $\text{CdSnO}_3$  films increases with dipping time, at 2 min dipped films there may be more heterocontacts on the surface as compare to other films.

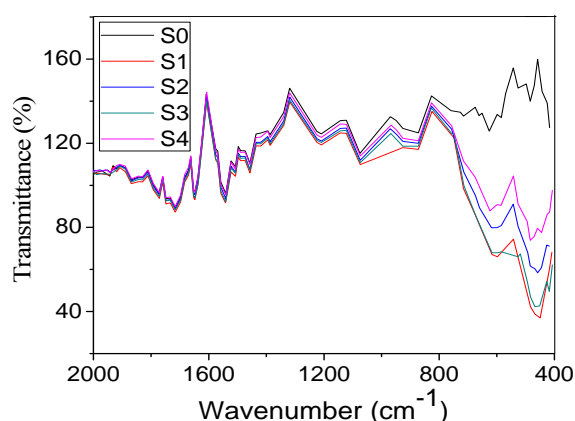


Fig. 8. FTIR spectrum of pure and surface modified  $\text{CdSnO}_3$  thick films.

### 3.2. Gas Sensing Properties

Thick films of synthesized  $\text{CdSnO}_3$  powder were surface modified by using dipping method and made electrical contacts by using purchased silver paste and copper wires. We measured methanol response of pure and surface modified  $\text{CdSnO}_3$  films. Fig. 9(a) shows the variation of response of sensors to methanol. It is observed that the 2 minute dipped film (S2) gives highest response to 100 ppm methanol at room temperature ( $35^\circ\text{C}$ ) as compare to others. At 2 minute dipped film the heterocontacts between CuO and  $\text{CdSnO}_3$  may be larger as compare to the other films. The amount of Cu on surface was measured by EDAX and it shows the amount increases with dipping time. The methanol is more easily dissociated on heterocontacts as compare to pure  $\text{CdSnO}_3$ . It is known the operating temperature play important role in determining gas sensing performance of the sensor. Thus to determine optimal operating temperature to detect methanol the gas sensing measurement were carried out at different operating temperature to 100 ppm methanol. It is observed from experiment that the sensor S2 shows slowly ascending response from room temperature to  $150^\circ\text{C}$  and descends very quickly above  $150^\circ\text{C}$  operating temperature (Fig. 9 (b)).

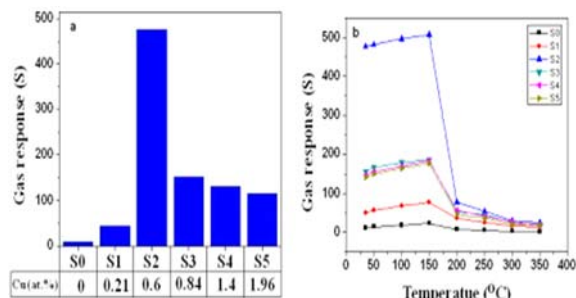


Fig. 9. (a) Response of pure and surface modified sensors to 100 ppm at  $35^\circ\text{C}$ . (b) Response versus operating temperature of the sensor exposing to 100 ppm methanol.

The selectivity of gas sensors is the ability that a sensor can distinguish different kinds of gases. Selectivity is important gas sensing property. We measure the selectivity of sensor to various gases at room temperature. The  $\text{CuCl}_2$  dipped (for 2 minute)  $\text{CdSnO}_3$  thick film (Sensor S2) gives good selectivity to methanol. It can be seen that the sensitivity of sensor S2 to methanol was higher than the sensitivity for other gases at room temperature. Fig. 10(a) shows selectivity of the sensor S2 to various gases.

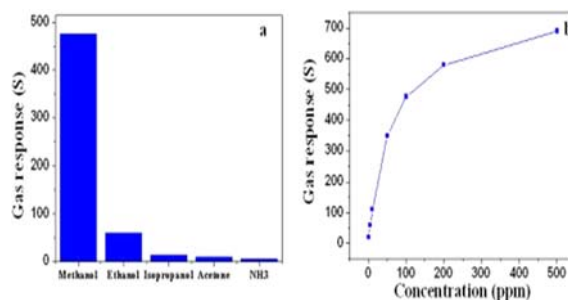
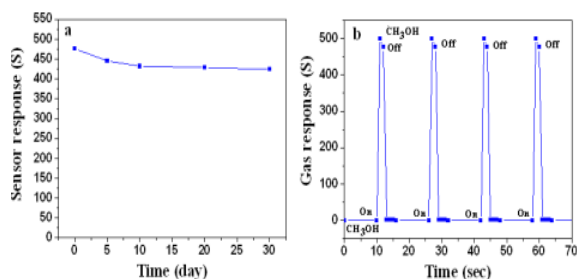


Fig. 10. (a) Selectivity of sensor S2 to 100 ppm vapors at  $35^\circ\text{C}$ , (b) Response versus methanol concentration of sensor S2 at  $35^\circ\text{C}$ .

The sensing performance of the sensor S2 to methanol with different concentration was also performed at room temperature ( $35^\circ\text{C}$ ). Fig. 10(b) shows methanol response of the sensor S2 tested at various methanol concentrations: 5, 10, 20, 50, 100, 200, 500 ppm at room temperature ( $35^\circ\text{C}$ ). From experiments it is observed that the response increases with concentration. At lower concentrations, the response increases fastly and then slowly at higher concentrations of methanol. Stable output of the sensor is important characteristic of sensor for practical application. The experiments to test sensor performance were repeated for few days to study the stability. As seen from experiment (Fig. 11(a)), the long term stability of the sensor has nearly constant response to 100 ppm methanol vapors, which confirmed the good stability of Cu modified  $\text{CdSnO}_3$  thick film (S2).





**Fig. 11.** (a) Stability of sensor S2, and (b) Response recovery curve of sensor S2 to 100 ppm methanol at room temperature (35 °C).

The response and recovery time is an important factor to evaluate the gas sensing properties of the sensor. The response time was defined as the time required for the variation in resistance to reach 90 % of the equilibrium value after a test gas was injected, and the recovery time as the time necessary for the sensor to return to 10 % above the original resistance in air after releasing the test gas. The response recovery time of the sensor S2 to 100 ppm methanol at 35 °C was measured. It is observed that the sensor response in 2 seconds and recover in 5 seconds. Response and recovery times of the sensor were measured to check repeatability and reproducibility (Fig. 11(b)). The sensor was observed to be reproducible. The sensor S2 exhibited fast response (2 s) and quick recovery (5 s). These values are

notable when compared with the response and recovery times reported values by the other researchers (Table 1). The rapid response and recovery of our sensors are due to the porous structure of CdSnO<sub>3</sub> nanospheres, the CuO modified CdSnO<sub>3</sub> nanospheres based thick film sensor (S2) exhibit excellent reproducibility as four reversible cycles of the response curve maintain their initial response value shown in Fig. 8(b). Furthermore, a comparison of this work and some typical metal oxide gas sensors to methanol is presented in Table 1. It should be pointed that the CuO modified CdSnO<sub>3</sub> thick film in present study exhibit higher response and shorter response and recovery time when compared with other metal oxide semiconductor sensors reported in previous works [25-34]. The response of nanocrystalline CdSnO<sub>3</sub> thick film sensor S2 to methanol is much higher than the responses reported in literature, as shown in Table 2.

**Table 1.** Quantitative elemental analysis.

Element (wt %)	Dipping time (min)					
	0 (pure)	1	2	3	4	5
Cd	22.19	20.09	19.30	18.45	19.53	18.70
Sn	21.31	21.18	20.75	20.16	19.74	20.06
O	56.50	56.12	55.68	55.90	54.20	53.12
Cu	-	2.61	4.27	5.49	6.53	7.58

**Table 2.** Comparison of the sensing performances of various metal oxide nanostructure-based sensors towards methanol.

Sensing materials	Operating temperature (°C)	Methanol concentration (ppm)	Sensor response	Response/recovery time (s)	Ref.
CdSnO <sub>3</sub> nanoparticles	Room temperature	100	Ra/Rg = 477	2/4	This work
Co <sub>3</sub> O <sub>4</sub> -intercalated reduced grapheme oxide	Room temperature	800	Rg/Ra = 8.5	240/360	[25]
Ce-doped In <sub>2</sub> O <sub>3</sub> nanospheres	320	100	Ra/Rg = 35.2	14/10	[26]
La <sub>0.8</sub> Pb <sub>0.2</sub> FeO <sub>3</sub> nanoparticles	230	200	Rg/Ra = 50	40/75	[27]
SnO <sub>2</sub> -ZnO composite nanofibers	350	500	Ra/Rg = 65	20/40	[28]
ZnO quantum dots	350	100	Ra/Rg = 90	-	[29]
CuO thin films	350	500	(Rg - Ra)/Ra = 0.12	~380	[30]
Al-doped ZnO thin films	275	500	(Ra - Rg)/Ra = 0.44	~280	[31]
CdS-doped SnO <sub>2</sub> thick films	200	5000	Ra/Rg = 70	40/110	[32]
CuO-modified α-Fe <sub>2</sub> O <sub>3</sub> hybrid hollow spheres	380	100	Ra/Rg = 14	15/30	[33]
polycrystalline Cr <sub>1.8</sub> Ti <sub>0.2</sub> O <sub>3</sub> thick films	300	1.2	[(Rg-Ra)/Ra]×100%=392	23/60	[34]

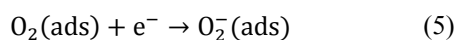
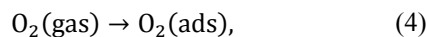
### 3.3. Sensing Mechanism

It was observed that the CdSnO<sub>3</sub> thick films with surface modified by CuO based sensor shows

suddenly decrease in the resistance when the sensor was exposed to reducing gas of CH<sub>3</sub>OH, this indicates that the sensor exhibits n-type conductivity behaviors. The experimental results show that the sensing

properties of CdSnO<sub>3</sub> were greatly enhanced due to incorporating of CuO. Two main reasons account for these results: first, the nanoparticles of CdSnO<sub>3</sub> prepared from ultrasonic atomization offer larger surface accessibility, which will be favorable to adsorption and diffusion of gas molecules, and surface oxidizing reaction of CH<sub>3</sub>OH due to the sensing response of semiconductor metal oxide is surface control type [40]. Second the formation of p-n heterojunction at interface between both oxides is responsible for enhancement of gas response [41]. As we know CdSnO<sub>3</sub> mainly shows n-type conductivity by electrons and CuO displays p-type conductivity by holes. When the CuO were implanted into the surface of CdSnO<sub>3</sub> nanoparticles, the electrons in CdSnO<sub>3</sub> and holes in CuO diffuse in opposite direction due to great gradient of the same carrier concentration. Then, the inner electric field was formed at the CuO/CdSnO<sub>3</sub> interface and the carriers diffuse was finally balanced [42-43]. As a result, the energy band bends in the

depletion layer and the system gets a uniform Fermi level ( $E_f$ ). This is the formation of p-n junction in equilibrium. When the sensor was exposed to air at room temperature (35 °C), the oxygen molecules adsorbed at the adsorption sites on the surface of the material and form chemisorbed oxygen species. The oxygen species most available at room temperature is O<sub>2</sub> [44-45] according to Equation (4) and (5).



A depletion layer will form on the surface of material, leading to the high resistance state of sensing materials. Moreover, the formation of CuO/CdSnO<sub>3</sub> on the surface of CdSnO<sub>3</sub>, p-n heterojunction with a new depletion layer at their interface also make the resistance of sensor to further increase in air, as shown in Fig. 12.

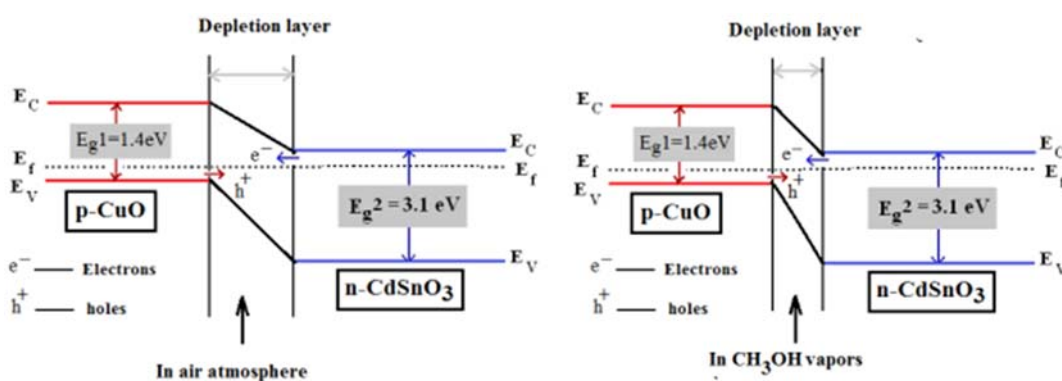
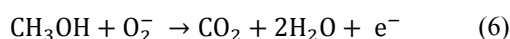


**Fig. 12.** Schematic diagram for the p-type CuO/n-type CdSnO<sub>3</sub> heterojunction based sensor when exposed to CH<sub>3</sub>OH vapors.

However, once the composite was exposed to reducing gas of CH<sub>3</sub>OH, it reacts with the oxygen species adsorbed on the surface of material and release the electrons back to the material as shown in following Equation (6), which decreases the hole concentration in p-type semiconductor of CuO due to electron-hole recombination and reduces the concentration gradient of the same carriers on both sides of p-n junction. Consequently, the depletion layer at the interface becomes thin [46], as shown in Fig. 12. Therefore the resistance of the composite in CH<sub>3</sub>OH is further decreased [47], current increases, that is, the sensor response increases according to define ( $\frac{I_g - I_a}{I_a}$ ) of response.



The sensor S2 gives highest response to CH<sub>3</sub>OH at room temperature (35 °C) as compared to pure and other surface modified CdSnO<sub>3</sub> thick film sensors. This may be due to the large number of heterocontacts are formed between CuO and CdSnO<sub>3</sub> on the surface at 2 minute dipped film in 0.005 M CuCl<sub>2</sub>·2H<sub>2</sub>O solution as compare to other films.

## 4. Conclusions

CdSnO<sub>3</sub> nano particles were synthesized by using ultrasonic atomization assisted chemical method. The morphology and microstructure were analyzed. The CdSnO<sub>3</sub> thick films were cupricated by using dipping method. One of the cupricated sensor (S2) shows highest response to methanol at room temperature as compared to pure and other surface modified CdSnO<sub>3</sub> thick films. The sensor shows fast response and quick recovery. The sensor gives repeatable performance. It may be concluded that cupricated CdSnO<sub>3</sub> thick films may be potential candidate for fabrication of methanol sensor at low cost.

## Acknowledgement

Authors thank Pratap College Amalner for providing every facility required to conduct this research.

## References

- [1]. S. J. Luo, G. Fu, H. Chen, Y. Y. Zhang, Gas sensing properties and complex impedance analysis of La<sub>2</sub>O<sub>3</sub>-added WO<sub>3</sub> nanoparticles to VOC gases, *Materials Chemistry and Physics*, Vol. 109, Issues 2-3, 2008, pp. 541–546.
- [2]. Md. Rajibur Rahaman Khan, B. H. Kang, S. H. Yeom, D. H. Kwon, S. W. Kang, Fiber-optic pulse width modulation sensor for low concentration VOC gas, *Sensors and Actuators B: Chemical*, Vol. 188, 2013, pp. 689–696.
- [3]. S. Yi, S. Q. Tian, D. W. Zeng, K. Xu, X. L. Peng, H. Wang, S. P. Zhang, C. S. Xie, A novel approach to fabricate metal oxide nanowire-like networks based coplanar gas sensors array for enhanced selectivity, *Sensors and Actuators B: Chemical*, Vol. 204, 2014, pp. 351–359.
- [4]. G. Korotcenkov, Gas response control through structural and chemical modification of metal oxide films: state of the art and approaches, *Sensors and Actuators B: Chemical*, Vol. 107, Issue 1, 2005, pp. 209–232.
- [5]. E. Comini, Metal oxide nano-crystals for gas sensing, *Analytica Chimica Acta*, Vol. 568, Issues 1-2, 2006, pp. 28–40.
- [6]. N. Barsan, D. Koziej, U. Weimar, Metal oxide-based gas sensor research: how to ?, *Sensors and Actuators B: Chemical*, Vol. 121, Issue 1, 2007, pp. 18–35.
- [7]. G. Korotcenkov, Metal oxides for solid-state gas sensors: what determines our choice ?, *Materials Science and Engineering B*, Vol. 139, Issue 1, 2007, pp. 1–23.
- [8]. P. V. Vanitha, P. O'Brien, Phase Control in the Synthesis of Magnetic Iron Sulfide Nanocrystals From a Cubane-Type Fe–S Cluster, *Journal of the American Chemical Society*, Vol. 130, Issue 51, 2008, pp. 17256–17257.
- [9]. Yi Zeng, Tong Zhang, Huitao Fan, Geyu Lu, Minghui Kang, Synthesis and gas sensing properties of ZnSnO<sub>3</sub> cubic nanocages and nanoskeletons, *Sensors and Actuators B: Chemical*, Vol. 143, Issue 1, 2009, pp. 449–453.
- [10]. G. Ma, R. Zou, L. Jiang, Z. Zhang, Y. Xue, Li Yu, G. Song, W. Li, J. Hu, Phase-controlled synthesis and gas-sensing properties of zinc stannate (ZnSnO<sub>3</sub> and Zn<sub>2</sub>SnO<sub>4</sub>) faceted solid and hollow microcrystals, *Crys Eng Comm*, Vol. 14, 2012, pp. 2172–2179.
- [11]. C. H. Fan, X. Y. Song, H. Y. Yu, Z. L. Yin, H. Y. Xu, G. X. Cao, D. S. Zheng, S. X. Sun, Shape-controlled synthesis of CaSnO<sub>3</sub> micro crystals via a precursor route, *Materials Letters*, Vol. 61, Issue 7, 2007, pp. 1588–1591.
- [12]. Y. L. Liu, Y. Xing, H. F. Yang, Z. M. Liu, Y. Yang, G. L. Shen, R. Q. Yu, Ethanol gas sensing properties of nano-crystalline cadmium stannate thick films doped with Pt, *Analytica Chimica Acta*, Vol. 527, Issue 1, 2004, pp. 21–26.
- [13]. X. H. Jia, H. Q. Fan, X. D. Lou, J. Q. Xu, Synthesis and gas sensing properties of perovskite CdSnO<sub>3</sub> nanoparticles, *Applied Physics A: Materials Science & Processing*, Vol. 94, Issue 4, 2009, pp. 837–841.
- [14]. Shannon R. D, Gillson J. L, Bouchard R. J, Single crystal synthesis and electrical properties of CdSnO<sub>3</sub>, Cd<sub>2</sub>SnO<sub>4</sub>, In<sub>2</sub>TeO<sub>6</sub>, and CdIn<sub>2</sub>O<sub>4</sub>, *Journal of Physics and Chemistry of Solids*, Vol. 38, Issue 8, 1977, pp. 877–881.
- [15]. Sharma Y., Sharma N., Subba Rao G. V., Chowdari B. V. R., Lithium-storage and cycleability of nano-CdSnO<sub>3</sub> as an anode material for lithium-ion batteries, *Journal Power Sources*, Vol. 192, Issue 2, 2009, pp. 627–635.
- [16]. V. V. Deo, D. M. Patil, L. A. Patil, M. P. Kaushik, Ultrasonically sprayed nanostructured CdSnO<sub>3</sub> thin films for the detection of VOC's, *Sensors and Actuators B: Chemical*, Vol. 196, 2014, pp. 489–494.
- [17]. L. A. Patil, V. V. Deo, M. D. Shinde, A. R. Bari, M. P. Kaushik, Sensing of 2-chloroethyl ethyl sulfide (2-CEES) - a CWA stimulant - using pure and platinum doped nanostructured CdSnO<sub>3</sub> thin films Prepared from ultrasonic spray pyrolysis technique, *Sensors and Actuators B: Chemical*, Vol. 160, Issue 1, 2011, pp. 234–243.
- [18]. L. A. Patil, V. V. Deo, M. D. Shinde, A. R. Bari, D. M. Patil, M. P. Kaushik, Improved 2-CEES sensing performance of spray pyrolyzed Ru-CdSnO<sub>3</sub> nanostructured thin films, *Sensors and Actuators B: Chemical*, Vol. 191, 2014, pp. 130–136.
- [19]. K. Jain, R. P. Pant, S. T. Lakshmikummar, Effect of Ni doping on thick film SnO<sub>2</sub> gas sensor, *Sensors and Actuators B: Chemical*, Vol. 113, Issue 2, 2006, pp. 823–829.
- [20]. Y. Cao, W. Pan, Y. Zong, D. Jia, Preparation and gas-sensing properties of pure and Nd-doped ZnO nanorods by low-heating solid-state chemical reaction, *Sensors and Actuators B: Chemical*, Vol. 138, Issue 2, 2009, pp. 480–484.
- [21]. N. D. Singh, C. Y. Yan, P. S. Lee, Room temperature CO gas sensing using Zn-doped In<sub>2</sub>O<sub>3</sub> single nanowire field effect transistors, *Sensors and Actuators B: Chemical*, Vol. 150, Issue 1, 2010, pp. 19–24.
- [22]. N. Han, X. F. Wu, D. W. Zhang, G. L. Shen, H. D. Liu, Y. F. Chen, CdO activated Sn-doped ZnO for highly sensitive, selective and stable formaldehyde sensor, *Sensors and Actuators B: Chemical*, Vol. 152, Issue 2, 2011, pp. 324–329.
- [23]. P. Song, Q. Wang, Z. X. Yang, Preparation, characterization and acetone sensing properties of Ce-doped SnO<sub>2</sub> hollow spheres, *Sensors and Actuators B: Chemical*, Vol. 173, 2012, pp. 839–846.
- [24]. N. A. N. Azmy, H. Abdullah, N. M. Naim, A. A. Hamid, S. Shaari, W. H. M. W. Mokhtar, Gamma irradiation effect on the structural, morphology and electrical properties of ZnO–CuO doped PVA nanocomposites thin films for Escherichia coli sensor, *Radiation Physics and Chemistry*, Vol. 103, 2014, pp. 108–113.
- [25]. N. Chen, X. G. Li, X. Y. Wang, J. Yu, J. Wang, Z. N. Tang, S. A. Akbar, Enhanced room temperature sensing of Co<sub>3</sub>O<sub>4</sub>-intercalated reduced graphene oxide based gas sensors, *Sensors and Actuators B: Chemical*, Vol. 188, 2013, pp. 902–908.
- [26]. D. Han, P. Song, S. Zhang, H. Zhang, Q. Xu, Q. Wang, Enhanced methanol gas-sensing performance of Ce-doped In<sub>2</sub>O<sub>3</sub> porous nanospheres prepared by hydrothermal method, *Sensors and Actuators B: Chemical*, Vol. 216, 2015, pp. 488–496.
- [27]. C. Doroftei, P. D. Popa, F. Iacomi, Synthesis of nanocrystalline La–Pb–Fe–O perovskite and methanol-sensing characteristics, *Sensors and Actuators B: Chemical*, Vol. 161, Issue 1, 2012, pp. 977–981.
- [28]. W. Tanga, J. Wang, P. Yao, X. Li, Hollow hierarchical SnO<sub>2</sub>-ZnO composite nanofibers with heterostructure based on electrospinning method for detecting

- methanol, *Sensors and Actuators B: Chemical*, Vol. 192, No. 1, 2014, pp. 543–549.
- [29]. A. Forleo, L. Francioso, S. Capone, P. Siciliano, P. Lommens, Z. Hens, Synthesis and gas sensing properties of ZnO quantum dots, *Sensors and Actuators B: Chemical*, Vol. 146, Issue 1, 2010, pp. 111–115.
- [30]. M. Parmar, K. Rajanna, Copper (II) oxide thin film for methanol and ethanol sensing, *International Journal on Smart Sensing and Intelligent Systems*, Vol. 4, Issue 4, 2011, pp. 710–725.
- [31]. P. P. Sahay, R. K. Nath, Al-doped ZnO thin films as methanol sensors, *Sensors and Actuators B: Chemical*, Vol. 134, Issue 2, 2008, pp. 654–659.
- [32]. L. Yadava, R. Verma, R. Dwivedi, Sensing properties of CdS-doped tin oxide thick film gas sensor, *Sensors and Actuators B: Chemical*, Vol. 144, Issue 1, 2010, pp. 37–42.
- [33]. Y. Kang, L. Wang, Y. Wang, H. Zhang, Y. Wang, D. Hong, Y. Qv, S. Wang, Onstruction and enhanced gas sensing performances of CuO-modified  $\alpha$ -Fe<sub>2</sub>O<sub>3</sub> hybrid hollow spheres, *Sensors and Actuators B: Chemical*, Vol. 177, 2013, pp. 570–576.
- [34]. S. Pokhrel, L. Huo, H. Zhao, S. Gao, Sol-gel derived polycrystalline Cr<sub>1.8</sub>Ti<sub>0.2</sub>O<sub>3</sub> thick films for alcohols sensing application, *Sensors and Actuators B: Chemical*, Vol. 120, Issue 2, 2007, pp. 560–567.
- [35]. L. A. Patil, A. R. Bari, M. D. Shinde, V. V. Deo, D. P. Amalnerkar, Synthesis of ZnO nanocrystalline powder from ultrasonic spray pyrolysis technique, characterization and its application in gas sensing, *IEEE Sensors Journal*, Vol. 11, Issue 4, 2011, pp. 939–946.
- [36]. L. A. Patil, P. A. Wani, S. R. Sainkar, A. Mitra, G. J. Phatak, D. P. Amalnerkar, Studies on ‘fritted’ thick films of photoconducting CdS, *Materials Chemistry and Physics*, Vol. 55, Issue 1, 1998, pp. 79–83.
- [37]. M. W. Ahn, K. S. Park, J. H. Heo, J. G. Park, D. W. Kim, K. J. Choi, J. H. Lee, S. H. Hong, Gas sensing properties of defect-controlled ZnO-nanowire gas sensor, *Applied Physics Letters*, Vol. 93, Issue 26, 2008, pp. 263103-1 – 263103-3.
- [38]. N. Han, P. Hu, A. Zuo, D. Zhang, Y. Tian, Y. Chen, Photoluminescence investigation on the gas sensing property of ZnO nanorods prepared by plasma-enhanced CVD method, *Sensors and Actuators B: Chemical*, Vol. 145, Issue 1, 2010, pp. 114–119.
- [39]. G. H. Schoenmakers, D. Vanmaekelbergh, J. J. Kelly, Study of Charge Carrier Dynamics at illuminated ZnO Photoanodes, *J. Phys. Chem.*, Vol. 100, Issue 8, 1996, pp. 3215–3220.
- [40]. D. Ju, H. Xu, Q. Xu, H. Gong, Z. Qiu, J. Guo, *et al.*, High triethylamine-sensing properties of NiO/SnO<sub>2</sub> hollow sphere p–n heterojunction sensors, *Sensors and Actuators B: Chemical*, Vol. 215, 2015, pp. 39–44.
- [41]. D. Ju, H. Xu, Z. Qiu, J. Guo, J. Zhang, B. Cao, Highly sensitive and selectivetriethylamine-sensing properties of nanosheets directly grown on ceramictube by forming NiO/ZnO PN heterojunction, *Sensors and Actuators B: Chemical*, Vol. 200, 2014, pp. 288–296.
- [42]. Y. Chen, L. Yu, D. Feng, M. Zhuo, M. Zhang, E. Zhang, *et al.*, Superiorethanol-sensing properties based on Ni-doped SnO<sub>2</sub> p–n heterojunctionhollow spheres, *Sensors and Actuators B: Chemical*, Vol. 166–167, 2012, pp. 61–67.
- [43]. S. Bai, W. Guo, J. Sun, J. Li, Ye Tian, A. Chen, R. Luo, D. Li, Synthesis of SnO<sub>2</sub>–CuO heterojunction using electrospinning and application in detecting of CO, *Sensors and Actuators B: Chemical*, Vol. 226, 2016, pp. 96–103.
- [44]. V. X. Hien, J.-H. Lee, J.-J. Kim, Y.-W. Heo, Structure and NH<sub>3</sub> sensing properties of SnO thin film deposited by RF magnetron sputtering, *Sensors and Actuators B: Chemical*, Vol. 194, 2014, pp. 134–141.
- [45]. N. Blough, R. Zepp, Reactive oxygen species in natural waters, in: C. Foote, J. Valentine, A. Greenberg, J. Liebman (Eds.), *Active Oxygen in Chemistry*, Springer, Netherlands, 1995, pp. 280–333.
- [46]. A. T. Mane, S. T. Navale, S. Sen, D. K. Aswal, S. K. Gupta, V. B. Patil, Nitrogen dioxide (NO<sub>2</sub>) sensing performance of p-polypyrrole/n-tungsten oxide hybridnanocomposites at room temperature, *Organic Electronics*, Vol. 16, 2015, pp. 195–204.
- [47]. S. Bai, S. Chen, Y. Zhao, T. Guo, R. Luo, D. Li, *et al.*, Gas sensing properties of Cd-doped ZnO nanofibers synthesized by the electrospinning method, *J. of Materials Chemistry A*, Vol. 2, Issue 2, 2014, pp. 16697–16706.



## Synthesis of Nanocrystalline CdSnO<sub>3</sub> Powder on Large Scale by Simple Wet-chemical Route and CdSnO<sub>3</sub> Thick Film Based Sensors for NO<sub>2</sub> Sensing

<sup>1</sup>Shanabhau BAGUL, Dhanashri PATIL, Priyanka PATIL  
and \* Lalchand PATIL

Nanomaterials Research Laboratory, Department of Physics, Pratap College Amalner,  
Jalgaon, India. Pin-425401

<sup>1</sup>Tel.: +91-2587-223103, fax: 223101

<sup>1</sup>E mail: [plalchand\\_phy\\_aml@yahoo.co.in](mailto:plalchand_phy_aml@yahoo.co.in)

*Received: 18 March 2017 /Accepted: 20 April 2017 /Published: 30 April 2017*

---

**Abstract:** Nanocrystalline CdSnO<sub>3</sub> powder was synthesized by cost effective simple wet-chemical route. The technique was found to be useful for large scale production of nanocrystalline CdSnO<sub>3</sub> powder. The prepared CdSnO<sub>3</sub> powder was fired at 600 °C. Structural, microstructural, optical and thermal studies of the powder were carried out. The CdSnO<sub>3</sub> powder was associated with nanocubes with average side length of about 100 nm. Thick films of CdSnO<sub>3</sub> powder were prepared by screen printing method and fired at 500 °C to remove organic part adhesive material. Thick film based sensors showed high response and selectivity to NO<sub>2</sub> gas. The excellent NO<sub>2</sub> response may be due to porous structure and nanocrystalline nature of CdSnO<sub>3</sub> powder.

**Keywords:** Cadmium stannate, Wet-chemical, Nanocrystalline powder, Thick films, NO<sub>2</sub> sensors.

---

### 1. Introduction

NO<sub>2</sub> released from industries and from vehicles increase air pollution which may cause fatal problems not only to human beings but also to animals and plants. The detection of NO<sub>2</sub> is important for monitoring environmental pollution [1, 2]. Especially, nitrogen oxide NO<sub>2</sub> or NO is toxic. It is a main source of acid rain and photochemical smog [3, 4]. NO<sub>2</sub> or NO reacts with ammonia, moisture, and other compounds to form small particles. These small particles enter into sensitive parts of the lungs, may cause respiratory disease and may aggravate existing heart disease. Also NO gas is very easily oxidized into NO<sub>2</sub> gas in air. It is therefore necessary to develop NO<sub>2</sub> gas sensors with high sensitivity and excellent selectivity.

Perovskite oxides (ABO<sub>3</sub>) have attracted attention for their potential use as the gas sensors. CdSnO<sub>3</sub>

belongs to a perovskite structure. It needs cost effective and simplest technique to prepare ultrafine nanostructured CdSnO<sub>3</sub> at reduced the calcination temperature, sintering temperature and sintering time and having porous nature. In recent years, cadmium stannate (CdSnO<sub>3</sub>) had been used as electrochemical material [5, 6]. It was also used for sensing of various gases such as C<sub>2</sub>H<sub>5</sub>OH gas [7], Cl<sub>2</sub> [8], CEES [9].

The article reports simple wet chemical method- the simplest and cheapest way of synthesizing nanocrystalline CdSnO<sub>3</sub> powder on large scale. The preparative conditions of the powder were optimized so as to obtain nanocrystalline CdSnO<sub>3</sub> powder. The powder was studied for its structure, microstructure, optical and thermal properties. Thick films of CdSnO<sub>3</sub> powder were prepared by screen printing method. The gas sensing properties of CdSnO<sub>3</sub> thick films were investigated.

## 2. Experimental

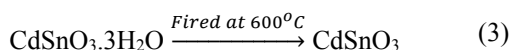
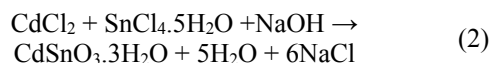
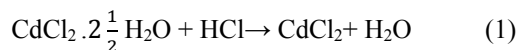
### 2.1. Materials and Method

Synthesis of nanocrystalline CdSnO<sub>3</sub> powder by simple wet chemical route:

The analytical reagent (AR) grade materials including stannic chloride (SnCl<sub>4</sub>.5H<sub>2</sub>O), cadmium dichloride (CdCl<sub>2</sub>. $\frac{1}{2}$ H<sub>2</sub>O), hydrochloric acid (HCl) and sodium hydroxide (NaOH) were dissolved in double distilled water to form transparent solutions. In a typical synthesis of cubic CdSnO<sub>3</sub> powder, 1 ml HCl was added drop by drop into cadmium dichloride (0.25 M, 25 ml) solution in a beaker. The product solution was called as solution A. Solution A was mixed into SnCl<sub>4</sub>.5H<sub>2</sub>O solution (0.25 M, 25 ml) at room temperature with vigorous stirring for 10 min. The solution so obtained was termed as solution B. 50 ml NaOH (2.5 M) solution was taken into the beaker. Solution B was added drop by drop with vigorous magnetic stirring into NaOH solution at room temperature with further vigorous stirring for 10 min. That final solution was kept into the constant temperature heating bath at 90 °C for 3 hours without disturbance. The precipitate formed was collected and washed 3-4 times using double distilled water and ethanol. The resulted product was filtered and dried in hot air oven at 80 °C for 10 hours. The dried powder was fired at 600 °C for 1 hour in muffle furnace.

Formation mechanism of nanocrystalline CdSnO<sub>3</sub>:

Formation of CdSnO<sub>3</sub> may be represented by following equations:



The yellowish CdSnO<sub>3</sub> powder so obtained was further studied using various characterization techniques.

### 2.2. Characterization and Gas Sensor Measurements

The phase and structural study of the powder were determined by powder X-ray diffraction (Bruker D8 Advance) with Cu-K $\alpha$ 1 radiation ( $\lambda = 1.5406 \text{ \AA}$ ) operating at 40kV, 30 mA over the 2 $\theta$  range of 20-80°. The powder was confirmed to be of CdSnO<sub>3</sub>. The morphology of the obtained powder was investigated by using field emission scanning electron microscopy (FE-SEM: JSM 670 F, JEOL Tokyo Japan). The chemical composition was investigated by using energy dispersive spectrum (EDAX). Thermal stability was observed by using thermogravimetric analysis (TGDTA: Perkin Elmer, STA-6000). The optical properties (band gap) were measured by using

ultraviolet-visible spectrophotometry (UV-Visible spectrophotometer: Shimadzu, Japan) and photoluminescence spectrophotometer (Perkin Elmer). Details of thick films preparation procedure and block diagram of indigenous gas sensing system have been explained in our previous publications [9, 10]. Thick film based sensors were exposed to various gases and their response ( $R = \frac{R_g}{R_a}$  where  $R_a$  and  $R_g$  are resistance of the sensor in air and in the test gas respectively), selectivity and transient response (response or recovery time was estimated as the time taken from the sensor output to reach 90% of its saturation after applying or switching off the gas in a step function) were measured at various operating temperatures.

## 3. Results and Discussion

### 3.1. Crystalline Structure of CdSnO<sub>3</sub> Powder

Fig. 1 shows XRD spectrum of the unfired and fired powder. Fig. 1 (a) matches with the standard spectrum of CdSnO<sub>3</sub>.3H<sub>2</sub>O. There are peaks of relatively higher intensities in XRD pattern of fired CdSnO<sub>3</sub> powder as compared to the corresponding peaks in unfired CdSnO<sub>3</sub> powder. It may be due to larger crystallites associated with fired powder (at 600 °C). All the diffraction peaks in fig. 1(b) are consistent with the standard values of the Rhomb-centered CdSnO<sub>3</sub> phase (JCPDS 34-0758).

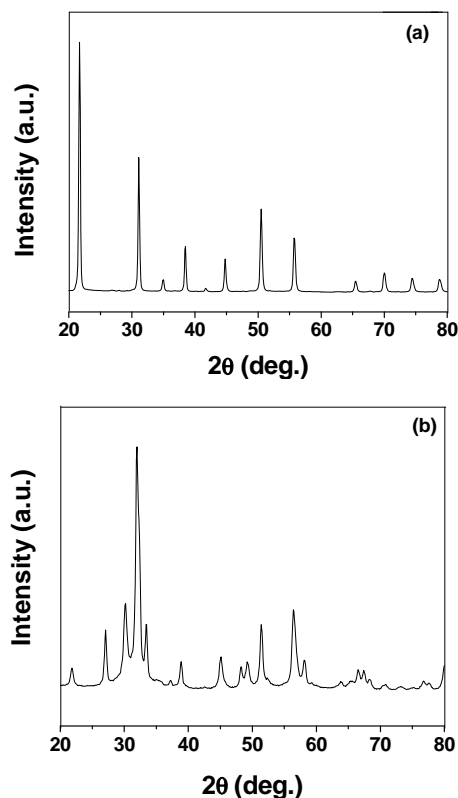


Fig. 1. XRD patterns of: (a) unfired CdSnO<sub>3</sub> and (b) fired CdSnO<sub>3</sub> powder at 600 °C.

### 3.2. Morphology of CdSnO<sub>3</sub> Powder

Particle Morphology of CdSnO<sub>3</sub> powder is represented by FESEM images in Fig. 2 (a)-(d). Quantitative elemental analysis of powder is represented by EDS spectrum in Fig. 2 (e).

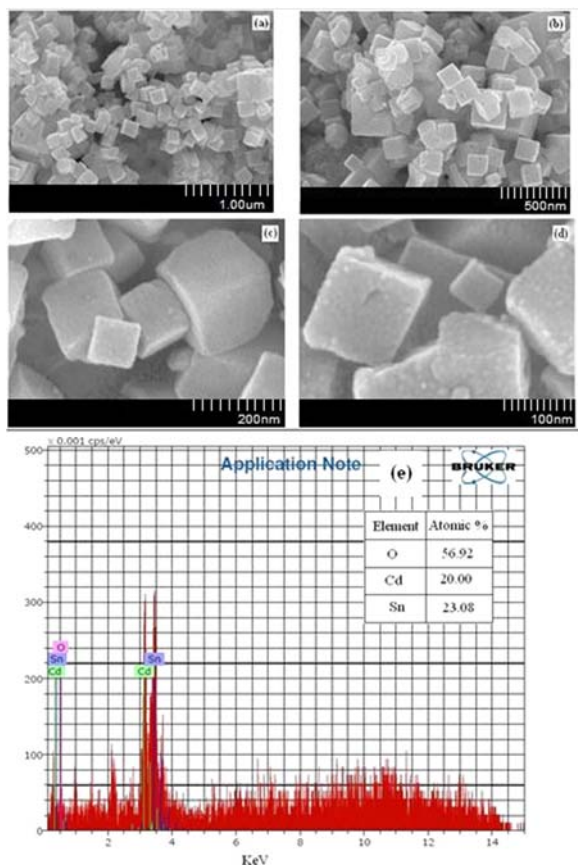


Fig. 2. (a)-(d) FESEM images and (e) EDS spectrum of CdSnO<sub>3</sub> powder fired at 600 °C.

It is clear from Fig. 2(a) that the powder is nanocrystalline and made up of nanocubes. The nanocubes have fairly sharp corners and smooth surfaces. The cubes were observed to be porous in nature (Fig. 2 (d)). The average crystallite size was calculated using Scherrer's equation and was observed to be 100 nm. Energy Dispersive Spectrum (Fig. 2 (e)) revealed that the atomic percentage of Cd, Sn and O was observed to be 20, 23 and 57 respectively. The observed atomic percentage of Cd, Sn and O is nearly matching with the stoichiometric atomic percentage of 20, 20 and 60. Therefore, the CdSnO<sub>3</sub> powder was observed to be nearly stoichiometric in nature.

### 3.3. Thermal Stability of CdSnO<sub>3</sub> Powder

Thermal stability is important property of the materials to be used to fabricate the sensors. Thermogravimetric analysis (TGA) of CdSnO<sub>3</sub> powder was carried out to test the thermal stability. TGA curve

of CdSnO<sub>3</sub> is represented in Fig. 3. In the process of thermal treatment, the weight loss of 0.91 % was observed in the range between 50 to 800 °C. Negligibly small weight loss clearly indicates that the CdSnO<sub>3</sub> powder is thermally stable and suitable to fabricate the gas sensors.

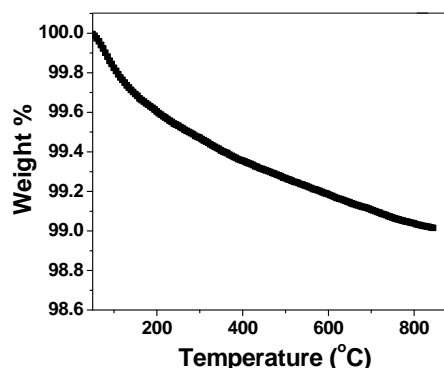


Fig. 3. TGA curve of CdSnO<sub>3</sub>.

### 3.4. Optical Property of CdSnO<sub>3</sub> Powder and Nanocrystallinity of the Powder Particles

The band gap energy of CdSnO<sub>3</sub> powder was determined using UV-Visible absorption spectrum (Fig. 4). The band gap was found to be 3.1 eV. The observed band gap energy (3.1 eV) is larger than reported band gap (2.9 eV). The absorption edge of the spectrum was shifted to lower wavelength side. This is termed as blue shift. The blue shift may be due to nanocrystalline nature of CdSnO<sub>3</sub> powder.

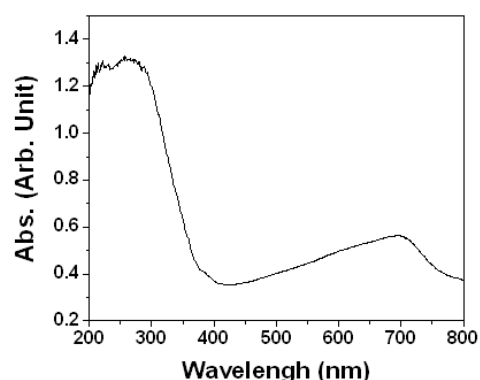


Fig. 4. UV-Visible spectrum of CdSnO<sub>3</sub>.

### 3.5. Photoluminescence (PL) Spectroscopy and Ability of CdSnO<sub>3</sub> chemisorption of Oxidizing Gas

The defect states in CdSnO<sub>3</sub> can be determined by photoluminescence (PL) spectroscopy. Fig. 5 shows PL spectrum for CdSnO<sub>3</sub> sample. The curve shows visible photoluminescence. Visible emissions may be due to different extrinsic and intrinsic defect centers

associated with nanocrystalline powder [11, 12]. The presence of defects would increase chemisorption of oxidizing gases, such as,  $\text{NO}_2$  and oxygen on the surface of sensor. Larger the ability of material to adsorb  $\text{NO}_2$  or oxygen on the surface, larger would be the extraction of surface electrons. If most the surface electrons would be grabbed by gas molecules to adsorbed in terms of ions, very few would be available for conduction and the resistance of the sensor would suddenly increase. This property of the material is helpful in sensing of oxidizing gases.

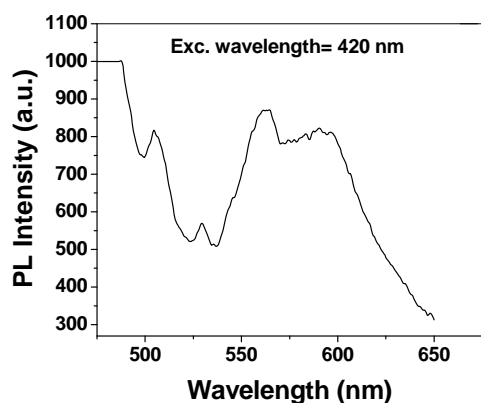


Fig.5 PL spectrum of  $\text{CdSnO}_3$  powder with excitation wavelength 420 nm.

## 4. Gas Sensing Performance of $\text{CdSnO}_3$ Thick Film Based Sensors

### 4.1. $\text{NO}_2$ Gas Response of Sensor

$\text{CdSnO}_3$  thick film based sensor was tested by exposing it to different gases, such as,  $\text{NO}_2$ ,  $\text{Cl}_2$ ,  $\text{H}_2$ ,  $\text{C}_2\text{H}_5\text{OH}$ ,  $\text{NH}_3$  and LPG by varying operating temperature from 40 °C to 350 °C. The sensor showed highest response to  $\text{NO}_2$  at 200 °C. Fig. 6 shows bell shaped variation of  $\text{NO}_2$  response with the operating temperature.

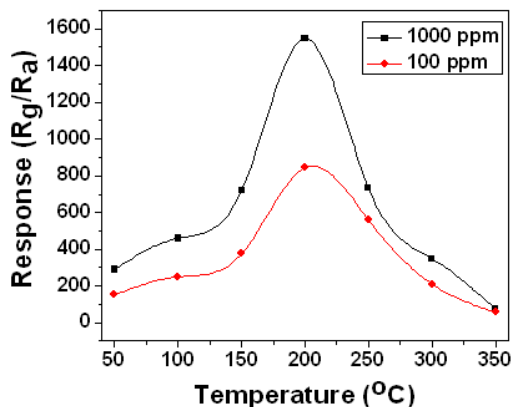


Fig. 6. Variation of  $\text{NO}_2$  response with operating temperature of the sensor.

The sensing performance of the sensor was tested by exposing it to different concentrations of  $\text{NO}_2$ . The variation of  $\text{NO}_2$  response (at operating temperature of 200 °C) with concentration is shown in Fig. 7. The sensor response was observed to be increasing with the concentration of  $\text{NO}_2$ .

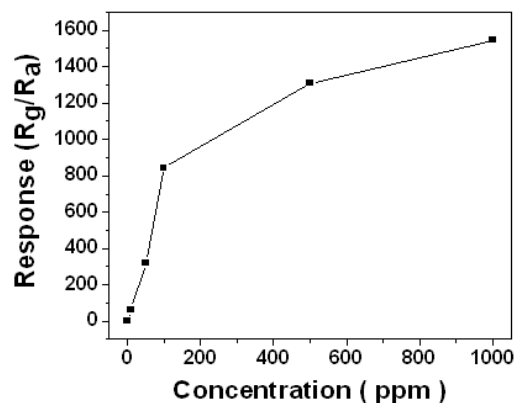


Fig. 7. Variation of sensor response (at 200 °C) with  $\text{NO}_2$  concentration.

### 4.2. Selectivity of Sensor to Various Gases

Sensing performance of the sensor was tested by exposing it to different gases at an optimum operating temperature of 200 °C. The bar diagram in Fig. 8 shows that the response of  $\text{NO}_2$  is largest (more than 1500) as compared to the responses of other gases. The sensor is therefore highly selective to  $\text{NO}_2$  in presence of other gases.

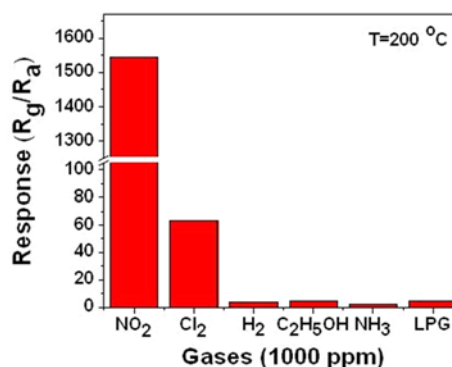


Fig. 8. Selectivity of sensor at 200 °C.

### 4.3. Response and Recovery of the Sensor on Exposure of $\text{NO}_2$

Response-recovery is an important parameter of sensors. Fig. 9 shows the response and recovery of  $\text{CdSnO}_3$  of sensor on exposure of 1000 ppm  $\text{NO}_2$  gas at 200 °C. It is clear from figure that the sensor resistance drastically increases within 2 seconds on exposure of  $\text{NO}_2$  and decreases exponentially when of



supply of NO<sub>2</sub> cuts off and sensor was exposed to air. The response time was observed to be 3 S and recovery time was 140 S.

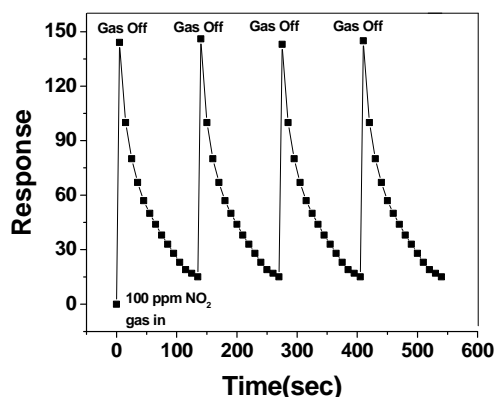


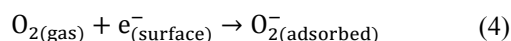
Fig. 9. Response and recovery of CdSnO<sub>3</sub> of sensor on exposure of 1000 ppm NO<sub>2</sub> gas at 200 °C.

## 5. Sensing Mechanism

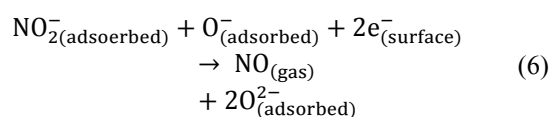
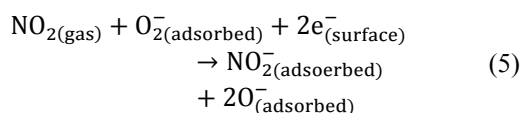
The gas response of nanocrystalline CdSnO<sub>3</sub> powder was measured by change in resistance due to chemical reactions occurring at the surface of the sensor. Nitrogen dioxide can react with metal oxide surface both in the presence and absence of oxygen as given in the equations 4, 5 and 6 [13-15].

At operating temperature of 200 °C, oxygen molecules adsorb on sensor surface as O<sub>2</sub><sup>-</sup> by extracting surface electrons. NO<sub>2</sub> is an oxidizing gas. On exposure on sensor surface, NO<sub>2</sub> would be also adsorbed on oxide surface (at operating temperature of 200 °C) by extracting the surface electrons forming NO<sub>2</sub><sup>-</sup> ions. In presence of NO<sub>2</sub><sup>-</sup> ions, O<sub>2</sub><sup>-</sup> ions would extract more electrons and transformed into O<sup>2-</sup> ions. Due to extraction of the electrons from the sensor surface, the resistance of the sensor suddenly decreases which is the measure NO<sub>2</sub> response. The interaction between the sensor and NO<sub>2</sub> is as follows.

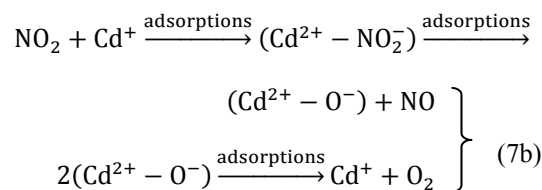
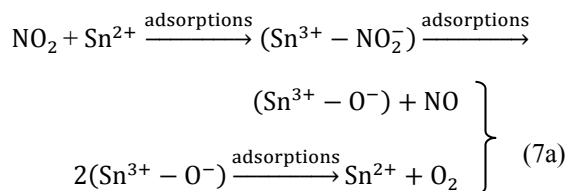
It can be seen that the oxidation of NO<sub>2</sub> leads to the reduction of conduction electrons in the conduction band. At higher temperature, O<sub>2</sub> molecules adsorb on surface of CdSnO<sub>3</sub> as:



NO<sub>2</sub> molecules adsorb as follows:



The adsorption of oxygen and NO<sub>2</sub> molecule on to the vacant site leads to decrease in conductance of the n-type metal oxide [16]. Eq. 7 explains that NO<sub>2</sub> directly adsorbed on the metal sites by electron capture and desorbed as NO [17]. The sensor resistance increased upon exposure to NO<sub>2</sub> gas. The most favorable condition occurs at temperature 200 °C. Due to this the sensor showed high response at 200 °C temperature.



## 6. Conclusions

The prepared CdSnO<sub>3</sub> based thick film sensor shows good response to NO<sub>2</sub> gas at moderately low temperature (200 °C). It can be produced on large scale by low cost, simple chemical route. The CdSnO<sub>3</sub> powder was observed to be cubic in nature with sharp edges. The sharp corners supports to adsorb more NO<sub>2</sub> gas on the surface of CdSnO<sub>3</sub> thick film sensor due to the high electric field intensity at the corners. High sensitivity and selectivity to NO<sub>2</sub> gas may be due to nanocrystalline CdSnO<sub>3</sub> powder.

## Acknowledgement

Authors thank Pratap College Amalner for providing every facility required to conduct this research.


## References

- [1]. N. G. Cho, D. J. Yang, M. J. Jin, H. G. Kim, H. L. Tuller, H-D. Kim, Highly sensitive SnO<sub>2</sub> hollow nanofiber-based NO<sub>2</sub> gas sensors, *Sens. Actuators B*, Vol. 160, Issue 1, 2011, pp. 1468-1472.
- [2]. E. R. Waclawik, Jin Chang, Andrea Ponzoni, Isabella Conciana, Dario Zappa, Elisabetta Comini, Nunzio Motta, Guido Faglia, Giorgio Sberveglieri, Functionalised zinc oxide nanowire gas sensors: Enhanced NO<sub>2</sub> gas sensor response by chemical modification of nanowire surfaces, *Beilstein J Nanotechnology*, Vol. 3, 2012, pp. 368-377.

- [3]. H. Meixner, J. Gerblinger, U. Lampe, M. Fleischer, Thin film gas sensors based on semiconducting metal oxides, *Sens. Actuators B*, Vol. 23, Issues 2-3, 1995, pp. 119-125.
- [4]. A. Gurlo, N. Barsan, M. Ivanovskaya, U. Weimar, W. Gopel,  $\text{In}_2\text{O}_3$  and  $\text{MoO}_3\text{-In}_2\text{O}_3$  thin film semiconductor sensors: interaction with  $\text{NO}_2$  and  $\text{O}_3$ , *Sens. Actuators B*, Vol. 47, Issues 1-3, 1998, pp. 92-99.
- [5]. L. Wang, W. Zhang, C. Wang, D. Wang, Z. Liu, Q. Hao, Y. Wang, K. Tang, Y. Qian, A facile synthesis of highly porous  $\text{CdSnO}_3$  nanoparticles and their enhanced performance in lithium-ion batteries, *J. Mater. Chem. A*, Vol. 2, 2014, pp. 4970-4974.
- [6]. Y. Sharma, N. Sharma, G. V. Subba Rao, B. V. R. Chowdari, Lithium-storage and cycleability of nano  $\text{CdSnO}_3$  as an anode material for lithium-ion batteries, *J. Power Sources*, Vol. 192, Issue 2, 2009, pp. 627-635.
- [7]. Xiaohua Jia, Huiqing Fan, Xiangdong Lou, Jiaqiang Xu, Synthesis and gas sensing properties of perovskite  $\text{CdSnO}_3$  Nanoparticles, *Appl Phys A*, Vol. 94, 2009, pp. 837-841.
- [8]. X. Zhao, Z. Li, X. Lou, M. Li, N Zhang, Room-temperature chlorine gas sensor based on  $\text{CdSnO}_3$  synthesized by hydrothermal process, *J. Advanced Ceramics*, Vol. 2, Issue 1, pp. 31-36.
- [9]. Patil L. A., Deo V. V., Shinde M. D. Shinde, Anil Bari, Dhanashri M. Patil, M. P. Kaushik, Ultrasonically sprayed Nanostructured perovskite type  $\text{CdSnO}_3$  thin films for sensing of CWA simulants, *IEEE Sensors Journal*, Vol. 14, Issue 9, 2014, pp. 3014-3020.
- [10]. G. H. Jain, L. A. Patil, M. S. Wagh, D. R. Patil, S. A. Patil, D. P. Amalnerkar, Surface modified  $\text{BaTiO}_3$  thick film resistor as  $\text{H}_2\text{S}$  gas sensors, *Sens. Actuators B*, Vol. 117, Issue 1, 2006, pp. 159-165.
- [11]. M. W. Ahn, K. S. Park, J. H. Heo, J. G. Park, D. W. Kim, Gas sensing properties of defect controlled  $\text{ZnO}$ -nanowire gas sensor, *Applied Physics Letters*, Vol. 93, 2008, pp. 263103-263107.
- [12]. N. Han, P. Hu, Ahui ZuO, D. Zhang Hu P., Zuo A., D. Zhang, Y. Tian, and Y. Chen, Photoluminescence investigation on the gas sensing property of  $\text{ZnO}$  nanorods prepared by plasma-enhanced, *Sens Actuators B*, Vol. 145, Issue 1, 2010, pp. 114-119.
- [13]. M. B. Rahmani, S. H. Keshmiri, M. Shafiei, K. Latham, W. Wlodarski, J. du Plessis, and K. Kalantar-Zadeh, Transition from *n*- to *p*-Type of Spray Pyrolysis Deposited Cu Doped  $\text{ZnO}$  Thin Films for  $\text{NO}_2$  Sensing, *Sensor Lett*, Vol. 7, 2009, pp. 621-628.
- [14]. O. E. Ruvinskii, N. S. Abramova, V. N. Sirko, Some problems in the theory of adsorption-catalytic stripping voltammetry, *Journal of Analytical Chemistry*, Vol. 58, Issue 7, 2003, pp. 646-647.
- [15]. R. Ferro, J. A. Rodriguez, P. Bertrand, Peculiarities of nitrogen dioxide detection with sprayed undoped and indium-doped zinc oxide thin films, *Thin Solid Films*, Vol. 516, Issue 8, 2008, pp. 2225-2230.
- [16]. S. Kannan, H. Steinebach, L. Reith, F. Solzbacher, Selectivity, stability and repeatability of  $\text{In}_2\text{O}_3$  thin films towards  $\text{NO}_x$  at high temperatures ( $\geq 500^\circ\text{C}$ ), *Sens Actuators B*, Vol. 148, Issue 1, 2010, pp. 126-134.
- [17]. A. Sharma, M. Tomar, V. Gupta,  $\text{SnO}_2$  thin film sensor with enhanced response for  $\text{NO}_2$  gas at lower temperatures, *Sens Actuator B*, Vol. 156, Issue 2, 2011, pp. 743-752.

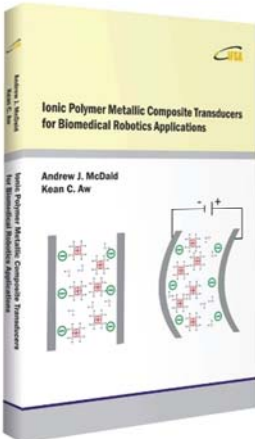


Published by International Frequency Sensor Association (IFSA) Publishing, S. L., 2017  
(<http://www.sensorsportal.com>).



**Andrew J. McDaid, Kean C. Aw**

**Ionic Polymer Metallic Composite Transducers for Biomedical Robotics Applications**



Robotic devices have traditionally been developed for industrial applications for tasks which are repetitive, inhospitable and even unachievable by humans. The natural progression then for future robotic devices is to be intelligent so they can work closely with humans in their own environment. This book is written for leading edge engineers and researchers, working with non-traditional or smart material based actuators, to help them develop such real world biomedical applications. Electrical, mechanical, mechatronics and control systems engineers will all benefit from the different techniques described in this book. The book may also serve as a reference for advanced research focused undergraduate and postgraduate students.

Specifically, this book describes a cluster of research which aims to not only advance the state of art through scientific progress in a specific smart material actuator, namely IPMC, but also serve as a guideline to demonstrate the techniques in which many more issues around developing future smart material actuators can be solved.

Order: <http://www.sensorsportal.com/HTML/BOOKSTORE/IPMC.htm>

Hardcover: ISBN 978-84-616-7669-9  
Printable PDF: ISBN 978-84-616-7670-5

## Phase Method of Invariant Measurement of Active-Inductive Measuring Two-Pole Parameters

**Boris MAMIKONYAN**

National Polytechnical University of Armenia, Gyumri Branch

2 Mher Mkrtchyan, 3103, Gyumri, Armenia

Tel.: +374312-46832, fax: +374312-43528

E-mail: [b\\_mamikonyan@seua.am](mailto:b_mamikonyan@seua.am)

*Received: 25 March 2017 /Accepted: 25 April 2017 /Published: 30 April 2017*

---

**Abstract:** There has been given the solution of the technical problem of separate measurement of parameters of inductance coils and inductive primary converters on alternating current without application of potential-current signals. As a measuring circuit the scheme of voltage divider with active-inductive two-pole is used, and as an output signal there has been used the angle of phase shift between two output voltages of the measuring circuit. For forming the output signal temporal separation of measurement channel is used. The advantages of phase method are mostly due to capacity of using microcontrollers. In the technical solutions under consideration the microcontroller regulates the measuring process and develops the measurement results.

**Keywords:** Inductance coil, Inductance, Active resistance, Measurement two-pole, Phase method.

---

### 1. Introduction

Inductance coils (IC) are widely used in electrical and electronic devices. They are the mandatory and main components of the relay, contactors, transformers, electrical machines; they are used as throttles for redistribution of alternating current along the circuits. While using IC with capacitors, high-quality vibration contours are generated, which are involved in filters and generators of high-frequency vibrations. In most electronic devices besides RC-circuits, RL-circuits are used for integrating or differentiating electrical signals.

Inductive sensors (IS) constitute a large group among devices with IC; these IS are used in various informational-measuring and regulating systems and are responsible for the most important functions. IS are the most available and fail-safe element of drive, machine, automatic line control systems and also measurement systems of physical units. IS are

characterized with relatively simple structure, small sizes, high accuracy and sensibility, comparatively high output voltage value (up to several dozen watts), reduced sensibility to the environment changes and interference and low price. IC, being properly insulated, can successfully operate at around 500 °C [1, 2].

Measurement devices with IS of the plunger type with movable core, in which increment of the coil inductance (or unbalance of the inductance of two coils) is the informative parameter, have got dominant position among electronic devices for linear measurement in the range 0...10 mm due to a number of undeniable advantages over other types of mechanical devices and electrical converters. Numerous manufactory control devices and craft tools as well as laboratory verificatory devices and, among them devices for appraisal and verification of indicators and end measures of length, are equipped with these sensors [3, 4].

IS of eddy-current type, in which the informative parameter is the increment of the coil active resistance, are widely used in control systems of technological processes in food industry, in pulp and paper industry, in brewing, pharmaceuticals, biotechnologies as contactless indicators of object position and for measuring electrical conductivity of liquids [5-7]. In these systems IS have significant advantages over mechanical and conductometric ones; i.e. lack of movable parts, lack of electrodes and, consequently, polarization; they provide exact measurement of the environment or solutions with high level of pollution and tendency to sedimentation, complete galvanic separation of the environment and measurement; high reliability and durability, resistance to temperature and pressure. Over 35 companies in the US are involved in the production of inductive sensors [8].

## 2. Design Considerations

Wide application of IC demands that simple, precise and fail-safe measurers of their parameters, compatible with up-to-date microcontrolling devices for proceeding the information and controlling the measurement process be developed.

The scheme of IC replacement is compiled with respect of the peculiarities of the coil with ferromagnetic core. If winding of the IC contains a great number of coils and there is a potential difference between particular coils and layers of coils, the IC will have some peculiar capacity, which will be switched on parallel to the inductance of the coil. When the current frequency is not very high (up to several hundred kHz), winding capacity can be neglected and the scheme of IC replacement can be presented as consistent connection of active resistance  $R_x$  and inductance  $L_x$ , which makes defining of the IC parameters considerably simpler [9]. For most IC, among them IS, inductance is a beneficial parameter, and active resistance is parasitic one. There are exceptions like eddy-current inductive sensors, induction electricity measurers and others, in which in the air gap of the magnetic circuit a non-magnetic conducting body is placed. In the latter due to the alternating magnetic field, created by the coil, eddy currents are induced, which cause active electric power loss and, consequently, increase of the coil active resistance. In the IS the primary converter (PC) and the measuring circuit (MC) are its constituent parts. Meanwhile MC is to provide invariance of the PC informative parameter measurement result to both destabilizing factors, acting upon PC (e.g. voltage and frequency of the feed generator) and to its non-informative parameters.

Due to the IC ferromagnetic core in which power loss depends on the magnetization reversal rate, active resistance  $R_x$  depends on the coil supply frequency; consequently, IC parameters should be measured by the alternating current of the frequency, on which application of IC is implied. Moreover, with respect of

the nonlinearity of the magnetization curve of the magnetic core, measuring (testing) current should be equal to the operating current of the IC. In addition, since the scheme of IC replacement is in fact complex resistance, MC is to provide separate measurement of the parameters  $R_x$  and  $L_x$ .

## 3. Research Methods

For separate measurement of passive two-element two-pole parameters on alternating current a number of methods and schemes have been developed and they are thoroughly considered in [2, 9, 10]. All the direct methods and the ways of converting parameters of these circuits on the alternating current as an intermediate value have voltage or current. These signals are known to be exposed to the impact of interference and noise. In addition, when linked with the electronic components of the digital technology and computing means they require additional transformations, which make the measurement system complicated.

Comparatively new direction in the field of measurement of passive electrical two-pole parameters is application of the alternating current voltage dividers on the basis of the phase method and the method of measurement channel temporal separation. The development of this direction is due to the general application of microcontrollers in the measuring technology. We have used such technical solution for separate measurement of parameters of the IC replacement consistent scheme [11].

## 4. Electrical Circuit

The essence of the measurer is illustrated by the scheme of Fig. 1, where 1 is the measuring circuit, 2 - two-pole under consideration, 3 - the generator of sinusoidal signals, 4 - electronic switch, 5 - the programmable microcontroller, 6 - the digital reading device (DRD), 7 - the interface converter (UART-USB), 8 - the computer.

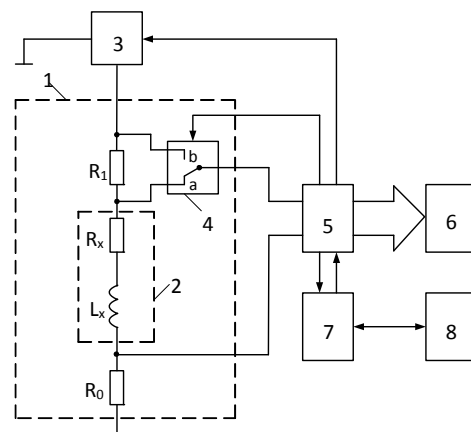


Fig. 1. Simplified principal scheme of the measurer of the inductance coil parameters.

In MC two sample resistors are series connected with the IC: reference resistor  $R_0$  and additional resistor  $R_1$ . The MC, obtained in the result of these compounds, is connected to the generator of the sinusoidal signals as a voltage divider. MC has two output voltages with respect to a common point, which pass onto the microcontroller inlet; voltage  $u_s$  of the common contact of the switch and voltage  $u_0$  of the reference resistor, and in this case the informative signal is the angle  $\varphi$  of phase shift between these voltages. In the process of measurement the microcontroller sets the required frequency  $\omega$  of generator, regulates the switch position and measures the values  $\varphi_1$  and  $\varphi_2$  of the angle  $\varphi$  in the two switch positions. In the switch position  $a$

$$\operatorname{ctg} \varphi_1 = \frac{R_0 + R_x}{\omega L_x} \quad (1)$$

and in the switch position  $b$

$$\operatorname{ctg} \varphi_2 = \frac{R_0 + R_x + R_1}{\omega L_x} \quad (2)$$

When we subtract from the expression (2) the expression (1):  $\operatorname{ctg} \varphi_2 - \operatorname{ctg} \varphi_1 = R_1 / \omega L_x$ , we get

$$L_x = \frac{R_1}{\omega(\operatorname{ctg} \varphi_2 - \operatorname{ctg} \varphi_1)} \quad (3)$$

Now we divide the expression (2) by the expression (1):

$$\frac{\operatorname{ctg} \varphi_2}{\operatorname{ctg} \varphi_1} = 1 + \frac{R_1}{R_0 + R_x}$$

and get

$$R_x = \frac{R_1}{\frac{\operatorname{ctg} \varphi_2}{\operatorname{ctg} \varphi_1} - 1} - R_0. \quad (4)$$

Formulas (3) and (4) provide separate definitions of the IC parameters on the alternating current. It is obvious that it is only required to measure the phase shift angle between two outlet voltages of the measuring circuit. The microcontroller measures the value of the angle  $\varphi$ , computes the parameters  $L_x$  and  $R_x$  according to the formulas (3) and (4) and introduces the measurement results on the digital display; as a display seven segment LED indicators are used. For increasing the reliability of the measurement results in every point the microcontroller performs 10 measurements and gives the average results of these measurements on the indicator.

When it is required, digitized signals of the angles  $\varphi_1$  and  $\varphi_2$  from the microcontroller can be sent on the computer through an interface converter (e. g. AVR 309) and processed and the measurement results can be displayed on the computer monitor.

Since in common case the measurement results  $R_x$  and  $L_x$  also depend on the frequency of the current, which feeds the measuring circuit, the problem of stabilization of this frequency or its control in the measurement process occurs. With respect of this circumstance as a power supply of the measuring circuit a programmable generator of sinusoidal signals AD9833 is used. For each measurement the microcontroller specifies the generator frequency and uses this frequency value while computing the IC parameters; due to it the change of the generator frequency can't have impact on the measurement accuracy. The generator voltage stability is not essential, for in formulas (3) and (4) the generator voltage does not appear.

Thus, the definition accuracy of the IC parameters only depends on the accuracy of measurement of the angle  $\varphi$ . In this device the measurement is performed by the discrete calculation method, therefore the measurement accuracy is considerably higher than when potential-current signals are used.

In these experiments as a measurement object IC with nominal values of parameters  $L_x = 7.2 \text{ mH}$ ,  $R_x \approx 3 \text{ Ohm}$  have been used. A sample resistance box P4831 was connected successively with the IC; the change  $R_x$  was imitated by the change of the resistance in this box. The measuring current is selected equal to  $1,0 \text{ mA}$ , and frequency -  $2 \text{ kHz}$ . Multiple measurements, analysis of results and also theoretical estimate of metrological characteristics of the measurers, according to the scheme on Fig. 1 demonstrated that under production conditions the device can provide measurement of the IC parameters with the limit of permissible relative error, not exceeding  $0.2 \%$ .

It is obvious that in the device according to the scheme of Fig. 1 two-pole 2, which is under the investigation, can also be an ordinary inductive PC. It should be taken into account that PC coils of most modern IS have multilayer windings, a core of ferrite with high magnetic permeability, and that they are intended for feeding by alternating current with frequency  $7-15 \text{ kHz}$ . In case of differential inductive PC we used the MC according to the scheme of Fig. 2, where the sensitive parameters can both be inductance (classical inductive PC) and active resistance (inductive PC of eddy-current type) [12].

In this scheme for the angle of phase shift between voltages  $\dot{U}_s$  and  $\dot{U}_x$  in the initial and second positions of the switch there can be written respectively

$$\operatorname{tg} \varphi_1 = \frac{\omega L_1}{R_1 + R_N}, \quad (5)$$

$$tg \varphi_2 = \frac{\omega L_2}{R_2 + R_N}. \quad (6)$$

If the inductance unbalance ( $\Delta L$ ) is an informative parameter, then  $L_1 = L_0 + \Delta L$ ,  $L_2 = L_0 - \Delta L$ ,  $R_1 = R_2 = R_0$ , where  $R_0$  and  $L_0$  are the initial values of these parameters, which are constant and known (they are indicated in the passport data of PC). For this case from (5) and (6) it follows:

$$tg \varphi_1 - tg \varphi_2 = \frac{\omega(L_1 - L_2)}{R_0 + R_N} = \frac{2\omega\Delta L}{R_0 + R_N},$$

$$tg \varphi_1 + tg \varphi_2 = \frac{\omega(L_1 + L_2)}{R_0 + R_N} = \frac{2\omega L_0}{R_0 + R_N},$$

from which we obtain the formula for defining the informative parameter of PC:

$$\Delta L = L_0 \cdot \frac{tg \varphi_1 - tg \varphi_2}{tg \varphi_1 + tg \varphi_2} = L_0 \cdot \frac{\sin(\varphi_1 - \varphi_2)}{\sin(\varphi_1 + \varphi_2)} \quad (7)$$

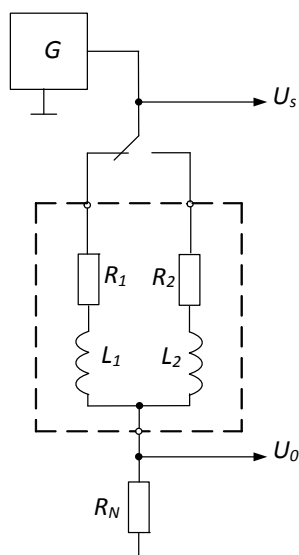


Fig. 2. The scheme of MC for measurement parameters of differential inductive PC.

But if the informative parameter is the unbalance of active resistance, then  $R_1 = R_0 + \Delta R$ ,  $R_2 = R_0 - \Delta R$ ,  $L_1 = L_2 = L_0$ . From (5) and (6) it is defined:

$$ctg \varphi_1 = \frac{R_1 + R_N}{\omega L_0} = \frac{R_0 + \Delta R + R_N}{\omega L_0},$$

$$ctg \varphi_2 = \frac{R_2 + R_N}{\omega L_0} = \frac{R_0 - \Delta R + R_N}{\omega L_0},$$

$$ctg \varphi_1 - ctg \varphi_2 = \frac{2\Delta R}{\omega L_0},$$

$$ctg \varphi_1 + ctg \varphi_2 = \frac{2(R_0 + R_N)}{\omega L_0},$$

$$\frac{ctg \varphi_1 - ctg \varphi_2}{ctg \varphi_1 + ctg \varphi_2} = \frac{\Delta R}{R_0 + R_N},$$

from which we obtain

$$\Delta R = (R_0 + R_N) \cdot \frac{\sin(\varphi_2 - \varphi_1)}{\sin(\varphi_2 + \varphi_1)} \quad (8)$$

## 5. Results

From formulas (7) and (8) it follows that MC, according to the scheme of Fig. 2, permits separate measurements of the differential inductive PC parameters by means of phase method. It is evident that in this case in formulas the generator frequency doesn't appear either, and it implies, that measurement accuracy can be provided, even if the curve shape of the feeding voltage is not purely sinusoidal.

## 6. Conclusion

Analysis of measurers according to the scheme of Figs. 1 and 2, demonstrates that the above-mentioned method of separate measurement of the IC parameters and parameters of inductive PC on alternating current, based on the application of the phase method combined with temporal separation of the measurement channel, is simple in its practical realization and has high accuracy. Its main merit is exception of potential-current signals, conversion and measurement of which are accompanied by unavoidable errors, which are caused by the impact of outer and inner interference and noises, voltages of displacement and shift of operating amplifiers, the non-stability of their amplification factors, the impact of cable communication parameters, etc.

## References

- [1]. Schepetov A. G., The theory, calculation and projecting of measuring devices, *Standartinform*, Moscow, 2008.
- [2]. Fedotov A. V., The theory and calculation of the inductive displacement sensor for the automatic control systems, *OmGTU*, Omsk, 2011.
- [3]. Sorochkin B. M., The automation of measuring and control of details' sizes, *Mashinostroyeniye*, Leningrad, 1990.
- [4]. Sobolev M. P., Etingof M. I., Automatic size control on metal-cutting machines, *Oykumena*, Smolensk, 2005.
- [5]. Klyuev A. S. and others, The projecting of the automated systems of the technological processes: Handbook, *Energoatomizdat*, Moscow, 1990.

- [6]. Buylov G. P. , Doronin V. A. Serebryakov N. P., The automatic and automation of the productions process of the pulp-and-paper productions, *Ecology*, Moscow, 1995.
- [7]. Smirnov V. I., The methods and means of functional diagnostics and control of the technological processes on the base of the electromagnetic sensors, *UIGTU*, Ulyanovsk, 2001.
- [8]. Sensors expo // Sensors. September 1990: [http://www.sensor.ru/articles/299/element\\_1235.html](http://www.sensor.ru/articles/299/element_1235.html)
- [9]. Melentyev V. S., Kostenko E. V., Mironov D. A., The approximate methods of parameters separate determination of two-element and bipolar electric circuits, *Polzunskiy Vestnik*. Issue 3/1, 2011, pp. 47-50.
- [10]. Martyashin A. I., Shakhov E. K., Shlyandin V. M., The converters of electric parameters for control and measurement systems, *Energy*, Moscow, 1976.
- [11]. B. M. Mamikonyan, Kh. B. Mamikonyan, The way of measurement of parameters of the coil of inductance, Patent RA N2930.GO1R 27/00, 2015.
- [12]. B. M. Mamikonyan, Kh. B. Mamikonyan, The way of measurement of informative parameter of the differential inductive transducer, Patent RA N2959.GO1R27/00, 2015.



Published by International Frequency Sensor Association (IFSA) Publishing, S. L., 2017 (<http://www.sensorsportal.com>).

## 10 Top Reasons

to Publish Open Access Books with *IFSA Publishing*



Publish your Open Access Book with IFSA Publishing and get a tablet for free!

More details are available on IFSA Publishing's web site: [http://www.sensorsportal.com/HTML/IFSA\\_Publishing.htm](http://www.sensorsportal.com/HTML/IFSA_Publishing.htm)

Today, many big and small publishers propose open access books publication. How IFSA Publishing open access books differ? Let to be focused on the main benefits:

- **The maximum number of pages is not limited.** Now you should not spend a lot of time and can eliminate additional efforts to put your manuscript in the limited number of page (for example, 350 pages). Create without limitations!
- **Very reasonable fixed price,** which does not dependent on the number of book pages. The publication fee is lower in comparison with other established publishers and is constant regardless of the number of pages.
- **High visibility.** All IFSA Publishing's books are listed on Sensors Web Portal (3,000 visitors per day) a primary Internet sensors related resource, increasing visibility and discoverability for your work. Information about published books also included in IFSA Newsletter (55, 000+ subscribers) and announced in professional LinkedIn Sensors Group (2,600+ members) at no additional charge to ensure the maximum possible distribution. As a result, citation rates of our authors are increased.
- **All book types accepted.** IFSA Publishing accepts complete monographs, edited volumes, proceedings, handbooks, textbooks, technical references and guides.
- **Available in different formats.** The open access eBook is freely available online and accessible to anyone with an internet connection at anytime. In addition to this free electronic version, a print (paper) edition (hardcover, paperback or dust jacket hardcover) in full color is offered for those who still wish to buy a printed book. Various book sizes are possible for print books. The book format is preliminary discussed together with authors. IFSA Publishing is the first publisher in the World who have started publish full-colour, print, sensors related books.
- **Freely available online.** IFSA Publishing's books are freely and immediately available online at Sensors Web Portal's web links upon publication and are clearly labeled as 'Open Access'. They are accessible to anyone worldwide, which ensures distribution to the widest possible audience.
- **Authors retain copyright.** IFSA Publishing's books are published under the Creative Commons Non-Commercial (CC BY-NC) license. It can be reused and redistributed for non-commercial purposes as long as the original author is attributed.
- **High quality standards.** IFSA Publishing's open access books are subject to the same high level peer-review, production and publishing processes followed by traditional IFSA Publishing's books.
- **Authors benefit from our IFSA Membership Program.** IFSA Publishing books charge an open access fee at the beginning of the publication process. Our payment IFSA Members receive a 10 % loyalty discount on this publication fee.
- **Authors free book copies and tablet.** Authors will get free print (paper) book copies (in full colour and one tablet 'Fire' from Amazon (Quad-Core processor, 1.3 GHz, 1 Gb RAM, 7" (17.7 cm), (1024 x 600), Wi-Fi, 8 GB) free of charge

## Chebyshev and Modified Wavelet Algorithm Based Sleep Arousals Detection Using EEG Sensor Database

**Mahalaxmi U. S. B. K. and Ramesh Patnaik M.**

Department of Instrument Technology, Andhra University, India

Tel.: 9490950823

E-mail: aumahalakshmi@gmail.com

*Received: 7 April 2017 /Accepted: 28 April 2017 /Published: 30 April 2017*

---

**Abstract:** Electroencephalographic (EEG) arousals are generally observed in EEG recordings as an awakening response of the human brain. Sleep apnea is a major sleep disorder. The patients, with Severe Sleep Apnea (SAS) suffers from frequent interruptions in their sleep which brings about EEG arousals. In this paper, a new method for Segmentation and Filtering process of EEG sensor database signals for finding sleep arousals using Chebyshev and Modified Wavelet Algorithm is proposed. The Segmentation Algorithm appears as various features extracted from EEG Data's and PSG Recordings. The Chebyshev Equiripple Filter is used in Filtering algorithm and then MSVM [M-Support Vector Machine] was utilized as Classification Tool. Algorithms are performed and different features are extracted and the ROC characteristics are performed. The extracted features are Delta, Gama, Beta, Alpha, Sigma of the EEG signal, EEG Signal Mean, EEG Signal Standard Deviation, EEG Signal Peak Signal to Noise Ratio [PSNR], and EEG Signal Normalization. MSVM tool showing EEG signals results.

**Keywords:** M-wavelet, Chebyshev Equiripple Filter, MW Coefficients, EEG database, MSVM classification tool, CELM, Confusion Matrix.

---

### 1. Introduction

Disorders of sleep apnea syndrome (SAS) have several phases such as obstructive sleep apnea syndrome (OSAS), central sleep apnea syndrome (CSAS) and their combination (mixed apnea). The obstructive sleep apnea (OSA) is most major thing in SAS (Chokroverty [1999]). OSAS is the symptom of upper airway closure in patients during sleep, which leads to serious disorders. OSA causes interruption of sleep period frequently during night, so that the patients cannot able to have a good sleep and always feel daytime sleepiness. This interruption of sleep period by OSA can be seen as immediate responses in electroencephalographic (EEG) records, and the response are known as EEG arousals. Usually PSG test is used in hospitals for diagnosing sleep disorders. The

relationship between appearance of arousal responses and sleep apnea is very important function in the diagnosis of SAS. To interpret the EEG arousals from the durable PSG record which is laborious and time consuming task for medical doctors and technologists. Therefore, the computer assisted system for detecting EEG arousals will be the powerful aid in the clinical scene from the efficiency point of view. The studies on automatic analysis for sleep EEG such as automatic sleep staging have been carried by many researchers in the past. Related studies for the automatic detection of EEG arousals have been proposed (Pillar et al. [2002], Pitson et al. [2006]). Even though the clinical PSG consists of various noise components, characteristics of EEG, these physiological data will vary from individual to individual. Thus, an adequate method usable in the clinical diagnosis aid has not yet



been existed. In this paper, the method for automatic detection of sleeping arousals Chebyshev and Modify wavelet Based EEG signals segmentation using EEG dataset. To separate one band of frequencies from another, Chebyshev filters are used. Different band of frequencies are separated using Chebyshev filters. The initial attribute of Chebyshev filters is their speed, typically which is more than an order of magnitude but faster than the windowed-sinc. This is because they are carried out by recursion method rather than convolution. The design of these filters is mainly based on a mathematical technique called the *z-transform*.

## 2. Sleep Arousal Detection Methodology

### 2.1. Chebyshev Algorithm

Chebyshev Algorithm methods are evolution of conventional QZ AI [1, 2]. These approaches typically involve multiple Fourier transformations of the data, with the goal of contribute more abstract and ultimately more useful representations [3]. These methods are becoming increasingly popular, often outperforming traditional approaches that include handcrafted features for data representation and Integration methods for polynomials process [4, 5].

One of the advance algorithms in efficient Chebyshev algorithm is used to find Eigen values and Eigen function. In the method of Eigen points, the unknown parameters (of polynomial coefficients) in the model are related to the Eigen points of one or more casual Eigen function, and thus, these unknown parameters can be predicted given the Eigen vectors. The Eigen function is mostly predicted from polynomial coefficients. The input signal is  $c[k]$ , previous output signal is  $y[n - 1]$ , the output signal is  $[n]$ , the polynomial coefficients is  $c, d$ .

*Chebyshev Nodes:*

$$X_k = \cos\left(2k - \frac{1}{2n} - \pi\right) \quad (1)$$

$$k = 1, \dots, n$$

*Chebyshev Polynomials:*

$$U_0(x) = 1;$$

$$U_1(x) = 2x;$$

$$U_{n+1}(x) = 2xU_n(x) - U_{n-1}(x) \quad (2)$$

#### 2.1.1. Method of Polynomial Analysis

We assume throughout this paper that, the desired Eigen values are smallest ones. The well-known Chebyshev polynomial to accelerated (fixed dimension) subspace iteration algorithm [5 - 7].

Polynomial Algorithm:

Filter  $x$  by an  $m$  degree Chebyshev polynomial that dampens on  $[a, b]$ .

Input: Vector  $x$ , degree  $m$  and interval and points  $a, b$ .

Output: filtered polynomial  $y$

$$\text{Step 1. } e = \frac{b-a}{2}; \quad (3)$$

$$\text{Step 2. } c = \frac{b+a}{2} \quad (4)$$

$$\text{Step 3. } \sigma = \frac{e}{(a-c)} \quad (5)$$

$$\text{Step 4. } \sigma_1 = \sigma \quad (6)$$

$$\text{Step 5. } y = \frac{(Ax-cx)\sigma_1}{e} \quad (7)$$

$$\text{Step 6. } i = 2:m \quad (8)$$

$$\text{Step 7. } \sigma_{new} = \frac{1}{\left(\frac{2}{\sigma_1} - \sigma\right)} \quad (9)$$

$$\text{Step 8. } x = y \quad (10)$$

$$\text{Step 9. } y = y_{new} \quad (11)$$

$$\text{Step 10. } \sigma = \sigma_{new} \quad (12)$$

#### 2.1.2. Filtering Techniques

$$Ch = \cos * \frac{\pi i}{8 * ch} + \cos * \frac{\pi i}{2 * ch} + \sin \frac{3 * \pi i}{4 + ch} \quad (13)$$

Ch ---channels

#### 2.1.3. Trigonometric Techniques

$$Ch_{trio} = \cos \frac{\pi i}{8 * ch1} + \cos \frac{\pi i}{2 * ch1} + \sin \frac{3 * \pi i}{4 + ch1} \quad (14)$$

#### 2.1.4. Equiripple Techniques

Equal ripples in both the passband & stopband, denotes the signal distortion which happens at the edge of passband due to presence of a large ripple is avoided in Equiripple design whereas the Equiripple design [8, 9] has a large transition band, where the total passband width will be limited.

$$Eq = \cos \left(2 * i - \frac{1}{2} * 7 - \pi\right) \quad (15)$$

## 2.2. Segmentation Process

In this section we have Segmentation process for EEG Data base using M-Wavelet Transform Algorithm Development. The Modules have various parameters, and also two main segment, they are arousals and valance frames. They parameters act as a coefficient matrix from M-wavelet. This algorithm first stage is decomposing the coefficients and then the decomposed elements are reconstructed and then various features are extracted from this module [10, 11].

Wavelet function is

$$\int_{-\infty}^{\infty} \varphi(t) dt = 0 \quad (16)$$

M-Wavelet function is

$$MW_{\varphi}x(a, b) = \frac{1}{\sqrt{a}} \int_{-\infty}^{\infty} x(t) \varphi * \frac{t-b}{a} dt, \quad (17)$$

where  $a$  is the Decomposed data's,  $b$  is the Decomposed vector's

The wavelet coefficients are deals with soft thresholding. The various steps of the M-DWT method are detailed below:

- 1) Apply Modified discrete wavelet transform to the signal;
- 2) Compute the hierarchical correlations of the detailed coefficients between level 1 and level 2 for three different (horizontal, vertical and diagonal) directions;
- 3) Select relevant threshold values based on the achieved hierarchical correlation values.
- 4) Apply the selected threshold values to the coefficients of level 1 for removing of noise, and can obtain the modified detailed coefficients for level 1;
- 5) Apply inverse wavelet transform to the modified wavelet coefficients;
- 6) Repeat steps 1-5 again, leading to obtain a final value.

## 2.3 Features Extraction Process

The Features are Power spectrum, Normalization, Entropy, Mean, Standard Deviation, Variance, Dynamic Range, Relative Power Energy, Logarithmic Relative Power Energy, and Absolute Logarithmic Relative Power Energy.

### 2.3.1 Mean

The probability distribution of random signals  $X$  the mean is equal to sum over every possible signal values.

$$\mu = \sum xP(x), \quad (19)$$

where  $x$  denoted to total number of signals values of EEG.

An analogous formula applies to the case of a 2D EEG Database probability distribution.

### 2.3.2. Power Spectrum

The power spectrum of a signal is the power or more simply energy of the signal at each frequency that contains. It can also be considered as the range or signal of energy or power of the given signal derived from the signals range of frequencies.

$$P = \frac{1}{2T} \int_{-T}^T x(t)^2 dt \quad (20)$$

Above process are stationary process, for instance, may have a finite power but an infinite energy. The

energy is the integral of power, and the stationary signal continues over an infinite time.

The content of signal  $x(t)$ , we can compute the Fourier transform  $\hat{x}(\omega)$ .

The truncated Fourier transform  $\widehat{x}_T(\omega)$ , where the signal is integrated only over a finite interval  $[0, T]$ .

$$x_T(\omega) = \frac{1}{\sqrt{T}} \int_0^T x(t) e^{-i\omega t} dt \quad (21)$$

### 2.3.3. Normalization

The Landolt concludes that forced normalization (FN) is the phenomenon characterized by the fact that, with the occurrence of psychotic states, the electroencephalography become more normal or entirely normal, as compared with previous and subsequent EEG signals.

$$d = P(:) \quad (22)$$

$$N_{(d,dn)} = \frac{d}{\text{sum}(d+1e-12)}, \quad (23)$$

where  $d$  is the normalization of signals. This signal converts into single column.  $N_{(d,dn)}$  is the total number of EEG signals. This represents as based on EEG band's.

### 2.3.4. Entropy

The Anesthetic and arousal detection and analysis based on entropy parameter's, from EEG bands. Entropy used to find to EEG activity from electromyogram.

$$\text{Log} = \log_2(d + 1e - 12) \quad (24)$$

$$\text{Entropy} = \frac{-\text{sum}(d.*\log)}{\log_2(\text{length}(d))} \quad (25)$$

### 2.3.5. Standard Deviation

For continuous EEG signal

$$\sigma = \sqrt{\int_{-\infty}^{\infty} p(x) dx} \quad (26)$$

where  $x$  is the EEG Band data.

For a discrete EEG signal

$$\sigma = \sqrt{\int_{-\infty}^{\infty} p_i x_i} \quad (27)$$

Relative power energy can be given by the following equation:

$$R_p = \frac{\text{norm}(y)^2}{\text{length}(y)} \quad (28)$$

Logarithmic RPE:

$$\log_{rpe} = \log(R_p) \quad (29)$$

Absolute RPE:

$$Abs_{RPE} = abs(RPF) \quad (30)$$

## 2.4. Fusing and CELM Process

### 2.4.1. Fusing Process

$$Features_{(x,y,...,n)} = Concat^{all\ features} \quad (31)$$

### 2.4.2. CELM Process

Step 1.

Present samples  $X_t, C_t$

$$C_{xy} = sum(fea) * l, \quad (32)$$

where x,y are the total samples, l is the dynamic range of signals

Step 2.

Apply compute process by features by Entropy parameters.

Step 3.

Conjugate Process of EEG data's.

Extracting real and complex parameters of EEG data's

Step 4.

Apply FFT Process.

### 2.4.2. Proposed Multi Support Vector Machine (MSVM) Process

The SVM has been studied extensively for classification, regression, and density estimation. Fig. 1 represents the proposed block diagram of SVM. It maps the input patterns into a higher-dimensional-feature space through some nonlinear mapping which is chosen by priority. A linear decision surface is then constructed in this high-dimensional-feature space. Hence the SVM is a linear classifier in the parameter space, where it develops into a nonlinear classifier as a result of nonlinear mapping of the space of the input patterns to the high-dimensional feature space. Training the SVM will be a quadratic-optimization problem. The construction of a hyper plane  $wT x + b = 0$  ( $w$  is the vector of hyper plane coefficients,  $b$  is a bias term) creates the maximum margin between the hyper plane and the nearest point which can be posed as the quadratic-optimization problem. SVM has been shown to provide high-

generalization ability. A proper kernel function is always dependent on the specific data for any problem and till now there is no proper way for how to select a kernel function. In this paper, the selection of the kernel functions was studied experimentally and optimal results were achieved using radial-basis function (RBF) kernel function.

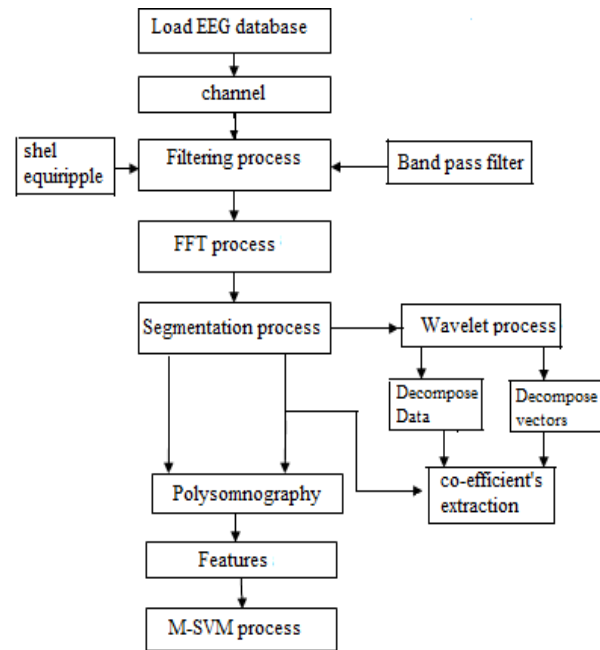


Fig. 1. Proposed Block Diagram.

Generally SVM is a binary classifier, which can be extended by fusing several of its kind into a multiclass classifier. In this paper, we fuse SVM decisions using the ECOC approach, adopted from the digital communication theory. In the ECOC approach, up to  $(2n-1) - 1$  (where  $n$  is the number of classes) SVMs are trained, each of them aimed at separating a different combination of classes. For three classes (A, B, and C) we need three classifiers; one SVM classifies A from B and C, a second SVM classifies B from A and C, and a third SVM classifies C from A and B. The multiclass classifier output code for a pattern is the combination of targets of all separate SVMs. In our example, vectors from classes A, B, and C have codes  $(1,-1,-1)$ ,  $(-1,1,-1)$ , and  $(-1,-1,1)$ , respectively. If each of the separate SVMs classifies the pattern correctly, then the multi class classifier-target code is met and the ECOC approach reports no error for that pattern. However, if one of the SVMs disagrees the pattern, the class selected for this pattern is the one its target code closest in the Hamming distance senses to the actual output code and this may be an erroneous decision.

Algorithm steps:

Step 1:

$$G = length(EEG), \quad (33)$$

where G is the group of MSVM.

Step 2:  
Apply MSVM Training Process

$$MSVM_{(d,g)} = \int_{-\infty}^{\infty} f_{(x,y)} dx \quad (34)$$

where d is the total features data, g is the total number of groups.

Step 3:  
Classification process

$$MSVM_{structs,class} = \int_{-\infty}^{\infty} p_{xyz} dx \quad (34)$$

where x is the kernel function of MSVM, y is the class, z is the MSVM Vector.

**ROC Curve performance:**

The roc curve plotting performance is shown in Fig. 2. This figure represents the MSVM algorithm performance based in Bundle of features.

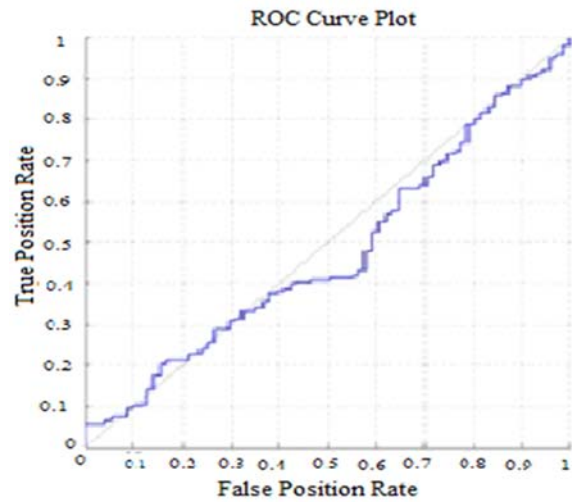
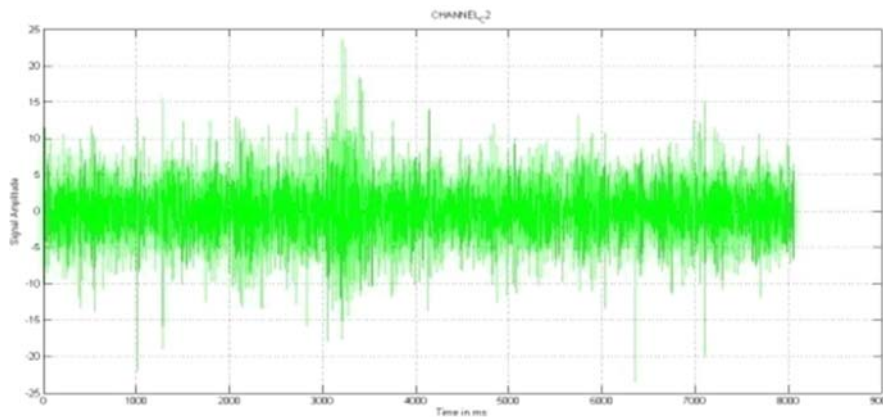


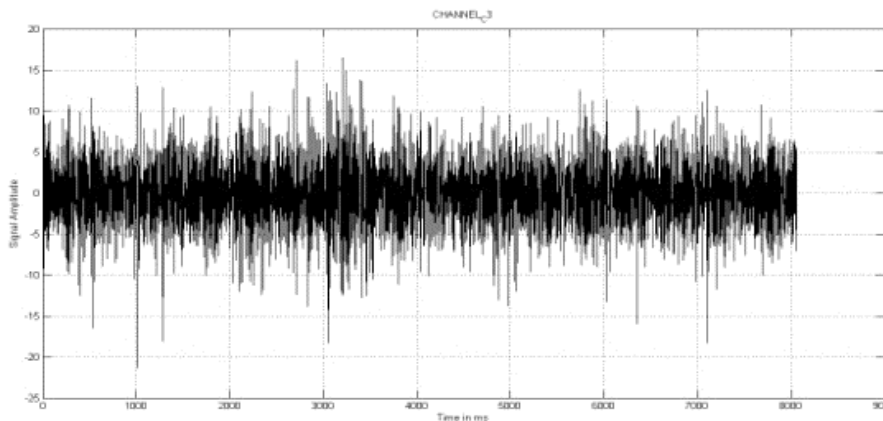
Fig. 2. ROC Characteristics

**3. Experimental Results**

The experimental results are shown in Fig. 3-12.



(a)



(b)

Fig. 3. (a) EEG signal of channel 1, (b) EEG signal of channel 2.

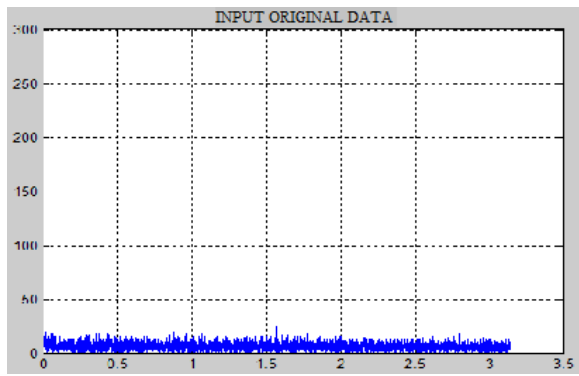


Fig. 4. Input original data.

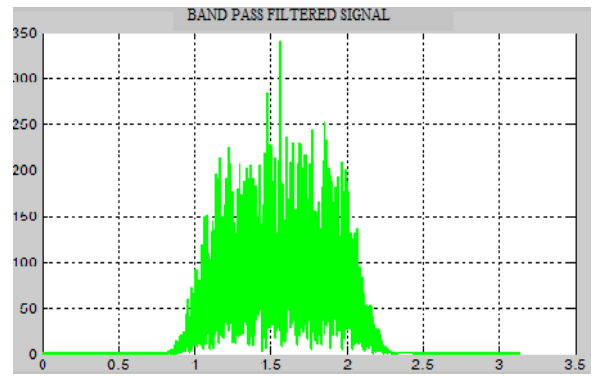


Fig. 5. Band pass filtered signal.

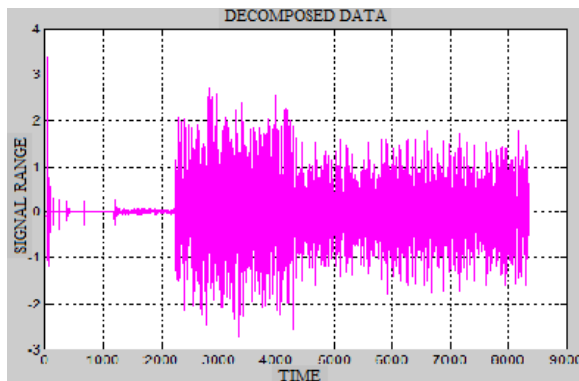


Fig. 6. Decomposed signal.

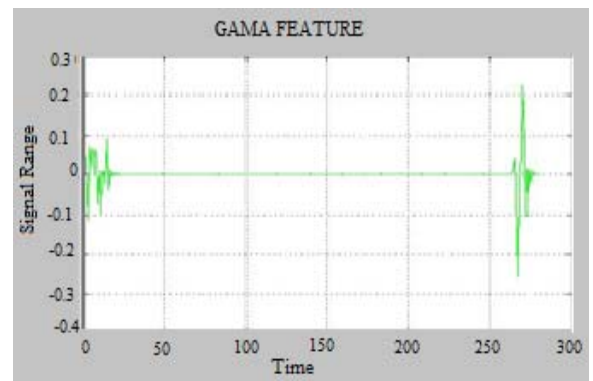


Fig. 7. Gamma Feature.

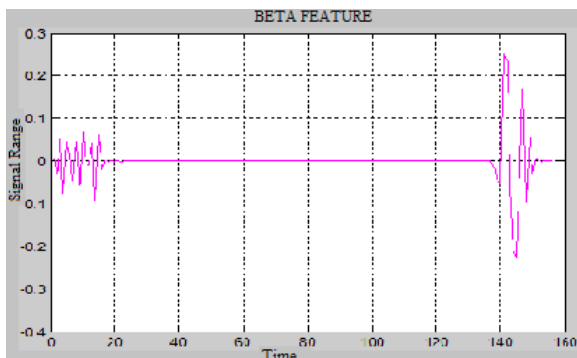


Fig. 8. Beta Feature.

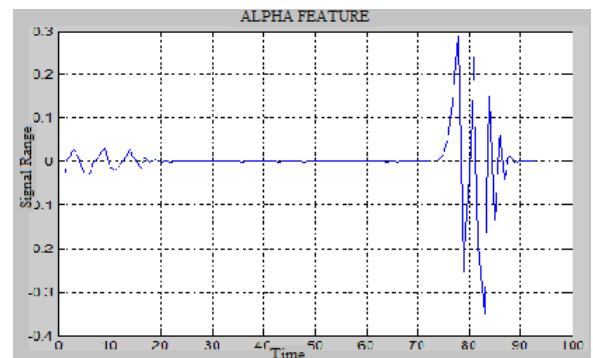


Fig. 9. Alpha Feature.

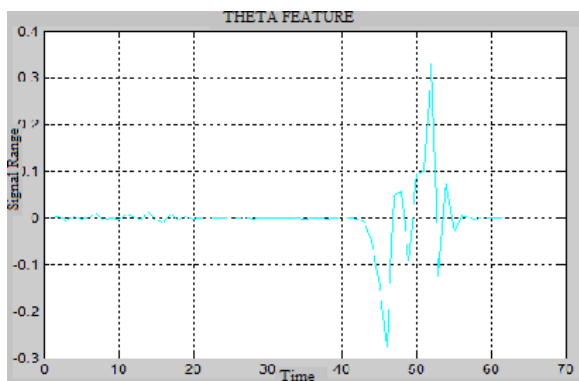


Fig. 10. Theta Feature.

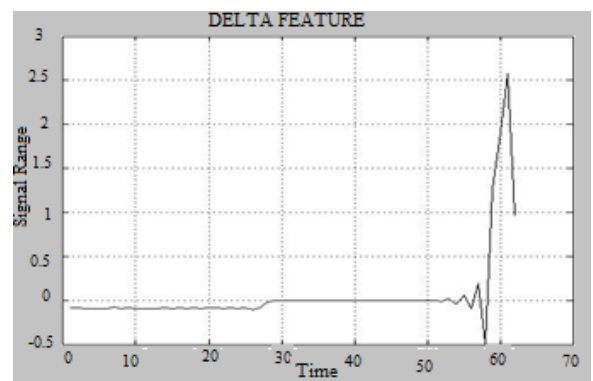


Fig. 11. Delta Feature.

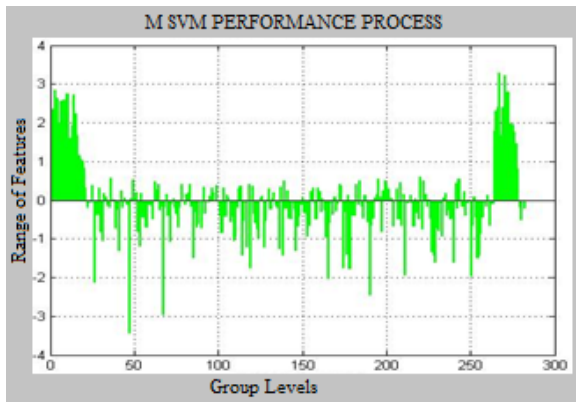


Fig. 12. MSVM Performance.

#### 4. Confusion Matrix Performance

The confusion matrix describes the performance of MSVM performance based on features. It is represented as performance of MSVM Classification algorithm. This technique expose as accuracy (ACC), specificity (SPC), sensitivity (TPR), false positive (FPR), false negative (FNR), true positive (TPR), true negative (TPN). The Confusion Matrix is shown in Fig.13.

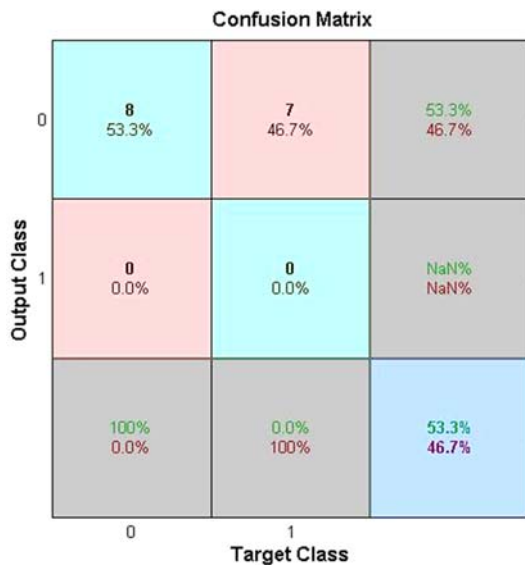


Fig. 13. Confusion Matrix performance.

$$TPR = \frac{TP}{P} \quad (36)$$

$$P = TP + FN$$

$$SPC = \frac{TN}{N} \quad (37)$$

$$N = FP + TN$$

$$PPV = \frac{TP}{TP + FP} \quad (38)$$

$$NPV = \frac{TN}{TN + FN} \quad (39)$$

$$ACC = \frac{TP + TN}{P + N} \quad (40)$$

Comparison performance of existing system and proposed system are shown in the Table 1.

Table 1. Comparison Features Performance.

Features	Existing system	Proposed system
Entropy	0.9624	0.9441
Mean	3.314	2.056
Variance	1.193	3.36
STD	1.0365	0.0174
SNR	3.1975	0.0118
LRPE	30.1205	3.0137

This table briefly explained about arousal detection of EEG and PSG data base. This performance analysis is briefly explained Brain signal analysis and also arousal and valance detection. This tabulation mentioned as different features by EEG DB. The features are Entropy, Mean, Standard Deviation, Signal to Noise Ratio, Logarithmic Relative Power Energy. These features are peacefully extracted from EEG and PSG using MSVM Proposed system. This implementation are developed by MATLAB 2013a Software , Memory 2 GB RAM, 3.40 GHz processor are we have used. This processor has only able to performing and speed result by using our MAT files DATA BASE.

#### 5. Conclusion

In this paper, the Arousal band detection approach is performed by Chebyshev with MSVM segmentation & Classification algorithms. The segmentation algorithm mainly to segment EEG and PSG Database, and then extracting bands from EEG based in frequency range. The algorithm result shows that the various features from various algorithms and its all are parameters are evaluated. Mainly compared features by segmentation level algorithm.

#### References

- [1]. J. J. Dongarra, B. Straughan, D. W. Walker, Chebyshev tau-QZ algorithm methods for calculating spectra of hydrodynamic stability problems, *Applied Numerical Mathematics*, Vol. 22, Issue 4, December 1996, pp. 399-434.

- [2]. Yunkai Zhou and Yousef Saad, A Chebyshev–Davidson Algorithm for Large Symmetric Eigen problems, *SIAM. J. Matrix Anal. & Appl.*, 29, 3, 2007, pp. 954–971.
- [3]. John P. Boyd, A Fast Algorithm for Chebyshev, Fourier, and Sine Interpolation onto an Irregular Grid, *Journal of Computational Physics*, 103, 1992, pp. 243-257.
- [4]. Martin H. Gutknecht, Stefan Röllin, The Chebyshev iteration revisited, *Parallel Computing*, Vol. 28, 2, February 2002, pp. 263–283.
- [5]. Enis Getin, Omer N. Gerek, and Yasemin Yardimci, Equiripple FIR filter design by the FFT algorithm, *IEEE Signal Processing Magazine*, Vol. 14, Issue 2, 1997, pp. 60 - 64.
- [6]. Ales Prochazka, Jaromir Kukal, Oldrich Vysata, Wavelet transform use for feature extraction and EEG signal segments classification, in *Proceedings of the 3<sup>rd</sup> International Symposium on Communications, Control and Signal Processing (ISCCSP'08)*, 2008.
- [7]. Ibrahim Omerhodzic, Samir Avdakovic, Amir Nuhanovic, Kemal Dizdarevic and Kresimir Rotim, Energy Distribution of EEG Signal Components by Wavelet Transform, in *Wavelet Transforms and Their Recent Applications in Biology and Geoscience*, Dumitru Baleanu (Ed.), *InTech*, 2012.
- [8]. Hsiao-Chun Wu, Novel robust optimal filter design method and new transition band analysis, in *Proceedings of the IEEE International Symposium on Broadband Multimedia Systems and Broadcasting (BMSB)*, 2013.
- [9]. Sande Seema Bhogeshwar, M. K. Soni, Dipali Bansal, Design of Simulink Model to denoise ECG signal using various IIR & FIR filters, in *Proceedings of the International Conference on Optimization, Reliability, and Information Technology (ICROIT'14)*, 2014.
- [10]. Tao Zhou, A scale invariant keypoints detector, in *Proceedings of the International Conference on Security, Pattern Analysis, and Cybernetics (SPAC)*, 2014.
- [11]. E. A. Barra, J. M. Jagadeesh, Wavelet functions to estimate velocity in spatiotemporal signals, *IEEE Transactions on Signal Processing*, Vol. 46, Issue 4, 1998, pp. 1105 – 1118.
- [12]. Benzy V. K., Jasmin E. A., Rachel Cherian Koshy, Frank Amal, Wavelet Entropy as a measure of Depth of Anaesthesia, in *Proceedings of the 3<sup>rd</sup> International Conference on Signal Processing and Integrated Networks (SPIN' 16)*, 2016.



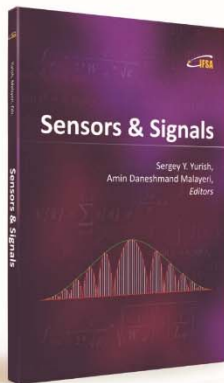
Published by International Frequency Sensor Association (IFSA) Publishing, S. L., 2017  
(<http://www.sensorsportal.com>).



International Frequency Sensor Association (IFSA) Publishing

# Sensors & Signals

Sergey Y. Yurish, Amin Daneshmand Malayeri, *Editors*



Formats: printable pdf (Acrobat) and print (hardcover), 208 pages

ISBN: 978-84-608-2320-9,  
e-ISBN: 978-84-608-2319-3

*Sensors & Signals* is the first book from the Book Series of the same name published by IFSA Publishing. The book contains eight chapters written by authors from universities and research centers from 12 countries: Cuba, Czech Republic, Egypt, Malaysia, Morocco, Portugal, Serbia, South Korea, Spain and Turkey. The coverage includes most recent developments in:

- Virtual instrumentation for analysis of ultrasonic signals;
- Humidity sensors (materials and sensor preparation and characteristics);
- Fault tolerance and fault management issues in Wireless Sensor Networks;
- Localization of target nodes in a 3-D Wireless Sensor Network;
- Opto-elastography imaging technique for tumor localization and characterization;
- Nuclear and geophysical sensors for landmines detection;
- Optimal color space for human skin detection at image recognition;
- Design of narrowband substrate integrated waveguide bandpass filters.

Each chapter of the book includes a state-of-the-art review in appropriate topic and well selected appropriate references at the end.

With its distinguished editors and international team of contributors *Sensors & Signals* is suitable for academic and industrial research scientists, engineers as well as PhD students working in the area of sensors and its application.

[http://www.sensorsportal.com/HTML/BOOKSTORE/Sensors\\_and\\_Signals.htm](http://www.sensorsportal.com/HTML/BOOKSTORE/Sensors_and_Signals.htm)

## Optimal Threshold Estimation Using Cultural Algorithm for EMD-DWT based ECG Denoising

Rama Raju N. S. V. N. and <sup>2</sup> V. Malleswara Rao

Department of Electronics and Communications, GITAM University, INDIA

Tel.: 9440922326

E-mail: ramarajupro@gmail.com, vmalleswararao@gitam.edu

*Received: 2017 /Accepted: 31 March 2017 /Published: 30 April 2017*

---

**Abstract:** The electrocardiogram (ECG) signal is widely used as one of the most important for analysis of cardiac condition of patients. It is necessary to filter the non-stationary noise from source to find clean ECG. This work falls within the overall framework of digital processing of the physiological signal. At first data driven EMD method is chosen to get the IMFS and these IMFS further passed through DWT for filtration. To achieve the adaptive filtering process better further optimal threshold is calculated based on cultural algorithm. Denoising is performed on MIT-BIH database and evaluated with parameter called SER, MSE, and cross correlation. It is found that the hybrid algorithm EMD + DWT + Cultural based yield better results than traditional methods.

**Keywords:** EMD, DWT, IMF, SER, MSE, Cultural algorithm.

---

### 1. Introduction

Automated processing of ECG signals has gained widespread interest in the last few years in both medical and signal processing environments. The challenge is very interesting: given the "sensitivity" of the field, the final goal of automatic processing (to complete or even substitute the physician's contribution) remains a particularly delicate task.

During the acquisition process, ECG signals are affected by multiple sources of distortion. The pre-processing step should minimize the effect of these interfering interferences, while conserving the useful components of the signal with great attention. Among the most common disturbances are interferences with the electrical network (the "50 Hz"), baseline fluctuations (due to breathing or patient movements) and so called "electromyographic noise" (EMG) caused by muscle activity [1]. ECGs are superposing in this domain. Other researchers have used spatial filters based on the fact that the maternal and they use a number of electrode signals, to find a linear

combination between the observations, and determine the best coefficients to model a weighted sum of these observation signals. EMD (empirical mode decomposition) based approach is proposed to remove high frequency noise and base line wandering in MIT-BIH database [2]. Suggested work has few deficiencies regarding the discard of unwanted IMFs, hence hybrid approach with ensemble empirical mode decomposition along with Wiener filter is proposed. [3-4] hence further adaptive techniques adopted to justify the non-stationary behaviour of ECG signals are explored with nonlinear Bayesian filtering framework with adaptive Gaussian noise [5].

Beside the mentioned methods, adaptive filter has also been applied successfully on the problem of ECG extraction [6]. This filter is generally based on adapting the coefficients of a linear filter through several iterations in order to estimate the adaptive filters may be sensitive to the temporal shape of the reference signal especially if only one reference is used; therefore, it normally requires multi reference signals [7-8].



Some studies have formulated the ECG extraction as a blind source separation (BSS) problem [9]. BSS is based on the assumption that the abdominal ECG channel is composed of independent components. The two main approaches which exist in this regard are Principal Component Analysis (PCA) and Independent Component Analysis (ICA). PCA tries to project the mixing signal onto the principal axis of its covariance matrix. Therefore, the PCA components are geometrically orthogonal by construction and also statistically orthogonal. This method is thus based on the removal of second order dependencies of the observation signals [10]. ICA approach looks for components which are not necessarily geometrically orthogonal, but are statistically independent, and tries to remove the higher order statistics of the sources [11]. The aim of ICA is to find the mixing matrix in equation (2.4) such that the sources are mutually statistically independent. The aim of ICA is to find the mixing matrix [12] such that the sources are mutually statistically independent. ICA is compared to PCA [13] and is proved to perform better in the literature [14-15].

The wavelet transform (WT) is another approach that has been proposed for the problem of ECG denoising. Different techniques for noise removal and/or detection of ECG waveforms have been used using Shannon and Tsallis entropy [16]. Non-local wavelet transform domain filtering [17] and optimal selection of wavelet thresholding algorithm for ECG signal denoising [18] has been proposed. The threshold selection was major issue while denoising the ECG, to overcome the problem various hybrid model has been proposed, electrocardiogram extraction based on non-stationary ICA and wavelet denoising [19] which claim better extraction of noise free ECG compare to traditional DWT method. Denoising of weak ECG signals by using wavelet analysis and fuzzy thresholding [20] claims optimal threshold calculation according to signal nature. Genetic algorithm and wavelet hybrid scheme is further proposed for denoising the ECG [21]. ECG signal denoising by functional link artificial neural network (FLANN) [22], An adaptive filtering approach for electrocardiogram (ECG) signal noise reduction using neural networks [23], has been proposed with limitation of predefined training information. PSO combined partial differential equation filtering based approach is suggested for ECG [24]. Further Modified PSO is suggested for denoising [25]. The soft computing based approaches ensures the optimal solutions of threshold estimation [26-29]. This paper proposes the hybrid approach of denoising the ECG signals.

## 2. Pre-Processing of ECG Signal

During the automatic processing of the ECG signal, consisting of the succession of a few steps (segmentation, analysis, classification), a pre-processing stage often imperatively necessary. It can

include all processing to eliminate the various perturbations which degrade the quality of the recording: the interference with the baseline oscillations due to movements or respiration of the patient, noise induced by the electrical activity of the muscles etc. Except the quality of the signal to be treated (this whole category of processing is sometimes grouped under the generic name of "denoising") manuscript in different sections.

### 2.1. Denoising of the ECG

The ECG signal is subjected to a set of disturbances caused by the movements or breathing, muscle electrical activity, inappropriate positioning electrodes, interference with the electrical network etc. All these undesirable phenomena lead to a degradation of the quality of the recorded ECG signal and make it automatic processing. Therefore, preliminary signal processing is strongly necessary in most cases. Given the peculiarities of the field, the quality of such a pre-processing must be irreproachable: it must consider the elimination of disturbing influences, while faithfully keeping the essential characteristics of the useful waves that make up the signal. These characteristics (including form, duration, and spectrum) will later be used to extract the parameters that "decide" the classification, therefore their slightest degradation can affect the automatic "verdict", that is to say the classification of the patient. This clearly explains the importance of denoising quality.

In recent years, new techniques based on the wavelets have become popular in the context of signal denoising. Indeed, this transformed has the remarkable property of "concentrating" most of the signal energy useful in a reduced number of high energy coefficients in the "transformed" domain. By against, the coefficients representing the image of the noise in the domain of the transformed wavelets will be numerous, but of low energy. In view of the above observations, the principle of a denoising system based on the wavelet transform results quickly. It consists of three successive steps:

1. Application of the wavelet transform to the signal affected by noise.
2. The filtering of the coefficients thus obtained, according to a certain criterion.
3. The calculation of the inverse transform, starting from the coefficients resulting from step former.

Such a denoising algorithm was originally proposed by Donoho [30] for the case of additive noise. It relies on the use of the discrete wavelet transform (DWT) for steps 1 and 3 and on non-linear adaptive filtering of the coefficients in step 2, known filtering on the name of "thresholding". The threshold value is set taking into account the estimate of the variance of the noise which affects the useful signal. In fact, this modality of choosing the threshold constitutes the weak point of the algorithm, since it does not take not consider any information regarding the useful signal. In attempting to overcome this

disadvantage, an alternative approach has been implemented for step 2 of the algorithm. It includes a category of techniques of optimized threshold using cultural algorithm. In this case, cultural algorithm will predict threshold based on fitness function, which can further filter of the useful signal coefficients and the noise coefficients. The filtering will be the direct implementation of the analytical solution that maximizes the conditioned probability of useful coefficients, being "Noisy" observations. In order to implement the denoising of the ECG signals, this approach, given its rigorous mathematical bases and the experimental results obtained on working time. Towards such an approach, also carried out by experimental and theoretical studies on the particular case of ECG signals.

## 2.2. Soft Filtering in the Domain of the Wavelet Transform Applied for the ECG Signals

In the case of a soft filtering of the wavelet coefficients, the performance of the method are determined by two factors:

- The accuracy of a proper prediction of local and statistical property of the wavelet coefficients, both for the useful signal and for the noise.
- The quality of the prediction of the parameters for the two components (useful and disruptive) of a wavelet coefficient.

Of particular interest for the case of ECG signals is the Wiener filter says "Empirical" in the field of DWT, filter proposed in [31] and presented as an improvement of the "classical" Wiener filtering in the transformed domain. Given the importance of transformed into different wavelets. The estimation of the parameters of the useful signal is made thus using

a "pilot signal", obtained by the hard thresholding of the wavelet coefficients resulting from the application of the first DWT. This is the first step of the algorithm. The Soft threshold based filtering of the coefficients is done in the domain of the second DWT, under the hypothesis of a Gaussian distribution for both the useful and noise coefficients. This filtering is the second step of the algorithm. The idea has been implemented under different forms in the [32-34] case of ECG signals and the results been satisfactory. The benefits of such an approach have been stated and verified empirically by the authors in [35]. First, it is the ability of the system to properly preserve the forms of the useful waves of the ECG signal. Indeed, the conventional disadvantages of the denoising by the thresholding of the DWT in its usual form (sometimes called "DWT Decimated ") can be found in the case of ECG signals, with disturbing effects. Reconstruction of useful waves could be severely damaged by artefacts such as parasitic oscillations at the beginning and at the end of the QRS complex (the phenomenon of Gibbs, attributed to the translational variance of the decoded DWT) [35-37] or by the deformation of the "slow" waves of the signal (the P and T waves). In [35], the authors use a wavelet mother well localized in time to obtain the pilot signal, wavelet having the role of correctly reproducing the exact form of the QRS complex. The negative effect of such a choice for the shape of the P and T waves (which have a relatively slow temporal evolution) is corrected by the second step of the algorithm, where wavelets are well localized in frequency are preferred.

## 3. Proposed Method

The architecture for denoising method is shown in Fig.1.

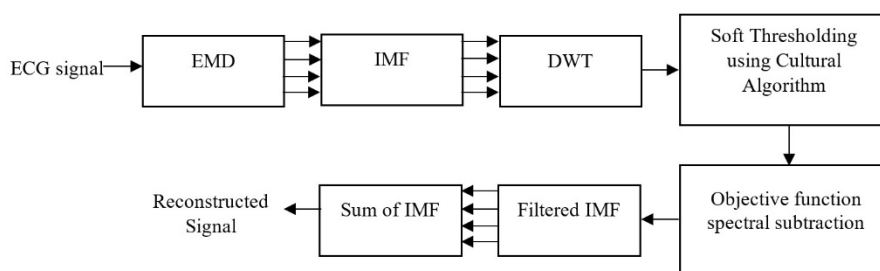


Fig. 1. Architecture for denoising method.

### 3.1. EMD: Original Method

Empirical Mode Decomposition (EMD) is a tool for Decomposition of non-linear, non-stationary signals proposed by Huang and his Colleagues [38]. It is defined by an empirical decomposition algorithm, without genuine theoretical evaluation. Despite its limited theoretical foundations, the method is applied to several types of real signals, including physiological

signals and Biomedical, where promising results are obtained. The EMD is used to extract descriptors from speech signals to classify emotions. It also used to extract descriptors of physiological signals, As well as to analyse the gastro-oesophageal information. The first time that the EMD method was tested on cardiac ECG signals, it was in the [9], who applied this method on simulated  $S_1$  and  $S_2$  signals [39]. Liu et al. [40] used the Hilbert-Huang transformation, which is based on

the Decomposition EMD, to extract features of cardiac sounds [40].

In primary step, the algorithm for EMD technique will be presented. The second step consists in applying the algorithm to real signals S1 and S2, in order to propose a method for extracting descriptors that discriminates between S1 and S2. The EMD is a recursive algorithm that aims to separate any signal  $x(t)$  into two components: approximation component which is the low frequency component (slow variations) and a second high frequency component (fast variations) called detail. These components are IMFs (Intrinsic mode functions). The main motivation for empirical modal decomposition is that it does not depend on the choice of a particular basis, such as wavelets, for example; The EMD is totally adaptive. The EMD algorithm, applied to the signal  $x(t)$ , can be illustrated by the following steps:

### EMD Algorithm

1. Initialization,  $r(t) = x(t)$  and  $k = 1$ .
2. Determine the extrema (maxima and minima) of the signal  $r(t)$ .
3. Interpolate by a cubic spline the minima and maxima to generate an envelope  $e_{min}(t)$  and  $e_{max}(t)$ , respectively.
4. Calculate the mean  $m(t) = \frac{[e_{min}(t)+e_{max}(t)]}{2}$  and extract intermediate functions:  
 $p_i = r(t) - m(t)$  and let  $r(t) = m(t)$
5. As long as  $p_i$  does not satisfy the conditions of an IMF (Intrinsic Mode Function), repeat:
  - Calculate the mean  $m_i(t)$  of  $p_i(t)$
  - $p_{i+1}(t) = p_i(t) - m_i(t)$ ;  $i = i + 1$
6.  $d_k(t) = p_i(t)$  and  $r(t) = r(t) - d_k(t)$
7. If  $r(t)$  is not monotone, return to step 2 and apply the increment in  $k$  as ( $k = k + 1$ ). Otherwise, the decomposition is complete.

At the end of the decomposition,  $x(t)$  can be reconstructed as follows:

$$x(t) = \sum_{k=1}^N d_k(t) + r(t) \quad (1)$$

The theoretical basis of the EMD method and to solve some disadvantages. For example, the spline interpolation, which aims to construct the envelopes of maxima and minimas respectively, generates in some cases "overshoot"; where the envelope constructed has an amplitude greater than the maximum of the signal, which introduces artefacts in step 5 of the algorithm, which is normally referred to as "Shifting Process" (SP). The individual IMFs are further samples to the cultural optimized soft thresholding.

### 3.2. Discrete Wavelet Transform

The different IMFs obtained from EMD (in case of mixed signals) holds some noise content as the abrupt peaks in signals. Every IMF is further transformed into frequency domain for more localize information about

noise by DWT. It gives Detailed Coefficients (DC) and Approximate Coefficients (AC) of signals according to high and low pass filtration accordingly.

$$X_i = \frac{1}{\sqrt{M}} \sum_n x(t) \varphi_i(n) \quad (2)$$

$$X_j = \frac{1}{\sqrt{M}} \sum_n x(t) \psi(n) \quad (3)$$

where  $i \geq j$ ,  $x(t)$  is the output and  $\varphi_i(n), x(t)\psi(n)$  depends upon  $n = 0, 1, \dots, M - 1$ . Equation (2) represents the approximate coefficients and Equation (3) represents detailed coefficients. This method corresponds to the objective set out at the beginning of the course and is the result of a theoretical and practical study on the subject of the processing of ECG signals.

### 3.3. Working Hypotheses

We consider the case of an ECG signal (s) perturbed by noise in an additive way (p). Since the classical white noise assumption is not realistic in the case of real physical noises that disrupt the ECG signal, the assumption is that the noise is additive, coloured, Gaussian and of zero mean. While the Gaussian and zero-mean PDF does not reduce the generality of the method, the hypothesis of a coloured noise predominantly considers the broadband type noise produced by the electrical activity of the muscles. This type of noise, called EMG (electromyography) noise, is the most difficult to remove, because its spectrum is partially coincident with the frequency band occupied by the useful ECG signal. Generally, it is considered as a random, wide-band noise (the phrase "almost white" is sometimes used in the literature) and having a non-stationary character. It should also be noted that for real ECG signals, an accurate characterization of the noise is not available. This means that even if one knows the possible sources of disturbance (listed above), neither the noise statistic nor its power spectral density is known. In practice, all the characteristics of the noise can vary between two separate ECG signals and even for recording from a single individual over time. We are then obliged to make the most general assumptions a priori, to place ourselves within a sufficiently broad and generic framework.

As for the signal, the authors in [32-34] take into account a Gaussian PDF of the DWT coefficients of the ECG signal. The hypothesis, on which the possibility of filtering Wiener is based, is not sufficiently realistic. In fact, the ECG signal has a highly non-stationary character: there are some "prominent" waves (P, QRS, T) separated by intervals that mark the lack of electrical activity (the isoelectric segments). In the domain of the wavelet transform, this results in the existence of a relatively small number of high-energy coefficients (marking especially the "breaks" in the signal, i.e. the beginnings and ends of the waves) and a large number

of low-energy coefficients, corresponding to the isoelectric segments and the slow variation portions of the signal. Therefore, the hypothesis of a Gaussian distribution seems inappropriate for realistic modeling of the useful coefficient statistics. To take into account the observations presented above, it was considered that a heavy-tailed distribution for the coefficients PDF is more realistic, and the particular case of a Laplacian distribution becomes very attractive given its Simplicity of calculation [41-42]. In order to illustrate the plausibility of this a priori assumption, the empirical observations (the histogram of the wavelet coefficients) and the theoretical curve representing a PDF. It should be remembered that the mathematical form of a Laplacian law is:

$$p_W(w) = \frac{1}{\sqrt{2}\sigma_w} \exp\left(-\frac{\sqrt{2}|w|}{\sigma_w}\right), \quad (4)$$

where  $\sigma_w$  is the standard deviation of the wavelet coefficients  $w$ .

The proposed denoising algorithm consists of two distinct steps:

**Step 1: Obtaining the processed signal**

The processed signal represents an estimate of the useful ECG signal. It is used to calculate the optimal threshold according fitness function of cultural algorithm, with the necessary statistical estimates of the useful wavelet coefficients. To obtain the processed signal, the noisy signal is sampled with EMD decomposition and obtained IMFs are transformed in the domain of the DWT  $w_1$  and its coefficients are threshold. The inverse transform is then applied to obtain the processed signal. For this step, it is better to choose a well-located mother wavelet in time [32]: it has been determined empirically that the daubechies wavelet provides the

best results. The filtering in the domain  $W_1$  is non-linear and consists in the simple application of a thresholding strategy: either soft-thresholding or hard thresholding [30]. Since no white noise has been assumed, this thresholding must be adapted to each decomposition scale of the DWT (the power of the noise is not equally distributed in all the frequency sub-bands corresponding to the different decomposition scales).

**Step 2: The optimal threshold from cultural algorithm in the domain of the  $W_2$  wavelet transform**

In general, an optimal threshold maximizes the a posteriori probability of obtaining the useful values, given the noisy observations. In Fig. 2, the steps taken to implement the second stage of the denoising algorithm were explained.

The Discrete wavelet transform (DWT) [43-44] was used for this step. The source of diversity is the wavelet wave selected for the calculation of the DWT. Generally, obtaining diversity is desirable because in each variant of the signal obtained by diversity there remains the same original signal (useful signal, signal to be estimated), affected by several variants of the noise. In fact, the transform proposed in [43-44] consists practically in different L DWT applied to the same input signal (see Fig. 2). For the particular case of an ECG signal, it is better to use in this step wavelet functions which are well localized in frequency (which may well preserve the forms of the P and T waves) and at the same time which are not Implemented by means of filters with an extremely long impulse response (these filters would introduce oscillations around the QRS complex) [32]. A compromise must therefore be secured in this respect. Another source of possible diversity is represented by the circular permutations of the signal samples.

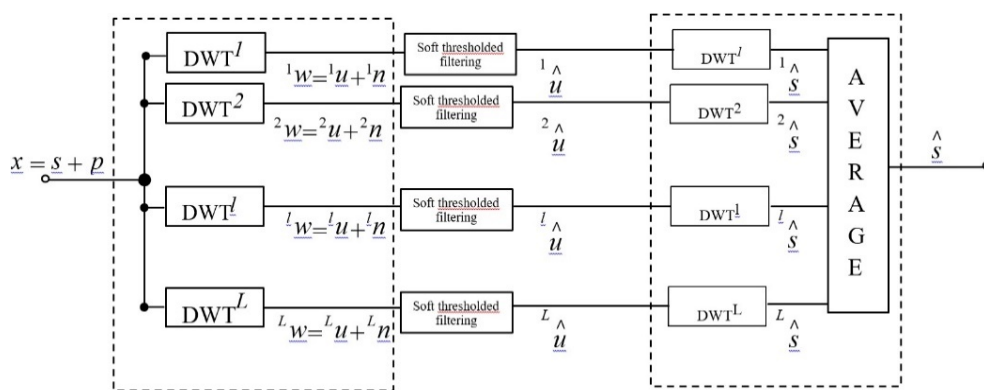


Fig. 2. Illustration of the second stage of the denoising algorithm.

The signal at the input of the system ( $x$ ) is considered as composed of a useful signal ( $s$ ) affected by additive noise ( $p$ ):

$$X = s + p \quad (5)$$

After the application of the DWT, one obtains at its output L sequences of wavelet coefficients, each sequence corresponding to the mother wavelet used for the calculation of the DWT:

$$l_w = l_u + l_n, \quad (6)$$

where  $l_u$  is the useful coefficients and  $l_n$  is the noise coefficients, with  $l = 1, \dots, L$ . The cultural algorithm gives the optimal threshold value according to fitness function of power spectral subtraction. The optimal threshold provides a filter maximizes the a posteriori probability of obtaining the useful coefficients ( $l_u$ ), given the observations disturbed by the noise ( $l_w$ ). The goal is to find for each DWT coefficients and hence the solution of the equation:

$$l_u(l_w) = \arg \max_{l_u} p_{u/w} \left( \frac{l_u}{l_w} \right) \quad (7)$$

Using the Bayes rule, equation (4) becomes:

$$l_u(l_w) = \arg \max_{l_u} \left( p_{w/u} \left( \frac{l_w}{l_u} \right) \cdot p_u(l_u) \right) = \arg \max_{l_u} (p_n(l_w - l_u) \cdot p_u(l_u)) \quad (8)$$

This equation expresses the estimation of the useful coefficients as a function of the probability densities respectively of the coefficients of the noise ( $p_n$ ) and of the useful coefficients ( $p_u$ ). The signals are in transformed domain only hence under consideration that a Gaussian distribution for the noise and Laplacian coefficients for the useful coefficients. Under these assumptions, the analytical solution of equation (7) [41-43] is:

$$l_{\hat{u}} = \frac{\left( l_w - \frac{\sqrt{2^l} \sigma_n^2}{l_{\sigma_u}} \right)_+}{l_w} \cdot l_w, l = 1, \dots, L, \quad (9)$$

where  $(X)_+ = \begin{cases} X, & \text{if } X > 0 \\ 0, & \text{others} \end{cases}$ . It can easily be seen that equation (9) actually represents a soft thresholding operation of the noisy coefficients, the threshold value being:

$$l_s = \frac{\sqrt{2^l} \sigma_n^2}{l_{\sigma_u}}, \quad (10)$$

Where  $\sigma_u$  is the variance of the noise and  $l_{\sigma_u}$  is the estimated value of the coefficients of the useful signal for the DWT with the index  $l$ . Indeed, the exact values of these parameters are not known (this would have solved our problem ideally) and must be estimated. The value of the useful coefficients, it will not remain constant across a decomposition scale. It is the non-stationary character of the ECG signal which leads to such a consequence: there will be breaks in the signal, marked by groups of high-energy wavelet coefficients, with successive zones of low-amplitude coefficients. Therefore, the local evaluation of this parameter is necessary, and the fact that a pilot signal is available facilitates this evaluation: instead of the standard deviation (equation 9) we take the absolute value of each DWT coefficient of the pilot signal. In practice,

the value of the threshold will be particularized for each coefficient: thus, the filtering becomes adaptive. In terms of noise variance, it is usually evaluated using the well-known median estimator:

$$\sigma_n^2 = \frac{\text{median}(w(j,k))}{0.6745} \quad (11)$$

where  $k = 1, \dots, M/2^j$  and  $j = 1$ ,  $w(j, k)$  is the wavelet coefficient that occupies the position  $k$  in the decomposition scale  $j$  and  $M$  is the length of the DWT. In the case of a white and Gaussian noise, the estimate is made only for the coefficients of detail obtained after the first iteration of the DWT ( $j = 1$ ): given the white character of the noise, this estimate remains valid for the others Scales, because  $\sigma_n^2$  do not depend on the scale  $j$ . On the other hand, if we consider the case of a noise that is not AWGN, the situation changes and the estimate must be made on each scale in particular.

The empirical study of the denoising of ECG signals has led to a different method for estimating this variance of noise. The reasoning is as follows: since the pilot signal is an approximation of the useful signal and since the noise is additive, it can be stated that the difference between the input signal and the pilot signal will be an approximation of the noise. Therefore, in order to obtain the variance of the noise at decomposition level  $j$  (of the DWT), this transform will be applied to the "noise" signal and the variance will simply be computed at  $j$  for the noise coefficients obtained, which will provide us The desired estimate. Considering all the observations made before, equation (6) becomes:

$$l_u(j, k) = \frac{\left[ l_w(j, k) - \sqrt{2^l} \sigma_n^2 / l_{\xi_u}(j, k) \right]_+}{l_w(j, k)} \cdot l_w(j, k), \quad (12)$$

where  $l_{\xi_u}(j, k)$  is the coefficients of the DWT (using the mother wavelet with the index  $l$ ) of the pilot signal. The relation in equation (12) shows that the Soft threshold based filtering is applied to each sample in particular ("sample-by-sample" processing), which is in agreement with the non-stationary character of the ECG signal (the threshold value must be variable in time) and with the colour spectrum of the noise (the threshold value must be "adapted in frequency").

As we have already discussed before, the use of the DWT in this stage of the algorithm provides a gain in diversity. Concretely, we have  $L$  different estimates for the key parameters of equation (9) instead of a single one. In our case, variance of the noise and the standard deviation are the useful coefficients. To measure this dependence, we define the sensitivity of the estimate of the coefficients:

$$S_u(\sigma_u) = \frac{du}{d\sigma_u} \frac{\sigma_u}{u} \quad (13)$$

For coefficients which are greater than the threshold defined by (10), substituting equation (9) in equation (13), this becomes:

$$S_u(\sigma_u) = \frac{\sqrt{2}\sigma_n^2}{\sigma_u w - \sqrt{2}\sigma_n^2} \quad (14)$$

The function defined in (14) is decreasing in  $\sigma_u$ . The wavelet coefficients have a small local variation in the zones corresponding to the slow evolution of the signal (for example, P wave). For these zones, with small values of the parameter  $\sigma_u$ , equation (14) indicates a greater approximation error. In this context, the use of L distinct estimates for  $\sigma_u$  can improve the results especially for these portions of the signal. This helps us to preserve the shape of the P wave, which is the most sensitive to noise and denoising (because of its low amplitude and its varied morphology).

Returning to Fig. 2, after the Soft threshold based filtering, the denoised signal is obtained via the discrete wavelet transform (DWT). This consists of calculating each inverse DWT (corresponding to the DWTs used in the DWT). The output signal is obtained by calculating the mean of the L variants denoised by  $l_{sc}$  from the following relation.

$$s(n) = \frac{1}{L} \sum_{l=1}^L l_{sc}(n), n = 1, \dots, M \quad (15)$$

Note that by means of the results of the various filtration given by (12). It can be assumed the residual noise is a Gaussian random process with zero mean. Its different realizations are the sequences of residual noise (which has "survived" soft threshold filtering) which disturb the useful signal. On the other hand, each sample can be considered as the summation of a useful sample (which, theoretically, is always the same since there is only one useful signal) and a residual noise sample (which is different for each branch of the DWT). Consequently, the calculation of the average of the corresponding samples at a fixed time point will result in the reciprocal cancellation of the remaining portion of noise in each sample. On the other hand, the useful signal will be well preserved (under the condition that the signal does not vary very quickly).

A "second iteration" of our algorithm could further improve the results. This iteration would consist in the reuse of the denoised signal as a better version of the processed signal. The signal resulting from the output of the system is returned to the input of the filtration process, where it will act as the processed signal for this second iteration.

Fitness function of cultural algorithm:

Spectral flatness: [44]

The spectral flatness is calculated by dividing the geometric mean of the power spectrum by the arithmetic mean of the power spectrum, i.e.:

$$\text{Flatness} = \frac{\sqrt[N]{\prod_{n=0}^{N-1} x(n)}}{\frac{1}{N} \sum_{n=0}^{N-1} x(n)} = \frac{\exp\left(\frac{1}{N} \sum_{n=0}^{N-1} \ln x(n)\right)}{\frac{1}{N} \sum_{n=0}^{N-1} x(n)} \quad (16)$$

where  $x(n)$  represents the magnitude of binary number  $n$ .

Cultural algorithm will evaluate the optimal threshold according to following fitness function.

$$Er = \min(1 - \text{Flatness}) \quad (17)$$

After spectral subtraction, filtered IMFs are summed up to get the reconstructed signal.

### 3.4. Cultural Algorithm

Inspired by the process of social and cultural changes, the CA was developed to enhance evolutionary computation. Cultural algorithms (introduced by Robert G. Reynolds) [44] modelling inspired by the evolution of human culture at two levels of scale:

- The micro level corresponding to a space describing a population of individuals;
- The macro level corresponding to a belief space.

The interactions between these two levels are described on the one hand by a validation / acceptance of the evolution of the population towards the space of belief and on the other by the influence of beliefs on population.

As Fig. 3 shows, the population space and the belief space can evolve respectively. The population space consists of the autonomous solution agents and the belief space is considered as a global knowledge repository. The evolutionary knowledge that stored in belief space can affect the agents in population space through influence function and the knowledge extracted from population space can be passed to belief space by the acceptance function.

In the process of the CA evolution, the population space is initialized with candidate solution agents at random, meanwhile, the initial knowledge sources in the belief space are built. At first the two spaces evolve independently. Then the selected agents from the population space are used to update the belief space. After the knowledge sources being updated, the belief space will reversely guide the evolution of the population space.

These procedures repeat till a termination condition has been reached. The CA pseudo code presented by [44] is given as follows:

$t=0$ ; no of iteration  $i=0$ ;

Define initial value of Population size  $p(i)$

Define initial value of Belief Space  $B(i)$

Repeat sequence

Evaluate Population size  $P(i)$ ;

Define new  $B(i)$ ,

Accept ( $P(i)$ );

Adjust ( $B(i)$ );

Variation ( $P(i)$  to  $P(i-1)$ );

Stop until condition achieved

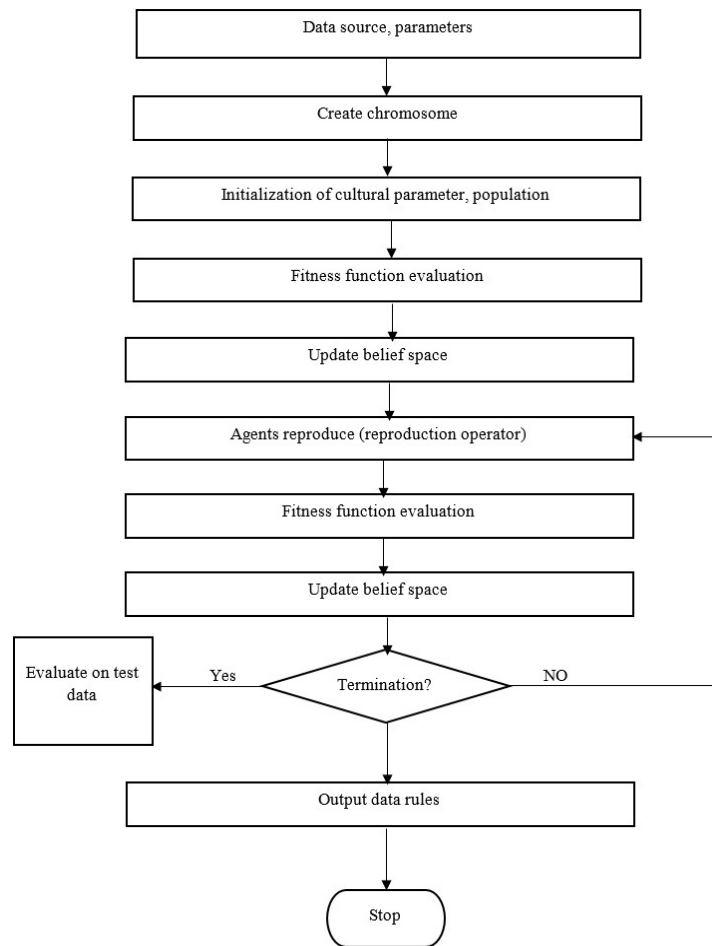


Fig. 3. CA framework.

### 3.5. Evaluation Parameters

#### 3.5.1. Signal-to-Noise Ratio (SNR)

The signal-to-noise ratio (SNR) is the ratio between the signal strength and the noise power.

$$SNR(dB) = 10 \log \frac{\sum_{n=1}^N s^2(n)}{\sum_{n=1}^N [S(n) - \hat{s}(n)]^2} \quad (18)$$

#### 3.5.2. Signal-to-Error Ratio (SER)

Signal to error ratio defined as

$$SER = \frac{\sum_{t=0}^{L-1} s^2(t)}{\sum_{t=0}^{L-1} [s(t) - \hat{s}(t)]^2} \quad (19)$$

where  $S(t)$  and  $\hat{S}(t)$  are the clean and reconstructed ECG signal respectively and  $L$  or  $N$  is the length of the signal.

#### 3.5.3. MSE

$$MSE = \frac{\sum_{n=1}^N [S(n) - \hat{S}(n)]^2}{\sum_{n=1}^N [S(n)]^2} \quad (20)$$

#### 3.5.4. Cross Correlation

Correlation is a measurement of the linear relationship between two continuous variables. The calculation of the correlation coefficient is covariance between two continuous variables. The coefficient of correlation is in fact the normalization of covariance. This normalization makes it possible to obtain a value which will always vary between -1 and +1, independent of the scale of the variables considered [45].

## 5. Experimental Setup

The MIT-BIH database [46] is a universal database containing 48 half-hour two-way records (DII and V5). It has been collected by researchers to be used as a reference for the validation and comparison of algorithms on the ECG signal.

- Each ECG recording is sampled at a frequency of 360 Hz.
- The main advantage of this database is that it contains a large number of cardiac pathologies, which makes it possible to validate the algorithms on a large number of ECG signal cases.

- The records correspond to subjects that are 25 men aged 32 to 89 years, and 22 women aged 23 to 89 years.
- The signals are numbered from 100 to 124 for the first group that includes a variety of waveforms and from 200 to 234 for the second group that includes a variety of pathological cases.
- In order to objectively evaluate the quality of the proposed methodology, to the usual measures used in this sense, noise was added generated artificially under MATLAB on a number of 5 signals from MIT-BIH database.

The signals were chosen from among the most "clean" possible and with morphologies different. To evaluate the results, the SNR was calculated. The noise was generated via a second order AR process, the signal disturbance thus resulting being a coloured noise, intended to simulate the physical noise broadband of the EMG type.

To calculate the SNR at the output of the system, we have considered as "signal error" the difference between the original signal and the denoised signal and the evaluation criterion that we used is the percentage of normalized squared error (SER) between the various reconstructed signals and the original signal not noisy.

Finally an ECG signal evaluate the robustness of our method by adding noise to the signals to obtain reports Signal / noise (SNR) of 6, 8, 10, 12, 14, 16 and 18 dB. We compared the performance of the method Classical to those of our approach. We have also looked at the error of our approach without adding signal part of the MFI 1 in the reconstruction, in order to apprehend in isolation the effect of the correction of threshold estimation on signal reconstruction interest. Simulation is carried out using MATLAB 2014.

Table 1 represents the different ECG signal against varying SNR value in dB. The observation shows the increase in SER value according increase in SNR. Lowest SER achieved when signal strength is high. Table 2 represents the comparative study of different methods proposed, EMD + DWT + Cultural gives better performance against varying SNR compare to other traditional method. Approximately 2-3 dB gain is achieved in proposed method.

Therefore we use cross correlation as a measurement of denoising impact on ECG based on different SNR, Cross correlation obtained after input ECG signal further normalized to get output between 0 to 1. The correlation coefficient value near to 1 resemble nearest match to the reference signal. Fig. 10 shows the maximum cross correlation at 18 dB SNR compare to lower order SNR value.

Fig. 11 claims the mean square value according SNR. It is observed that MSE value is high when noise power is more, gradually it is decreasing, according to decrement in noise power. At 18 dB minimum MSE is achieved i.e. .98. Fig. 12 shows the performance of signal to noise ratio over different input noise power. When input noise power (dB) increases the SNR increases. The performance of proposed method shows better than EMD and EMD + Wavelet methods.

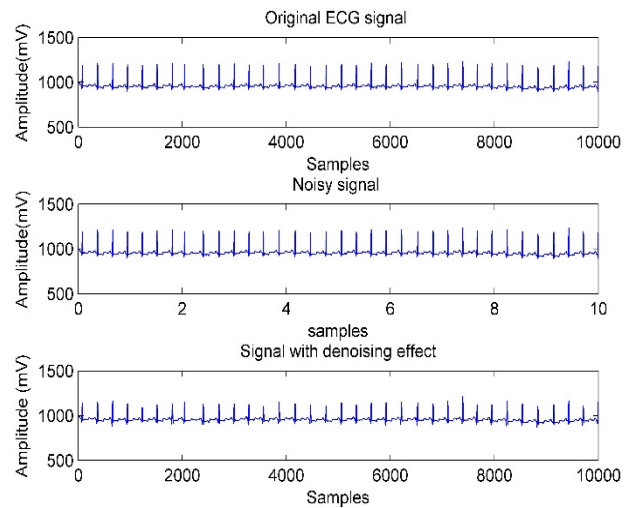


Fig. 4. Original ECG (100 m), noise with 14 dB SNR and denoised signal with proposed method.

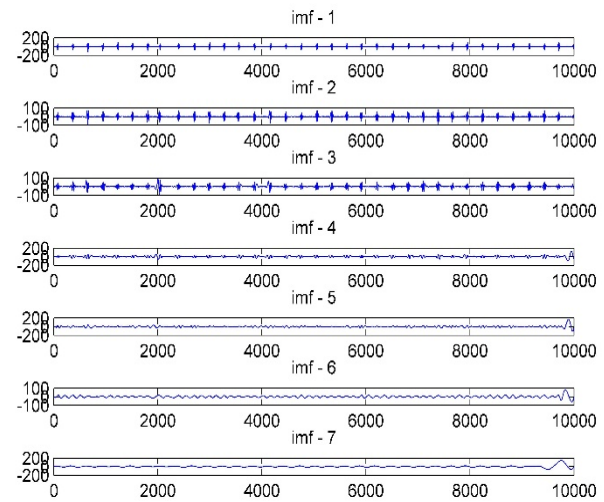


Fig. 5. Generated 1 to 8 IMFs after EMD.

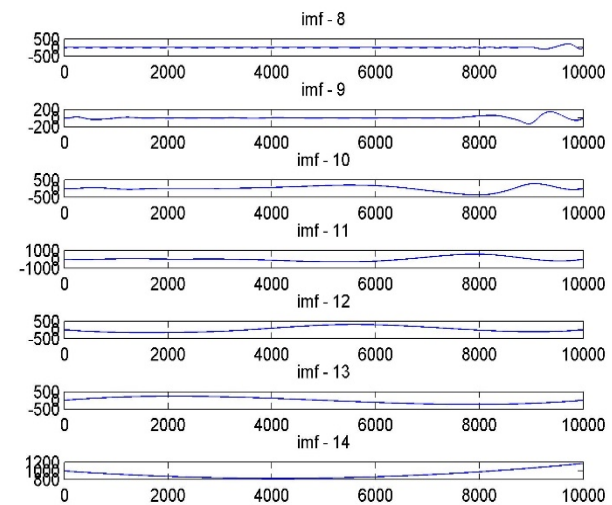


Fig. 6. Generated 9 to 14 IMFs after EMD.



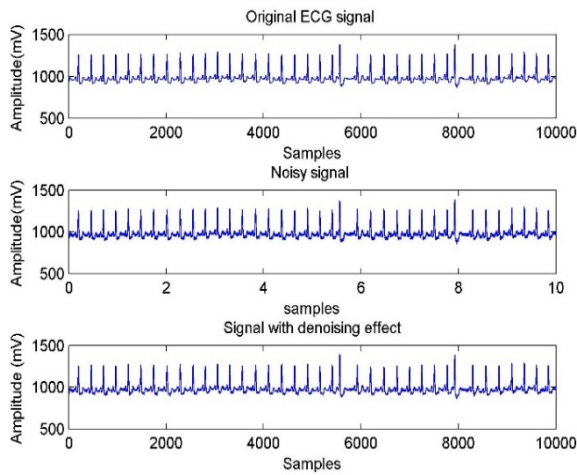


Fig. 7. Original ECG (105 m), noise with 18 dB SNR and denoised signal with proposed method.

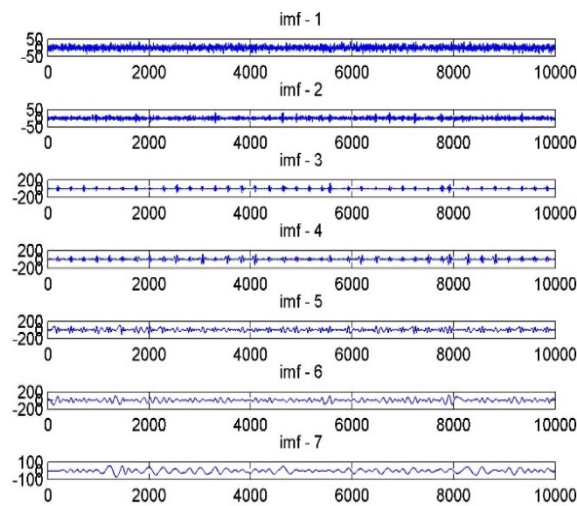


Fig. 8. Generated 1 to 8 IMFs after EMD.

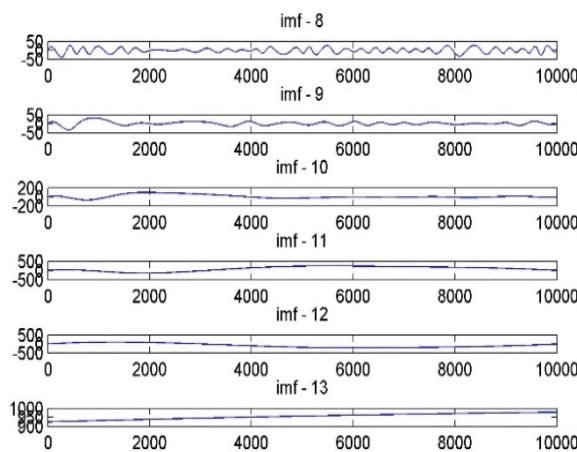


Fig. 9. Generated 9 to 14 IMFs after EMD.

Table 1. Experiments carried out for the several records from MIT-BIH arrhythmia database for additive white Gaussian noise (AWGN).

I/P SNR(dB)	ECG 100	ECG 103	ECG 105	ECG 119	ECG 212
6	26.6130	33.5129	37.9481	30.7114	25.1185
8	24.0910	33.8904	39.2179	21.4330	33.4391
10	35.9229	33.8653	40.357	32.6768	25.6640
12	28.0034	34.3316	41.3822	33.1530	34.5457
14	26.4311	34.4010	42.2049	33.6560	25.1798
16	36.0674	34.5119	43.1465	32.2159	34.6279
18	35.1695	34.4138	43.4989	34.2534	28.1049

Table 2. Comparisons various denoising methods for ECG record 105 model from MIT- BIH arrhythmia database.

SNR (dB)	EMD (dB)	EMD-DWT(dB)	EMD-CL-DWT(dB)
6	26.6130	29.234	37.9481
8	28.498	31.4534	39.2179
10	32.229	34.8653	40.357
12	34.005	36.4556	41.3822
14	36.5511	38.4010	42.2049
16	38.0344	40.119	43.1465
18	40.145	42.4338	43.4989

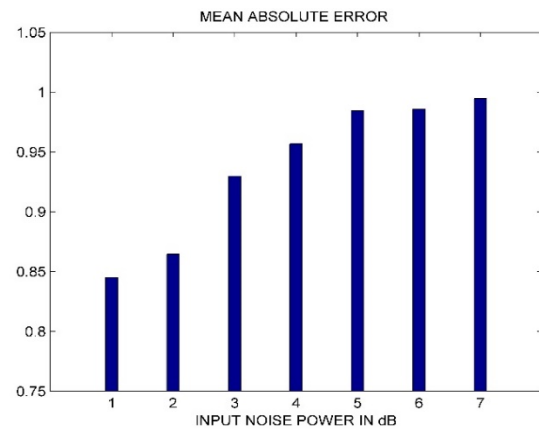


Fig. 10. Cross correlation calculation under different SNR (6-18) in MIT-BIH (100.mat) data.

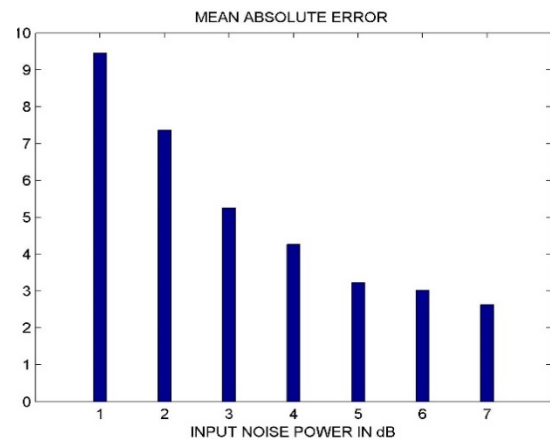


Fig. 11. Mean square error calculation under different SNR (6-18) in MIT – BIH (100.mat) data.

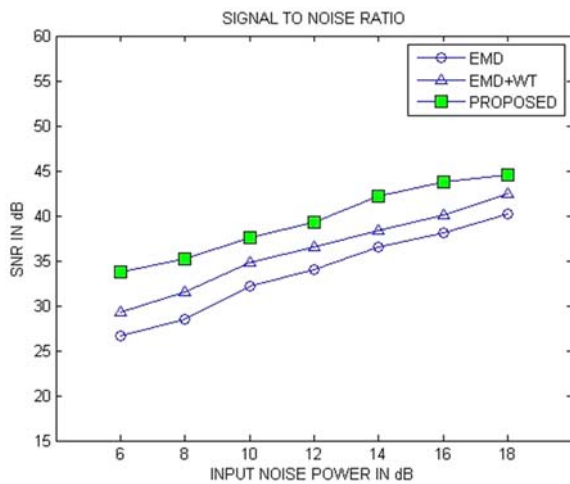


Fig. 12. Comparison of SNR for different methods with different input noise power.

## 6. Conclusion

The result of the work on this subject was the implementation of a denoising method which relies on the statistical properties of the SNR of the ECG signal. Some variants different from the proposed method have been tested under a variety of conditions and results have always been satisfactory. The tests carried out were aimed at bringing the more possible of the actual conditions from which such processing must operate. In this context, we have studied the influence of denoising on ECG signal, the synthetic noise ranges from 6 dB to 18 dB. The optimal selection of threshold using cultural algorithm yield better results than traditional results. Approximately 15 % of gain is achieved in proposed method.

## References

- [1]. Chacko, A. and Ari, S., Denoising of ECG signals using empirical mode decomposition based technique, in *Proceedings of the IEEE International Conference on Advances in Engineering, Science and Management (ICAESM'12)*, 2012, pp. 6-9.
- [2]. Blanco-Velasco, M., Weng, B. and Barner, K. E., ECG signal denoising and baseline wander correction based on the empirical mode decomposition, *Computers in Biology and Medicine*, 38, 1, 2008, pp. 1-13.
- [3]. Chang, K. M. and Liu, S. H., Gaussian noise filtering from ECG by Wiener filter and ensemble empirical mode decomposition, *Journal of Signal Processing Systems*, 64, 2, 2011, pp. 249-264.
- [4]. Smítal, L., Vitek, M., Kozumplík, J. and Provazník, I., Adaptive wavelet wiener filtering of ECG signals. *IEEE Transactions on Biomedical Engineering*, 60, 2, 2013, pp. 437-445.
- [5]. Sameni, R., Shamsollahi, M. B., Jutten, C. and Clifford, G. D., A nonlinear Bayesian filtering framework for ECG denoising. *IEEE Transactions on Biomedical Engineering*, 54, 12, 2007, pp. 2172-2185.
- [6]. Kabir, M. A., and Shahnaz, C., Denoising of ECG signals based on noise reduction algorithms in EMD and wavelet domains, *Biomedical Signal Processing and Control*, 7, 5, 2012, pp. 481-489.
- [7]. Rahman, M. Z. U., Shaik, R. A. and Reddy, D. R. K., Efficient sign based normalized adaptive filtering techniques for cancelation of artefacts in ECG signals: Application to wireless biotelemetry, *Signal Processing*, 91, 2, 2011, pp. 225-239.
- [8]. Wang, J., Ye, Y., Pan, X., Gao, X. and Zhuang, C., Fractional zero-phase filtering based on the Riemann-Liouville integral, *Signal Processing*, 98, 2014, pp. 150-157.
- [9]. Vázquez, R. R., Velez-Perez, H., Ranta, R., Dorr, V. L., Maquin, D. and Maillard, L., Blind source separation, wavelet denoising and discriminant analysis for EEG artefacts and noise cancelling, *Biomedical Signal Processing and Control*, 7, 4, 2012, pp. 389-400.
- [10]. Romero, I., PCA and ICA applied to Noise Reduction in Multi-lead ECG, in *Proceedings of the IEEE Computing in Cardiology Conference*, 2011, pp. 613-616.
- [11]. Sharma, R. and Patterh, M. S., A new pose invariant face recognition system using PCA and ANFIS, *Optik-International Journal for Light and Electron Optics*, 126, 23, 2015, pp. 3483-3487.
- [12]. Joshi, S. L., Vatti, R. A. and Tornekar, R. V., A survey on ECG signal denoising techniques, in *Proceedings of the IEEE International Conference on Communication Systems and Network Technologies (CSNT'13)*, 2013, pp. 60-64.
- [13]. Fernandes, S. L. and Bala, G. J., Recognizing facial images using ICA, LPP, MACE Gabor filters, score level fusion techniques, in *Proceedings of the International IEEE Conference on Electronics and Communication Systems (ICECS'14)*, 2014, pp. 1-5.
- [14]. Romero, I., PCA-based noise reduction in ambulatory ECGs, in *Proceedings of the Computing in Cardiology Conference*, 2010, pp. 677-680.
- [15]. Romero, I., PCA and ICA applied to Noise Reduction in Multi-lead ECG, in *Proceedings of the Computing in Cardiology Conference*, 2011, pp. 613-616.
- [16]. Beenamol, M., Prabavathy, S. and Mohanalin, J., Wavelet based seismic signal de-noising using Shannon and Tsallis entropy, *Computers & Mathematics with Applications*, 64, 11, 2012, pp. 3580-3593.
- [17]. Kabir, M. A. and Shahnaz, C., Denoising of ECG signals based on noise reduction algorithms in EMD and wavelet domains, *Biomedical Signal Processing and Control*, 7, 5, 2012, pp. 481-489.
- [17]. Yadav, S. K., Sinha, R. and Bora, P. K., Electrocardiogram signal denoising using non-local wavelet transform domain filtering, *IET Signal Processing*, 9, 1, 2015. pp. 88-96.
- [18]. Isa, S. M., Noviyanto, A. and Arymurthy, A. M., December. Optimal selection of wavelet thresholding algorithm for ECG signal denoising, in *Proceedings of the IEEE International Conference on Advanced Computer Science and Information System (ICACSIS'11)*, 2011, pp. 365-370.
- [19]. Vigneron, V., Paraschiv-Ionescu, A., Azancot, A., Sibony, O. and Jutten, C., Fetal electrocardiogram extraction based on non-stationary ICA and wavelet denoising, in *Proceedings of the 7th International IEEE Symposium on Signal Processing and its Applications*, Vol. 2, 2003, pp. 69-72.
- [20]. Üstündağ, M., Gökbulut, M., Şengür, A. and Ata, F., Denoising of weak ECG signals by using wavelet analysis and fuzzy thresholding, *Network Modeling*

- Analysis in Health Informatics and Bioinformatics*, 1, 4, 2012, pp. 135-140.
- [21]. El-Dahshan, E. S. A., Genetic algorithm and wavelet hybrid scheme for ECG signal denoising. *Telecommunication Systems*, 46, 3, 2011, pp. 209-215.
- [22]. Dey, N., Prasad Dash, T. and Dash, S., ECG signal denoising by functional link artificial neural network (FLANN), *International Journal of Biomedical Engineering and Technology*, 7, 4, 2011, pp. 377-389.
- [23]. Pongponso, S. and Yu, X. H., An adaptive filtering approach for electrocardiogram (ECG) signal noise reduction using neural networks, *Neurocomputing*, 117, 2013, pp. 206-213.
- [24]. Lahmiri, S. and Boukadoum, M., Combined partial differential equation filtering and particle swarm optimization for noisy biomedical image segmentation, in *Proceedings of the 7<sup>th</sup> IEEE Latin American Symposium on Circuits & Systems (LASCAS'16)*, 2016, pp. 363-366.
- [25]. Mahil, J. and Raja, T. S. R., An intelligent biological inspired evolutionary algorithm for the suppression of incubator interference in premature infants ECG, *Soft Computing*, 18, 3, 2014, pp. 571-578.
- [26]. Martis, R. J., Acharya, U. R., Adeli, H., Prasad, H., Tan, J. H., Chua, K. C., Too, C. L., Yeo, S. W. J. and Tong, L., Computer aided diagnosis of atrial arrhythmia using dimensionality reduction methods on transform domain representation, *Biomedical Signal Processing and Control*, 13, 2014, pp. 295-305.
- [27]. Lahmiri, S. and Boukadoum, M., A weighted bio-signal denoising approach using empirical mode decomposition, *Biomedical Engineering Letters*, 5, 2, 2015, pp. 131-139.
- [28]. Joshi, V., Verma, A. R. and Singh, Y., De-noising of ECG Signal Using Adaptive Filter Based on MPSO, *Procedia Computer Science*, 57, 2015, pp. 395-402.
- [29]. El-Dahshan, E. S. A., Genetic algorithm and wavelet hybrid scheme for ECG signal denoising, *Telecommunication Systems*, 46, 3, 2011, pp. 209-215.
- [30]. Donoho, D. L., De-noising by soft-thresholding, *IEEE Transactions on Information Theory*, 41, 3, 1995, pp. 613-627.
- [31]. Ghael, S. P., Sayeed, A. M. and Baraniuk, R. G., October. Improved wavelet denoising via empirical Wiener filtering, in *Proceedings of the Optical Science, Engineering and Instrumentation Conference 1997*, pp. 389-399.
- [32]. Nikolaev, N. and Gotchev, A., ECG signal denoising using wavelet domain Wiener filtering, in *Proceedings of the 10<sup>th</sup> IEEE European Signal Processing Conference*, 2000, September, pp. 1-4.
- [33]. Gotchev, A., Nikolaev, N. and Egiazarian, K., Improving the transform domain ECG denoising performance by applying interbeat and intra-beat decorrelating transforms, in *Proceedings of the IEEE International Symposium on Circuits and Systems (ISCAS' 01)*, 2001, Vol. 2, pp. 17-20.
- [34]. Nikolaev, N., Nikolov, Z., Gotchev, A. and Egiazarian, K., Wavelet domain Wiener filtering for ECG denoising using improved signal estimate, in *Proceedings of the IEEE International Conference on Acoustics, Speech, and Signal Processing (ICASSP'00)*, Vol. 6, 2000, pp. 3578-3581.
- [35]. Romaniuk, P., Non-regular distortions in ECG signal introduced by wavelet denoising, *Journal of Medical Informatics & Technologies*, 1, 2000, pp. B1-15.
- [36]. Romaniuk, P. and Chizyński, K., Clinical evaluation of ECG signal wavelet denoising method, *Journal of Medical Informatics & Technologies*, 2, Part 2, 2001, pp. MT49-55.
- [37]. Huang, N. E., Shen, Z., Long, S. R., Wu, M. C., Shih, H. H., Zheng, Q., Yen, N. C., Tung, C. C. and Liu, H. H., The empirical mode decomposition and the Hilbert spectrum for nonlinear and non-stationary time series analysis, in *Proceedings of the Royal Society of London A: Mathematical, Physical and Engineering Sciences*, Vol. 454, No. 1971, 1998, pp. 903-995.
- [38]. Charleston-Villalobos, S., Aljama-Corrales, A. T. and Gonzalez-Camarena, R., Analysis of simulated heart sounds by intrinsic mode functions, in *Proceedings of the 28<sup>th</sup> IEEE Annual International Conference on Engineering in Medicine and Biology Society (EMBS'06)*, 2006, pp. 2848-2851.
- [39]. Liu, L., Wang, H., Wang, Y., Tao, T. and Wu, X., Notice of Retraction Feature analysis of heart sound based on the improved Hilbert-Huang Transform, in *Proceedings of the 3<sup>rd</sup> IEEE International Conference on Computer Science and Information Technology (ICCSIT)*, Vol. 6, 2010, pp. 378-381.
- [40]. Sendur, L. and Selesnick, I. W., Bivariate shrinkage functions for wavelet-based denoising exploiting interscale dependency, *IEEE Transactions on Signal Processing*, 50, 11, 2002, pp. 2744-2756.
- [41]. Pizurica, A. and Philips, W., Multiscale statistical image models and Bayesian methods, in *Proceedings of the Photonics Technologies for Robotics, Automation, and Manufacturing Conference*, 2004, pp. 60-74.
- [42]. Nibhanupudi, S., Signal denoising using wavelets, Doctoral dissertation, *University of Cincinnati*, 2003.
- [43]. Oltean, M. and Adafinoaiei, V., ECG Signal Denoising in the Diversity Enhanced Wavelet Domain, *Scientific Bulletin of the Politehnica University of Timisoara, Trans. on Electronics and Communications*, 51, 65, 2006, pp. 63-68.
- [44]. Reynolds, R. G., An introduction to cultural algorithms, in *Proceedings of the Third Annual Conference on Evolutionary Programming*, Singapore, Vol. 131139, 1994.
- [45]. Stoica, P. and Moses, R. L., Spectral analysis of signals, Vol. 452, *Pearson Prentice Hall*, Upper Saddle River, NJ, 2005.



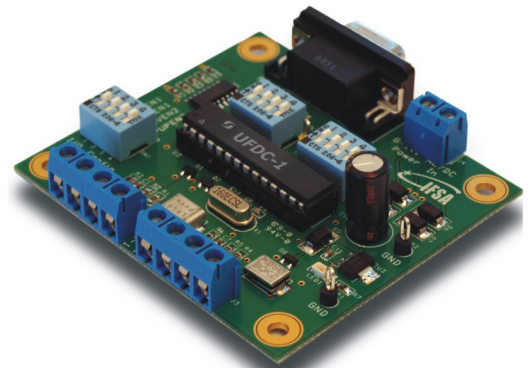
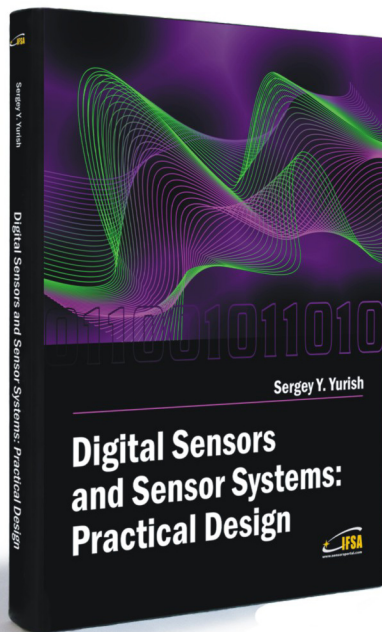
**Theory:**

# Digital Sensors and Sensor Systems: Practical Design

and

**Practice:**

## Development Board EVAL UFDC-1/UFDC-1M-16



Buy book and Evaluation board together. **Save 30.00 EUR**

### Development Board EVAL UFDC-1 / UFDC-1M-16

Full-featured development kit for the Universal Frequency-to-Digital Converters UFDC-1 and UFDC-1M-16. 2 channel, 16 measuring modes, high metrological performance, RS232/USB interface, master and slave communication modes. On-board frequency reference (quartz crystal oscillator). Operation from 8 to 14 V AC/DC. Development board software is included.

All existing frequency, period, duty-cycle, time interval, pulse-width modulated, pulse number and phase-shift output sensors and transducers can be directly connected to this 2-channel DAQ system. The user can connect TTL-compatible sensors' outputs to the Development Board, measure any output frequency-time parameters, and test out the sensor systems functions.

#### Applications:

- Digital sensors and sensor systems
- Smart sensors systems
- Data Acquisition for frequency-time parameters of electric signals
- Frequency counters
- Tachometers and tachometric systems
- Virtual instruments
- Educational process in sensors and measurements
- Remote laboratories and distance education

**Order online:**

[http://www.sensorsportal.com/HTML/BOOKSTORE/Digital\\_Sensors\\_and\\_Board.htm](http://www.sensorsportal.com/HTML/BOOKSTORE/Digital_Sensors_and_Board.htm)



International Frequency Sensor Association Publishing



[www.sensorsportal.com](http://www.sensorsportal.com)

ISSN 1726- 5479



9 771726 547001